

**Global Earth Structure Recovery  
from State-of-the-art Models  
of the Earth's Gravity Field  
and Additional Geophysical  
Information**

Ph.D. Thesis

Hamayun



# **Global Earth Structure Recovery from State-of-the-art Models of the Earth's Gravity Field and Additional Geophysical Information**

Proefschrift

ter verkrijging van de graad van doctor

aan de Technische Universiteit Delft,

op gezag van de Rector Magnificus prof. dr. ir. K.C. A. M. Luyben,

voorzitter van het College voor Promoties,

in het openbaar te verdedigen op maandag 30 juni 2014 om 10.00 uur

door

Hamayun

Master of Philosophy (MPhil.) in Physics

Department of Physics, Quaid-i-Azam University Islamabad, Pakistan

geboren te Shewa, Swabi, Pakistan.

Dit proefschrift is goedgekeurd door de promotor:

Prof. Dr.-Ing. habil. R. Klees

Samenstelling promotiecommissie:

Rector Magnificus

Prof. Dr.-Ing. habil. R. Klees,

Dr. P. Ditmar,

Prof. Dr. -Ing R. Tenzer,

Prof. Dr.-Ing. habil. J. Kusche,

Prof. Dr.Ir. R. F. Hanssen,

Prof. Dr. Ing. P. Novak,

Dr. M. van de Meijde,

Prof. Dr. M. Menenti

voorzitter

Technische Universiteit Delft, promotor

Technische Universiteit Delft, copromotor

Wuhan University, China, copromotor

Universiteit Bonn, Germany

Technische Universiteit Delft

Universiteit West Bohemia, Plzen

Universiteit Twente

Technische Universiteit Delft, reservelid

This thesis has been completed in partial fulfillment of the requirements of Delft University of Technology (Delft, the Netherlands) for the award of the Ph.D. degree. The research described in this thesis was supported by Delft University of Technology, and the Higher Education Commission Pakistan.

Published by Hamayun

email: hamayunkhan2000@yahoo.com

ISBN 978-94-6186-325-6

Keywords: Earth structure, Gravity field, Inverse problem

Copyright ©2014 by Hamayun

All rights reserved. No part of this publication may be reproduced, stored in a retrieval system, or transmitted in any form or by any means, electronic, mechanical, photocopying, recording, or otherwise, without permission of the author.

Printed in the Netherlands by Sieca Repro.

This work is dedicated to my family



# Contents

<b>Summary</b>	<b>xv</b>
<b>Acknowledgements</b>	<b>xix</b>
<b>1 Introduction</b>	<b>1</b>
1.1 Background . . . . .	1
1.2 Objectives . . . . .	3
1.3 Outline of the thesis . . . . .	4
<b>2 Earth structure and gravimetric methods for the recovery of the Moho geometry</b>	<b>7</b>
2.1 Composition of the Earth . . . . .	7
2.2 Moho discontinuity . . . . .	8
2.3 Reference density of crust and Moho density contrast . . . . .	10
2.4 Earth structure models . . . . .	11
2.5 Gravitational potential of a solid body . . . . .	14
2.6 Earth gravity and geoid . . . . .	14
2.7 Gravity disturbance and gravity anomaly . . . . .	16
2.8 Harmonic expansion of the gravity field . . . . .	18
2.9 Global gravity field model . . . . .	20
2.10 Isostasy and crust models . . . . .	20
2.11 Gravimetric methods for the Moho geometry . . . . .	24
2.12 Vening Meinesz's Model (VMM) . . . . .	26
<b>3 Analytical and semi analytical methods ..</b>	<b>29</b>
3.1 Point Mass Approach . . . . .	31
3.2 Gauss Cubature Approach . . . . .	32
3.3 Linear Vertical Mass /Semi-analytical Approach . . . . .	34
3.4 Homogeneous Rectangular Prism Method . . . . .	34
3.5 Line Integral Analytical Method . . . . .	36

3.6	Test For Numerical Accuracy And Efficiency . . . . .	48
3.7	Summary . . . . .	53
<b>4</b>	<b>Global maps of the CRUST 1.0 stripped gravity disturbances and gravity anomalies</b>	<b>55</b>
4.1	Corrections to gravity disturbances and anomalies . . . . .	57
4.1.1	Topographic stripping corrections . . . . .	59
4.1.2	Bathymetric stripping correction . . . . .	60
4.1.3	Ellipsoid-referenced topographic and bathymetric stripping correction . . . . .	63
4.1.4	Ice stripping corrections . . . . .	65
4.1.5	Sediment corrections . . . . .	65
4.1.6	Crustal corrections . . . . .	66
4.2	Stripped gravity disturbances and gravity anomalies . . . . .	67
4.3	Accuracy of the corrections applied . . . . .	70
4.4	Discussion . . . . .	71
4.5	Summary . . . . .	72
<b>5</b>	<b>Estimation of global crust-mantle density contrast</b>	<b>73</b>
5.1	Methodology . . . . .	76
5.2	Correlation of gravity field quantities with topography . . . . .	77
5.3	Correlation of gravity field quantities with bathymetry . . . . .	80
5.4	Correlation of gravity field quantities with Moho . . . . .	83
5.5	Estimation of the Moho density contrast . . . . .	85
5.6	Summary . . . . .	88
<b>6</b>	<b>Recovery of the Moho geometry as an inverse problem</b>	<b>89</b>
6.1	Residual gravity data as input for the computation of the Moho geometry	90
6.2	Computation of spherical harmonic coefficients of gravity disturbance (residual part $\delta g_r$ ) . . . . .	92
6.3	Linear Model for Moho configuration recovery . . . . .	92
6.4	Least-squares estimation . . . . .	94
6.5	Regularization . . . . .	96
6.6	Discrete zero-order and first-order Tikhonov regularization . . . . .	99
6.7	Solution strategy . . . . .	101
6.8	Summary . . . . .	102



<b>7</b>	<b>The Moho model and its validation</b>	<b>103</b>
7.1	Optimal data processing strategy . . . . .	104
7.1.1	Optimal data combination and the choice of regularisation . . .	105
7.1.2	Spherical harmonic coefficients low-degree contribution . . . .	107
7.1.3	Degree dependent weights of gravity data . . . . .	107
7.1.4	Maximum degree truncation . . . . .	109
7.2	Moho density contrast estimation from MMJF model . . . . .	110
7.3	Analysis of the obtain Moho model and comparison with alternative global models . . . . .	113
7.4	Regional comparison . . . . .	114
7.4.1	Moho model for South America (GDMSA) . . . . .	114
7.4.2	Moho model beneath Africa (PCSAA) . . . . .	121
7.5	Summary . . . . .	122
<b>8</b>	<b>Summary, conclusions and recommendations</b>	<b>125</b>
8.1	Summary and conclusions . . . . .	125
8.2	Major results . . . . .	128
8.3	Future recommendations . . . . .	128
<b>A</b>	<b>Algorithms for the computation of gravitational potential and attraction for poly- hedral body</b>	<b>131</b>
<b>B</b>	<b>Link between the Stokes coefficients <math>C_{lm}</math> and the mass distribution inside the Earth</b>	<b>135</b>
<b>C</b>	<b>Optimum regularization parameter estimation</b>	<b>139</b>
	<b>Bibliography</b>	<b>141</b>
	<b>List of publication</b>	<b>153</b>
	<b>Samenvatting</b>	<b>157</b>
	<b>Propositions</b>	<b>159</b>
	<b>Curriculum Vitae</b>	<b>161</b>



# List of Figures

2.1	Geometrical representation of geoid and reference ellipsoid . . . . .	17
2.2	(a) Isostatic model of Airy (b) Isostatic model of Pratt . . . . .	22
3.1	The inaccuracy of linear vertical mass approach relative to prism method (a) gravitational potential and (b) gravitational attraction. Red, green, and blue colour represent the computation for a spherical shell of the same dimension of a prisms of the height 100 m and the base area, $30 \times 30 \text{ m}^2$ , $150 \times 150 \text{ m}^2$ , and $300 \times 300 \text{ m}^2$ , respectively. . . . .	49
3.2	The inaccuracy of Gauss cubature approach relative to prism method (a) gravitational potential and (b) gravitational attraction. Red, green, and blue colour represent the computation for prisms of the height 100 m and the base area, $30 \times 30 \text{ m}^2$ , $150 \times 150 \text{ m}^2$ , and $300 \times 300 \text{ m}^2$ , respectively. . . . .	50
3.3	The inaccuracy of the point mass approach. relative to prism method (a) gravitational potential and (b) gravitational attraction. Red, green, and blue colour represent the computation for prisms of the height 100 m and the base area, $30 \times 30 \text{ m}^2$ , $150 \times 150 \text{ m}^2$ , and $300 \times 300 \text{ m}^2$ , respectively. . . . .	51
3.4	The relative time efficiency with respect to the line integral analytical method (a) potential (b) attraction. . . . .	52
4.1	Direct corrections (left), and the secondary indirect corrections (right) (a) topography, (b) bathymetric, (c) ice, (d) sediments, and (e) crust. . . . .	61
4.2	Total corrections: (a) topography, (b) bathymetry, (c) ice, (d) sediments and (e) crust. . . . .	62
4.3	The difference between the ellipsoid-referenced and geoid-referenced bathymetric and topographic correction. . . . .	64

4.4	(a) Gravity disturbances ( $\delta g$ ) (b) gravity anomalies ( $\Delta g$ ) at the Earth's surface. . . . .	68
4.5	Gravity disturbances (left) and gravity anomalies (right), from top to bottom: sequentially corrected for topography, bathymetry, ice and sediments, and crust heterogeneities. . . . .	69
5.1	(a) The global topography and bathymetry, (b) The depth of the Moho boundary; $1^0 \times 1^0$ discrete data from CRUST 1.0. . . . .	77
5.2	The relation between the topography $H$ and sequentially corrected gravity disturbances: (a) observed $\delta g$ , (b) topography corrected $\delta g^T$ , (c) topography and bathymetry corrected $\delta g^{TB}$ , (d) topography, bathymetry, ice, and sediment corrected $\delta g^{TBIS}$ and (e) topography, bathymetry, ice, sediment and consolidated crust corrected $\delta g^{TBISC}$ . . . . .	79
5.3	The relation between the Ocean depth $D$ and sequentially corrected gravity disturbances: (a) observed $\delta g$ , (b) topography corrected $\delta g^T$ , (c) topography and bathymetry corrected $\delta g^{TB}$ , (d) topography, bathymetry, ice and sediment corrected $\delta g^{TBIS}$ , and (e) topography, bathymetry, ice, sediment and consolidated crust corrected $\delta g^{TBISC}$ . . . . .	81
5.4	The relation between the Moho depth $H_m$ and sequentially corrected gravity disturbances: (a) observed $\delta g$ , (b) topography corrected $\delta g^T$ , (c) topography and bathymetry corrected $\delta g^{TB}$ , (d) topography, bathymetry, ice, and sediment corrected $\delta g^{TBIS}$ , and (e) topography, bathymetry, ice, sediment and consolidated crust corrected $\delta g^{TBISC}$ . . . . .	84
5.5	The absolute Pearson's correlation between the updated crust stripped gravity data and the Moho depths for different values of the Moho density contrast. Diamonds represent gravity disturbances and circles gravity anomalies (a) using CRUST 1.0 Model (b) using CRUST 2.0 . . . . .	87
7.1	Global Moho maps from (a) CRUST 1.0, (b) CRUST 2.0, (c) CRUST07, and (d) DMM-1 models . . . . .	111
7.2	Difference between DMM-1 and (a) CRUST 1.0, (b) CRUST 2.0, and (c) CRUST07 . . . . .	112
7.3	Histograms of differences between the GDMSA and (a) CRUST 1.0 (b) CRUST07 (c) DMM-1 . . . . .	115

---

7.4	Top: different Moho models, middle: difference with GDMSA, bottom: observation v.s. derive model. From left to right GDMSA, CRUST 1.0, DMM-1, and CRUST07 . . . . .	116
7.5	Histograms of differences between the PCSAA and (a) CRUST 1.0 (b) CRUST07 (c) DMM-1 . . . . .	119
7.6	Top: different Moho models, middle: difference with PCSAA, bottom: observation v.s. derive model. From Left to right, PCSAA, CRUST 1.0, DMM-1, and CRUST07. . . . .	120



# List of Tables

4.1	Statistics of ellipsoid-referenced direct correction . . . . .	60
4.2	Statistics of ellipsoid-referenced indirect correction . . . . .	60
4.3	Statistics of ellipsoid-referenced total correction . . . . .	63
4.4	Statistics of sequentially corrected gravity disturbances ( the super- scripts 'T' stands for topography; 'TB' for topography and bathymetry; 'TBI' for topography, bathymetry, and ice; 'TBIS' for topography, ba- thymetry, ice, and sediments; and 'TBISC' for topography, bathymetry, ice, sediments, and crust). . . . .	68
4.5	Statistics of sequentially-corrected gravity anomalies. . . . .	70
5.1	Pearson's correlation of the sequentially corrected gravity field quant- ities with the topography $H$ over the continents. . . . .	80
5.2	Pearson's correlation of the sequentially corrected gravity field quant- ities with the bathymetry. . . . .	82
5.3	Pearson's correlation of the sequentially corrected gravity field quant- ities with the Moho depth $H_m$ from CRUST 1.0. . . . .	85
7.1	Comparison of our different strategy based Moho models with EuM09 model, RMS difference in [km]. . . . .	106
7.2	Comparison of our different strategy based Moho models with Eu- crust07 model, RMS differences in [km]. . . . .	108
7.3	RMS differences [in km] between EuM09 and MMJF based strategy Moho model for different weights to spherical harmonics coefficients. . . . .	109
7.4	RMS difference [in km] between EuM09 and MMJF based strategy Moho model for different maximum-degree $L$ truncations. . . . .	110
7.5	Statistics of different Moho models, unit [km]. . . . .	113
7.6	Statistics of the differences between a DMM-1 on the one hand and CRUST 2.0, CRUST 1.0 and CRUST07 models on the other hand, [km].	113

7.7	Statistics for the Moho models over the South America. . . . .	117
7.8	RMS differences over the South America, between GDMSA Model on the one hand, and CRUST 2.0, CRUST 1.0 and DMM-1 models on the other hand . . . . .	117
7.9	RMS[km] differences between CTMAF Moho model with others Moho models for Africa. . . . .	118
7.10	Statics for the Moho models of the Africa. . . . .	118



# Summary

Currently, a tremendous improvement is observed in the accuracy and spatial resolution of global Earth's gravity field models. This improvement is achieved due to using various new data, including those from satellite gravimetry missions (CHAMP, GRACE, and GOCE); terrestrial and airborne gravity data, as well as altimetry data. The new gravity field models can be applied, in particular, to improve our knowledge of the Earth's interior structure. The aim of this study is to compile a global map of the Moho interface using a global gravity model and additional available information about the crust density structure. In our study, we use the gravity field model EIGEN-6C2 and the global crustal model CRUST1.0 derived from seismic data. In addition, we utilize seismic-based models of Moho as prior information: CRUST1.0 model, as well as the Crust07 model, which was derived by a fully non-linear inversion of fundamental mode surface waves.

The observed gravity field contains nuisance signals from the topography and density heterogeneities related to bathymetry, ice, sediments, and other crustal components. Therefore, we model and sequentially subtract these signals by applying so-called stripping corrections. This results in crust-stripped gravity field quantities (gravity anomalies and gravity disturbances). In the course of research, we review different analytical, semi-analytical, and numerical forward modeling techniques to compute the gravitational attraction of a body. We also derive an analytical formula for the computation of gravitational potential generated by a polyhedral body having linearly varying density. We compute the correction to observed gravity field using the analytical methods in the vicinity of the body and using semi-analytical methods in the far zone. We demonstrate that the sequential correction of gravity disturbances and gravity anomalies for nuisance signals increases the correlation with the Moho depths. We use the corrected gravity field to find the global (mean) value for the crust-mantle density contrast using the Pearson's correlation method. We use an empirical technique in which the absolute

correlation between the Moho depth from CRUST 1.0 model and the updated crust stripped gravity disturbances/anomalies is minimized. The updated stripped gravity disturbances/anomalies are obtained by adding a contribution (attraction) related to the density contrast between the reference crust and the upper most mantle to stripped gravity disturbances/anomalies.

The recovery of the Moho geometry is based on solving a system of linear equations which relates the crust-stripped gravity field (represented in terms of spherical harmonic coefficients) and the geometry of the Moho interface (represented in terms of Moho depths at the nodes of an equiangular geographical grid). In this way, corrections to the prior Moho configuration are estimated. It is known that a stand-alone inversion of gravimetric data may lead to inaccurate results because it is impossible to separate the signal from the interface under consideration and gravimetric signals from other sources (particularly, those located deeper inside the Earth). To suppress the latter signals (e.g, related to inhomogeneities of the mantle density and deep Earth structure), we propose to eliminate the contribution of low-degree spherical harmonics from input gravity data. Furthermore, we apply degree-dependent weights to the remaining spherical harmonics coefficients. The weight matrix is designed in such a way that low degrees are weighted less and high degree more.

We have developed an advanced inversion procedure in which gravity data and information from other (seismic) sources are exploited simultaneously, using zero-order and first-order Tikhonov regularization concepts. The variance components estimation (VCE) procedure is used for the estimation of relative weights of different data sets.

We consider a number of inversion strategies based on different combinations of data sets, regularization types, degree-dependent weights applied to input gravity data, as well as input gravity data minimum and maximum truncation degrees. For the selection of optimal inversion parameters, we compare the developed Moho models with the two regional Moho models for the European crust. The two models includes the EuCrust07 and EuM09 developed by Magdala Tesauro et al. and Marek Grad et al., respectively. We find that the best model is obtain when using a joint inversion (gravity data plus CRUST 1.0 and CRUST07 seismic models), first-order Tikhonov regularization, degree-dependent weights proportional to the fourth power of the degree and setting the minimum and maximum truncation degree equal to

90 and 180, respectively. The final Moho model (DMM-1) is compared with two regional models: (1) for the South America and (2) for Africa. From the comparison and statistical analysis we found that our developed model DMM-1 have the best RMS fit with the two regional models as well as with observed point values.



# Acknowledgements

First and foremost, I express my deepest gratitude to Allah, the Almighty for providing me the opportunity to complete my PhD studies, and granting me the required capability to proceed successfully. He has bestowed upon me the power to believe in my passions in order to pursue my dreams. Without this power and the consequent faith, I would be helpless.

I am indebted to my supervisor, Dr. P. Ditmar for his guidance, patience, perseverance, and useful critiques regarding my research work. I have no words to describe my gratefulness for his inputs. Dear Prof. R. Tenzer! I am deeply indebted to all your invaluable contributions towards the completion of my PhD studies. Your kind supervision, critical remarks and valuable corrections have provided me the opportunity to improve the quality of the thesis. I owe a plenty of gratitude to you. I would like to thank my promoter, Prof. R. Klees for providing me the opportunity to carry out this research. I am truly grateful for providing invaluable comments and suggestions on this dissertation, which have greatly improved its technical as well as linguistic quality. I am also thankful to you for assisting me with funding and support. I am thankful to Dr. Mark van de Meijde and Prof. Jeannot Trampert for useful discussion and providing the models data.

I wish to extend my special gratitude to my fellow researchers and colleagues Ilya Prutkin, Recardo Riva, Tobias Wittwer, Pedro Inacio, Joao Teixeira da Encarnacao, Olga Didova, Hassan Hashmifarahani, Rene Reudink, Mark Willem Jansen, Elena Revtova, Cornelis Slobe, Taco Broerse and Jasper Van Loon for their collaboration and excellent assistance. My gratitude also goes to all faculty members at PSG group. Thanks to Franca Post, Lidwien de Jong, Rebeca Demingo, Marjolein de Niet-de Jager, Relly van Wingarden and other GRS seretariat staff for their help in the administrative matters. Additionally, I want to acknowledge the HEC, NUFFIC and CICAT organization for their help in various administrative matters. I am grateful to my office at Islamabad for funding and support.

I am thankful to the members of the doctoral committee, who have spent their precious time in evaluating my research work and providing constructive recommendations, which help me to enhance this dissertation.

I am thankful to Faisal Nadeem, Seyab, Imran Ashraf, Rizwan Qaiser, and Mottaqiallah for proofreading of the thesis and for careful translation of the summary and propositions of the thesis into Dutch. I am also very grateful to my friends Mehfooz-ur-Rehman, Aqeel Khan, Fakhar Anjam, Mukhtar Ullah, Husnul Maab, Husnul Amin, Iftikhar Kazmi and Muhammad Nadeem. It is their encouragement that helped me to pursue and continue my research work in hardest of times. I would like to offer my special thanks to Abdul Hanan Sheikh for his hospitality during my stay for last few months. I want to acknowledge my senior PhD fellows, Laiq, Hisham, Zubair, and Tariq Abdullah who always supported me like brothers. I am also thankful to numerous HEC scholars Shah Muhammad, Saif Ullah Khalid, Atif, Cheema, Ch. Akram, Tabish, Shehzad Gishkori, Zahid Shabir, Iftikhar Faraz, Owais Ahmad, Rafi Ullah, A. H. Bangash, Faisal Karim. Umer Altaf, Mazhar, Fahim, Rajab, Atiq, Aleem, Nauman, Said Amin, Sa'ad *bhai* and many more.

Last, but not least, I would like to thank my parents, uncles, sisters, brothers, cousins and relatives for their unconditional love and support. It is only due to their prayers and encouragement, that I am able to complete this dissertation. Their love, care, and patience are indescribable, and beyond any words.

Special thanks and admiration go to my wife and my daughter Ayesha. I am also grateful to my nephews Haneef and Umar for their Love. All my love, wishes, and prayers are for you people. God bless you.

Hamayun  
Delft, The Netherlands, Jun 2014

---

# Introduction

## 1.1 Background

To learn more about the Earth's structure, geophysicists and geologists use two main sources of information: direct evidence from rock samples and indirect evidence from geophysical data. Geophysical data are the main source of information about the deep interior of the Earth. With geophysical data, the researchers have analysed the Earth's lithosphere and mantle, and their composition, structure and dynamics. Geophysical data are divided into two categories: those received through artificial sources, and those retrieved from the natural sources. In case of artificial sources, the researchers drill holes in the Earth's surface and blast rocks, and make inference about the deep conditions of the Earth. While the natural sources includes the data generated by earthquakes. The former is a time-consuming, expensive, and difficult method, because it is difficult to drill a deep hole due to the high temperature and pressure. The most common type geophysical data used for those purposes is the records of seismic waves generated by the earthquakes. However, such data can not provide a global coverages, for studying the Earth's crust and upper mantle.

An alternative source of information about the Earth's interiors is the gravity field. Gravity measurements sense density distribution inside the Earth. They play a vital role in modeling the Earth's interior especially in global and regional studies. Application of gravimetry in studying the global structure of the Earth is facilitated by the advent of modern satellite gravimetry missions as well as by the rapid increase in computational power. Several satellite missions, such as Challenging Mini-satellite Payload (CHAMP) (Reigber et al., 1996, 1999, 2002), Gravity Recovery

and Climate Experiment (GRACE) (Tapley et al., 2004) and Gravity field and steady-state Ocean Circulation Explorer (GOCE) (Drinkwater et al., 2003, Floberghagen et al., 2011) are delivering data that allow the accuracy and spatial resolution of global gravity field models to be improved drastically. The latest models based on the data from these missions have a spatial resolution of about 80 km in terms of half wavelengths. These models have global and homogeneous coverage and well-known stochastic properties. Further improvement of the spatial resolution can be achieved by combining satellite gravity data with airborne and ground-based gravity data and radar altimetry data over the oceans.

One of the primary interfaces of the Earth interior is the boundary between the crust and mantle, which is called the Mohorovičić discontinuity, or Moho. Geophysicists widely use seismic and gravity data to investigate the depth of the Moho discontinuity. Regional and global models of Moho are produced this way. In 1980, the establishment of International Lithosphere Program (ILP) emphasized the importance of investigating the Moho depth variation. The ILP seeks to explain the nature, dynamics, origin and evolution of the lithosphere through international, multidisciplinary geoscience research projects and coordination. The research aim to address societal needs, e.g. understanding natural catastrophes and other solid earth processes that affect the biosphere. The research provide information for improved resource exploration, environmental protection, and satisfying scientific curiosity. Lithosphere is a Latin words which mean stony layer. The crust and upper portion of the mantle called the lithosphere. It is a layer where most important geological processes occur, such as mountain-building, earthquakes and the source of volcanoes. The movements of Earth's tectonic plates is due to the slow churning and overturning of the mantle.

In gravimetry the gravity data are used to study the deep Earth structure. Generally, the gravity field functionals that are computed from the global gravity field models, are free air gravity anomalies or gravity disturbances. These gravity field functionals contain also the signal from terrain over continents, bathymetry variation over oceans, ice, sediments, and different density heterogeneity inside the crust and mantle. To use gravity data for the inversion into the Moho, the aforementioned signals contributors have to be removed from the gravity data. The relation between anomalous density distribution and gravitational attraction/potential is provided by the Newton volume integral. Various numerical methods are applied to evaluate the Newton's volume integral when studying the local gravity field. A



simple form of the integration is used, such as splitting the integration volume into right rectangular parallelepipeds (prisms) with constant density within each individual prism. For better accuracy of gravity field generated by a body having homogeneous/inhomogeneous density formations, the approximation of geological structures by more general geometrical forms than rectangular prisms has been adopted.

## 1.2 Objectives

The primary goal of this research is to use state-of-the-art information about the gravity field to improve the estimates of Moho depths globally. The basic procedure of gravimetric Moho modeling consists of two numerical steps; (1) the gravimetric forward modeling and (2) gravimetric inverse modeling. Gravity data used for a recovery of the Moho depths should comprise only the gravitational signal of the Moho geometry. Prior to used gravity data for Moho inversion, the gravitational signal generated by all know anomalous density structures should be modeled and subsequently removed from the observed gravity data. One can use either spatial or spectral description of the gravity field. Therefore, we first apply the gravimetric forward modeling step to calculate the gravity corrections and respective gravity data. For this purpose we use analytical expressions for computing the gravitational attraction and potential of a polyhedral body. The numerically efficient expression for computing the gravitational attraction of a polyhedral body is found in literature. However, numerical efficient expression for the gravitational potential is needed. In the course of research we derive the analytical expression for computing the gravitational potential of polyhedral body.

Traditionally, the gravity disturbances or anomalies are used for the inversion of the Moho depth. The crust corrected gravity (stripped gravity) data has maximum correlation with the Moho depth and hence best suited for the recovery of Moho geometry and the density contrast between the reference crust of constant density and mantle. Using the stripped gravity data, the global mean value for the crust-mantle density contrast can be estimated. The second step is implemented by establishing a linear relation between the topography of the Moho and the available gravity data (gravity disturbance and gravity anomaly), and then inverting the gravity data, together with the available information from seismic methods, into

the Moho topography. Gravity anomalies contains the long wavelength feature of the Earth structure, i.e., the signals from deep Earth structure, on the other hand gravity disturbances are more effected by the local variation in density structure. Therefore, gravity disturbances are more suitable for the refinement of shallow structure as compared to gravity anomalies.

Our procedure for solving the gravimetric Moho inverse problem is based on some assumptions: First assumption is the use of spherical approximation. The second assumption is adopting a global constant value for the crust-mantle density contrast. By applying proper corrections, the Earth crust density is replaced by a constant reference density of  $2670 \text{ kg/m}^3$ . The value of the crust-mantle density contrast is estimated relatively to the reference crust with constant density. In Moho geometry recovery, we use the input gravity data in the form of spherical harmonic coefficients (spectral domain). This allowed us to adopt degree dependent weights to the spherical harmonic coefficients of input gravity data, so that the signal from mantle heterogeneities is suppressed. Moreover, we assumed that the effects due to deeper Earth structure, mantle convection, oceanic lithosphere thermal contraction, tectonics motion, plate flexure, and elastic respond of the mantle are suppressed by eliminating the low degree coefficients of input gravity data.

### 1.3 Outline of the thesis

The remainder of the thesis is organized as follows:

**Chapter 2:** We present a brief literature overview in this chapter. It covers the structure of the Earth, a detailed history of the Moho interface studies, the isostatic crust models based on different hypothesis, and the existing crust models from seismic studies. Furthermore, this chapter includes a discussion on geopotential theory, Earth global geopotential models, and definitions of different gravity field functionals such as geoid, gravity disturbance, gravity anomaly etc.. Moreover, we discuss the computation of global gravity field functional from the Stokes coefficients and the transformation between spherical harmonic coefficients of various gravity field functional. Finally, the chapter is concluded with finding the global Moho using the Vening Meinesz's Model.

**Chapter 3:** In this chapter, we present different analytical and semi-analytical methods used for the forward modeling of the gravitational attraction and potential related to topography, bathymetry, ice, sediments, and other heterogeneities in the crust. We derived a new formula for the computation of gravitational potential of polyhedral bodies with constant or linearly changing density. We also present the numerical accuracy and efficiency of this formula.

**Chapter 4:** This chapter discusses the implementation of forward modeling algorithms and presents the preparation of the input gravity disturbances and gravity anomalies by removing the effects of the signals due to topography, bathymetry, ice, sediments and other heterogeneities in the crust. Based on these corrections the sequentially-stripped gravity field functionals are computed.

**Chapter 5:** In this chapter, we present the correlation of the gravity field functionals with topography, bathymetry, and Moho interface. We show that the application of subsequent corrections to the gravity field functionals improves their correlation with Moho topography. This confirms that the information content of the gravity field functionals is suited for the recovery of the Moho. Furthermore, we have demonstrated that the gravity disturbances are more suitable for the refinement of the Moho as compare to the gravity anomalies. The chapter is concluded with the estimation of the Moho density contrast by using an empirical formula.

**Chapter 6:** In this chapter, we propose and discuss the functional model for the recovery of Moho. The solution of linear stand-alone (gravity data) and joint (gravity and seismic data) inverse problems with zero and first order Tikhonov regularisation is presented. Weights for the individual data sets are estimated, using the variance component estimation technique. Application of zero weights to low-degree spherical harmonic coefficients to suppress the signal from deep Earth structure is discussed.

**Chapter 7:** In this chapter, we validate our adopted procedure for the recovery of the Moho geometry. These procedure include, the choice of the best data combination strategy, low-degree contribution of input gravity spherical harmonic coefficients and degree-depended weights of input gravity data. To get the optimal procedure

for the Moho recovery, we compare the develop models of the Moho depth with the high resolutions regional models for the European Moho. After the selection of final optimal model among our develop models, we compare it with the available global models. We also compare our final model with two available regional models of the Moho. One of the model is for the continent of the South America and the other is for the Africa.

**Chapter 8:** Finally, in this chapter, we have provided a summary and main results of the dissertation. Additionally, we have made suggestions for the future research in this field.

---

# Earth structure and gravimetric methods for the recovery of the Moho geometry

In this chapter, we briefly discuss the structure of the Earth, and its different layers and interfaces. We discuss the historical background of different crust structure models. Furthermore, we present a thorough review of local, regional and global isostatic crust models. Additionally, we present the analytical formula for gravity disturbances and gravity anomalies and link them to an expansion of the gravity field in spherical harmonics. Moreover, we illustrate different gravimetric methods for the determination of the Moho geometry. The solution of Vening Meinesz's inverse problem for the Moho recovery is reviewed.

## 2.1 Composition of the Earth

Geophysical studies reveal that the Earth consists of several distinct layers with different physical properties and chemical compositions. The three main layers are the crust, the mantle and the core. The crust is the outermost and thinnest layer. The next layer is the mantle, which extends to a depth of 2900 km. This is further subdivided into two parts: the upper mantle and the lower mantle. The innermost layer is the core. This is also further divided into the outer core and the inner core. The boundaries of these layers form discontinuities that may refract and reflect seismic waves. Global density models for different layers assume a spherically symmetric density distribution, which is a function of radial distance from the centre of the Earth ([Dziewonski and Anderson, 1981](#), [Bullen, 1975](#)).

The crust consists of silica-rich rocks which developed due to the melting of underlying mantle material, and subsequent metamorphic or erosional processes. Crustal rocks are broadly classified as igneous, metamorphic, or sedimentary, according to their individual characteristics. The crust is mainly divided into oceanic and continental crust. The thickness of the oceanic crust ranges from 6 to 12 km, while the continental crust is thicker, its thickness is more than 70 km. The oceanic crust is formed due to the decompression melting in the mantle at shallow depths beneath the mid-ocean ridges. The upper part of the crust consists of the exposed rocks and thin sedimentary layers having sharp variations in density and thickness. In the continental area, the upper crust below the sedimentary layer consists of granitic rocks with a mean density of  $2700 \text{ kg/m}^3$  (Torge, 1991). The granitic zone does not exist in the oceanic area. The lower crust is located beneath the upper crust, with a mean density of  $2900 \text{ kg/m}^3$ . The lower crust consists of basic rocks such as Gabbro (basalt). Below the lower crust, an abrupt increase in the velocity of seismic body waves and density is observed. For instance, the P-wave velocity increases from 7.1 km/s to 8.1 km/s. The lower boundary of the crust is called Mohorovičić discontinuity, or in short, Moho. The Moho separates the crust from the underlying mantle.

## 2.2 Moho discontinuity

Andrija Mohorovičić (1857-1936) discovered the Moho discontinuity in 1910, while he was studying the seismogram of the 8 October, 1909 earthquake in the Kulpa Valley, together with other earthquakes in this region (Mohorovičić, 1910, 1992). He observed two distinct pairs of compressional and shear waves. He wrote: “*When I was sure, based on data, that two kinds of first preliminary waves exist, both kinds reaching all locations from 300 km to 700 km distance, and that from the epicentre to approximately 300km distance only the first kind arrives, whereas from 700 km distance onward only the second kind arrives, I tried to explain this until now unknown fact*”. This observation led Mohorovičić to the conclusion that the Earth is not homogeneous, and at a specific depth there has to be a boundary surface, which separates two media with different elastic properties, and through which the waves must propagate with different velocities. He suggested that the first kind of arrival is from crystalline crust while the second kind of arrival corresponds to

the mantle. The interpretation of two sets of arrival times led Mohorovičić to the discovery of a velocity discontinuity. The estimated depth from his study was 50 km, the P-wave velocity was 5.6 km/s above and 7.747 km/s below this discontinuity and the S-wave velocity was 3.27 km/s above and 4.182 km/s below. In the past 100 years, seismologists studied different seismic profiles generated by earthquakes at different locations and proved that this discontinuity is present throughout the globe.

The discontinuity discovered by Mohorovičić provides the primary definition of the boundary between the crystalline crust and the upper mantle in terms of seismic waves velocities. Generally, the velocity of P-waves within the lower crust is smaller than 6.5 km/s, while that of S-waves is smaller than 4.4 km/s. The velocity of the P-waves in the upper mantle is about 7.9 km/s or more, and consequently, shows a velocity contrast of more than 1.0 km/s. This large velocity contrast indicates that there is a significant difference between the Earth crust and mantle in terms of elastic parameters, which can be explained by a difference in composition. Another definition for the Moho is in term of the density contrast between the Earth crust and mantle. The commonly used mean density of the crust is 2670 kg/m<sup>3</sup>, while for the mantle it is about 3300 kg/m<sup>3</sup> providing a density contrast of about 630 kg/m<sup>3</sup> at the Moho interface (Heiskanen, 1967). Many studies discuss the variation of the Moho density contrast and its mean value, including our own study (Tenzer et al., 2012a).

Many researches about the Moho geometry have been published in the last 10-15 years (e.g. Mooney et al., 1998, Kaban et al., 1999, Braitenberg et al., 2000, King et al., 2002, Banjeree and Satyaprakash, 2003). Meier et al. (2007), computed a global crustal model using fully non-linear inversion of fundamental mode surface waves. Moho in Australia was studied by Aitken et al. (2013) using the gravity data. The Moho model for the European Plate has been produced by Grad et al. (2009) using seismic as well as gravity maps. A new reference model for the European crust (EuCRUST-07) was presented by Magdala et al. (2008). Recently Van der Meijde et al. (2013) have produced gravity-derived Moho for the South America. Mariani et al. (2013) have identified a thick crust in Parana basin, Brazil, with GOCE gravity data.

## 2.3 Reference density of crust and Moho density contrast

The numerical value of the mean density of the crust used in the gravity reduction (Bouguer anomaly) is  $2670 \text{ kg/m}^3$  (Woollard, 1971). The average density of the upper continental crust  $2670 \text{ kg/m}^3$  is often adopted for defining the topographic and reference crust densities. This density better corresponds to the average density of the upper continental crust (cf. Hinze, 2003). The oceanic crust is typically heavier than the continental crust (e.g., Rogers N., 2008). Carlson and Raskin (1984), for instance, estimated the average density of the oceanic crust as  $2890 \pm 40 \text{ kg/m}^3$ . This estimate is based on seismic refraction data in combination with drilling results, laboratory studies of seismic properties of oceanic and ophiolitic rocks, and ophiolite lithostratigraphy.

In global studies, most of authors use a constant value of the Moho density contrast and compute the stripping corrections relative to the reference crustal density. The constant value of the Moho density contrast is again computed relative to the constant reference density of crust.

Tenzer et al. (2012a) used the consolidated crust-stripped gravity data to estimate the average Moho density contrast with respect to a homogenous crust layer of a reference density of  $2670 \text{ kg/m}^3$ . From that study, the average value is determined as  $485 \text{ kg/m}^3$ . The results are obtained by minimizing the correlation between the isostatic gravity disturbances and the Moho geometry. In that study the Moho geometry was taken from the global CRUST 2.0 model and stripped gravity disturbances were also computed using CRUST 2.0 model. This Moho density contrast closely agrees with the value of  $480 \text{ kg/m}^3$ , adopted in the definition of the PREM (cf. Dziewonski and Anderson, 1981, Table 1), which is derived based on seismic data. This value differs by about 7% from the global average  $448 \pm 187 \text{ kg/m}^3$  estimated by Sjöberg (2011b) based on solving the Vening Meinesz-Moritz (VMM) inverse problem of isostasy. Sjöberg (2011b) developed and applied also a least-squares approach, which combines seismic and gravity data in the VMM isostatic inverse scheme for a simultaneous estimation of the Moho depth and the Moho density contrast. The authors demonstrated that the Moho density contrast estimated that way varies considerably depending on the lithospheric structure of a particular region.



## 2.4 Earth structure models

Several global models of the Earth's structure have been developed based on the analysis of seismic data. [Dziewonski et al. \(1975\)](#) introduced the Parametric Earth Models (PEM) consisting of piece-wise continuous analytical functions of the radial density and velocity variations defined individually for the oceanic (PEM-O) and continental (PEM-C) lithosphere down to a depth of 420 km, below this depth these models are identical. They also provide an averaged function for the whole lithosphere (PEM-A). [Dziewonski and Anderson \(1981\)](#) presented the Preliminary Reference Earth Model (PREM), which provides information on the seismic velocities and density structure within the whole Earth's interior by means of spherically homogenous stratigraphic layers. [Van der Lee and Nolet \(1997\)](#) prepared the 1-D averaged model MC35 based on the PEM-C, while replacing the high and low velocity zones of the PEM-C by a constant S-wave velocity of 4.5 km/s within the upper mantle down to a depth of 210 km. [Kustowski et al. \(2008\)](#) derived the transversely isotropic reference Earth model STW105. In addition to these Earth's synthetic models, several other global and regional seismic velocity models were developed. A summary of these models can be found in [Trabant et al. \(2012\)](#).

The PEM and PREM models provide 1-D density information. Models based on a stratigraphic layering with a variable depth, thickness and laterally varying density distribution obviously represent the Earth's interior more realistically. Currently available global models provide information on a 3-D density structure only within the crust and upper mantle. The recently developed model by [Simmons et al. \(2010\)](#) contains the 3-D density structure of the whole mantle.

[Nataf \(1996\)](#) derived a global model of the crust and upper mantle density structure based on the analysis of seismic data and additional constraints such as heat flow and chemical composition. [Mooney et al. \(1998\)](#) compiled the global crustal model CRUST 5.1 with a  $5^0 \times 5^0$  spatial resolution. More recently, the global crustal model CRUST 2.0 was compiled with a  $2^0 \times 2^0$  spatial resolution ([Bassin et al., 2000](#)). This model has been prepared and administered by the U.S. Geological Survey and the Institute for Geophysics and Planetary Physics at the University of California. Both models were compiled based on seismic data published until 1995 and a detailed compilation of the ice and sediment thickness.

[Meier et al. \(2007\)](#) produced a global crustal model CRUST07, using fully non-linear inversion of fundamental mode surface wave. The resolution of CRUST07 model is  $2^0 \times 2^0$ . They use neural networks for finding 1-D marginal probability density functions (pdfs) of global crustal parameters. They have inverted the fundamental mode Love and Rayleigh wave phase and group velocity for the pdfs of crustal thickness. The constructed model provides the mean Moho depths and its standard deviations. In our work, we have utilized the data provided by this model as a-priori information.

Most recently, CRUST 1.0 has been released, which has a  $1^0 \times 1^0$  spatial resolution ([Laske et al., 2013](#)). CRUST 1.0 is the result of a comprehensive effort to compile a global model of the Earth's crust and lithosphere, LITHO 1.0 ([Pasyanos et al., 2012](#), [Laske et al., 2013](#)). LITHO1.0 is a  $1^0 \times 1^0$  model of the crust and uppermost mantle of the Earth. It is created by constructing an appropriate starting model and perturbing it to fit high-resolution surface wave dispersion maps. The CRUST 1.0 consists of the topography, ice, water layer, sediments layers and crustal layers. In addition, lateral varying density structure of the upper mantle is incorporated into CRUST 1.0. The globally averaged data from active seismic methods and deep drilling profiles were used to predict the sediment and crustal structure. In regions where no seismic measurements were available (most of Africa, South America, Greenland and large parts of the oceanic lithosphere) the crustal structure assigned by a generalization to similar geological and tectonic settings. For cells with no local seismic or gravity constraints, statistical averages of crustal properties, including crustal thickness, were extrapolated. The Moho depth in CRUST 1.0 is based on  $1^0 \times 1^0$  averages of a recently updated database of crustal thickness data from active source seismic studies as well as from receiver function studies. This model incorporates an updated version of the global sediment thickness.

The compilation of CRUST 1.0 initially followed the philosophy of the crustal model CRUST 2.0 by assigning elastic properties in the crystalline crust according to the basement age or tectonic settings. This reduces the possibilities of errors in both models. The sediment model ([Laske, 1997](#)) is an independent part of the CRUST 1.0 model. The sediment layers in CRUST 5.1 and CRUST 2.0 are divided into two layers of soft and hard sediments, while CRUST 1.0 consist of three sediment layers namely, upper, middle and lower sediments. Each  $1^0 \times 1^0$  cell of CRUST 1.0 provides, thickness, compressional and shear wave velocity and density for eight layers: water, ice, three sediment layers and three crustal layers. Topography, bathymetry and

ice cover are taken from the  $1' \times 1'$  ETOPO1 model (Amante and Eakins, 2009). Chen and Tenzer (2014) compiled the Earth's Spectral Crustal Model (ESCM80) by incorporating more detailed information on the topography, bathymetry, polar ice sheets and geoid surface into the CRUST 1.0 model.

Beside the global models, there are some regional models of the crust available in the literature (e.g., Magdala et al., 2008, Grad et al., 2009, Tedla et al., 2011, Van der Meijde et al., 2013 and Mariani et al., 2013). The model developed by Magdala et al. (2008) is termed as Eucrust-07. The model is  $15' \times 15'$  point spacing for download and it is based on the results of seismic reflection, refraction and receiver functions studies. The Moho model of the European plate developed by Grad et al. (2009) has a point spacing of  $0.1^{\circ}$  degree and is compiled using more than 250 data sets of seismic profiles, 3-D models obtained by body and surface waves, receiver function results and maps of seismic and gravity data. Recently a regional model of the Moho for South America has been published by Van der Meijde et al. (2013). This model is based upon the EIGEN-6C (Förste et al. (2011)) model derived from GOCE satellite and other gravity data. The authors inverted the gravity data by assuming a two-layer model with constant density contrast over the interface. The point spacing of the model is  $15' \times 15'$ . The regional model developed for the crustal thickness of Africa is derived from global gravity field data using Euler deconvolution (Tedla et al. (2011)). The model has a point spacing of  $3' \times 2.5'$ . The model is based on EIGEN-GL04C (Foerste et al. (2008)) free air gravity anomalies which contain 30 months of GRACE Level 1B data covering the period from February 2003 to July 2005 together with surface gravity data from seven different sources. More recently, Tugume et al. (2013) developed a regional crustal model for Precambrian Crustal Structure in Africa and Arabia (PCSAA). The Model of crust thickness for Africa and Arabia is based on the gravity data from EIGEN-6C gravity field model.

In our research, we use thickness and boundary layers and density from the recently published CRUST 1.0 model. We compute the gravitational attraction (stripping correction) and potential using forward modeling technique with data from CRUST 1.0 model. We use the above mentioned regional models of the Moho for the validation of our developed Moho model results (in Chapter 7).

## 2.5 Gravitational potential of a solid body

According to Newton's law of gravitation, the gravitational potential  $W_a$  of an attracting body with density  $\rho$  is given by the Newton integral (Mader, 1951)

$$W_a(x, y, z) = G \iiint_v \frac{\rho(x', y', z')}{\sqrt{(x-x')^2 + (y-y')^2 + (z-z')^2}} dx' dy' dz' \quad (2.1)$$

over the volume  $v$  of the body, where  $G$  is the Newtonian gravitational constant,  $dv = dx' dy' dz'$  is the volume element, and  $l = \sqrt{(x-x')^2 + (y-y')^2 + (z-z')^2}$  is the euclidean distance between the computation point  $(x, y, z)$  and integration point  $(x', y', z')$ .

The potential  $W_a$  is continuous throughout the space and for  $l \rightarrow \infty$  it behaves like the potential generated by a point mass located at the body's centre of mass. The first derivatives of the potential are also continuous throughout the space but the second derivatives are not continuous at density discontinuities (Kellogg, 1929). It can be shown that

$$\Delta W_a = -4\pi G\rho, \quad (2.2)$$

where  $\Delta = \frac{\partial^2}{\partial x^2} + \frac{\partial^2}{\partial y^2} + \frac{\partial^2}{\partial z^2}$  is the Laplacian operator. Outside the surface of the body the density  $\rho$  is zero, so Eq. (2.2) turns into

$$\Delta W_a = 0. \quad (2.3)$$

Eq. (2.3) is called the Laplace equation and its solutions are called harmonic functions.

## 2.6 Earth gravity and geoid

The total force acting on an object located at the surface of the Earth is the sum of gravitational force and centrifugal force. The centrifugal potential is

$$\Phi(x, y, z) = \frac{1}{2}\omega^2(x^2 + y^2),$$

where  $\omega$  is the angular velocity of the Earth's rotation and  $x, y, z$  are the coordinates defined in an Earth-fixed reference frame. The gravity potential  $W$  is the sum of the Earth gravitational potential  $W_a$  and the centrifugal potential  $\Phi$ :

$$W(x, y, z) = W_a(x, y, z) + \Phi(x, y, z). \quad (2.4)$$

The gravity vector  $\mathbf{g}$  is the gradient of the gravity potential (Moritz, 2006):

$$\mathbf{g} = \nabla W, \quad (2.5)$$

with components

$$\begin{aligned} g_x &= \frac{\partial W}{\partial x} = -G \iiint_v \frac{x-x'}{l^3} dx' dy' dz' + \omega^2 x, \\ g_y &= \frac{\partial W}{\partial y} = -G \iiint_v \frac{y-y'}{l^3} dx' dy' dz' + \omega^2 y, \\ g_z &= \frac{\partial W}{\partial z} = -G \iiint_v \frac{z-z'}{l^3} dx' dy' dz', \end{aligned}$$

where  $\nabla = \frac{\partial}{\partial x} \hat{i} + \frac{\partial}{\partial y} \hat{j} + \frac{\partial}{\partial z} \hat{k}$ , and  $\hat{i}$ ,  $\hat{j}$  and  $\hat{k}$  are the unit vectors in the terrestrial reference frame along the  $x$ ,  $y$  and  $z$  direction, respectively. The magnitude of the gravity vector

$$g = |\nabla W| \quad (2.6)$$

is called gravity.

Surface  $W = \text{constant}$  is called the geops, and one particular geops  $W = W_0$ , is the geoid. It is the geops which best approximates mean sea level.

The force of gravity at the geoid surface is always normal to it. The gravity potential  $W$  can be split into the normal potential  $U$  usually generated by a level ellipsoid and the disturbance potential  $T$ :

$$W = U + T.$$

Thus, the disturbance potential is defined as the difference between the actual gravity potential and the normal gravity potential. In geodetic coordinates, it can

be written as

$$T(h, \lambda, \phi) = W_a(h, \lambda, \phi) - U_a(h, \phi). \quad (2.7)$$

where  $h$  is the ellipsoidal height,  $\lambda$  is the longitude and  $\phi$  is the latitude. The gradient of the normal potential is called the normal gravity vector

$$\vec{\gamma} = \vec{\nabla} U,$$

and its magnitude is called the normal gravity

$$\gamma = |\vec{\nabla} U|.$$

## 2.7 Gravity disturbance and gravity anomaly

The gradient of the disturbance potential is called the gravity disturbance vector and is denoted by  $\delta g$  (Moritz, 2006):

$$\delta g = \vec{\nabla}(W - U) = \vec{\nabla} T,$$

and the difference in magnitude is the gravity disturbance (Moritz, 2006)

$$\delta g = |\vec{\nabla} W| - |\vec{\nabla} U| = g_P - \gamma_P. \quad (2.8)$$

The classical gravity anomaly vector  $\Delta g$  is defined as the difference between the gravity vector  $g_P$  at a point  $P$  on the geoid and the normal gravity vector  $\gamma_Q$  at the corresponding point on the reference ellipsoid (see Figure 2.1):

$$\Delta g = g_P - \gamma_Q,$$

and the difference in magnitude is the gravity anomaly

Now consider the geometrical representation of geoid and reference ellipsoid as given in Figure 2.1, where  $n$  is the local normal at  $P$  while  $n'$  is the normal to the reference ellipsoid at  $Q$  passing through point  $P$  on the geoid. Omitting subscript  $P$  for brevity, the gravity disturbance can be written as

$$\delta g = - \left( \frac{\partial W}{\partial n} - \frac{\partial U}{\partial n'} \right).$$

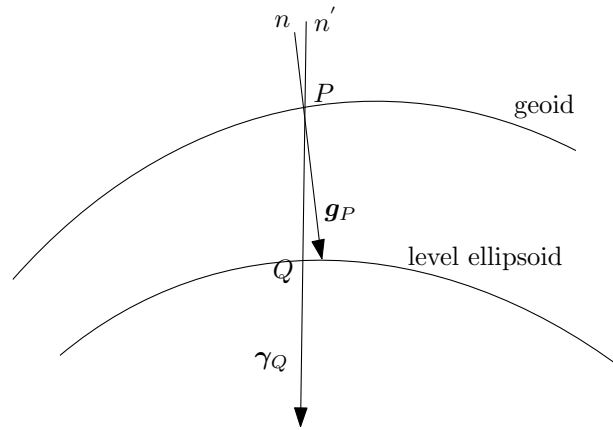


**Figure 2.1** Geometrical representation of geoid and reference ellipsoid

The direction of the normal vectors  $n$  and  $n'$  almost coincide, moreover the normal  $n$  is directed along the elevation  $h$  therefore, gravity disturbance can be approximately written as

$$\delta g \approx -\frac{\partial T}{\partial h}.$$

In spherical approximation, the gravity disturbance is the negative radial derivative of the disturbance potential ([Heiskanen, 1967](#))

$$\delta g \approx -\frac{\partial T}{\partial r} \quad (2.9)$$

and similarly, the expression for the gravity anomaly reads

$$\Delta g \approx -\frac{\partial T}{\partial r} - \frac{2}{r}T. \quad (2.10)$$

Eqs. (2.9) and (2.10) relate gravity disturbances and gravity anomalies to the disturbance potential.

## 2.8 Harmonic expansion of the gravity field

The total potential  $W$  of the Earth can be represented outside a sphere comprising all masses (Brouillon sphere) in term of spherical harmonic (Moritz, 2006)

$$W(r, \theta, \lambda) = \frac{GM}{R} \sum_{l=0}^{\infty} \left(\frac{R}{r}\right)^{l+1} \sum_{m=0}^l \left(\bar{C}_{lm} \cos m\lambda + \bar{S}_{lm} \sin m\lambda\right) \bar{P}_{lm}(\cos\theta) + \frac{1}{2}\omega r^2 \sin^2\theta, \quad (2.11)$$

where  $G = 6.674 \times 10^{-11} m^3 kg^{-1} s^{-2}$  is Newton's gravitational constant, and  $M$  is the mass of the Earth. The numerical value of the scaling terms  $\{GM, R\}$  are:  $GM = 3986004.415 \times 10^8 m^3 s^{-2}$  and  $R = 6378136.3m$ ,  $\theta$  is co-latitude,  $\lambda$  is longitude,  $\bar{C}_{lm}$  and  $\bar{S}_{lm}$  are the fully normalised spherical harmonic coefficients (Stokes coefficients),  $l$  is degree and  $m$  is the order.  $\bar{P}_{lm}$  are normalized associated Legendre's functions of degree  $l$  and order  $m$ ; they are defined by (Moritz, 2006)

$$\bar{P}_{lm} = \begin{cases} \sqrt{2l+1} P_{lm} & \text{if } m = 0 \\ \sqrt{2(2l+1) \frac{(l-m)!}{(l+m)!}} P_{lm} & \text{if } m \neq 0 \end{cases}$$

Similarly, the normal potential can be written as

$$U(r, \theta, \lambda) = \frac{GM}{R} \sum_{l=0(2)}^{\infty} \left(\frac{R}{r}\right)^{l+1} \bar{C}_{l0}^U \bar{P}_{l0}(\cos\theta) + \frac{1}{2}\omega r^2 \sin^2\theta. \quad (2.12)$$

The summation over  $l$  has a step size of 2. Using Eq. (2.11) and Eq. (2.12), one can express the disturbance potential as

$$T(r, \theta, \lambda) = \frac{GM}{R} \sum_{l=2}^{\infty} \left(\frac{R}{r}\right)^{l+1} \sum_{m=0}^l \left(\Delta\bar{C}_{lm} \cos m\lambda + \Delta\bar{S}_{lm} \sin m\lambda\right) \bar{P}_{lm}(\cos\theta), \quad (2.13)$$

where

$$\begin{bmatrix} \Delta\bar{C}_{lm} \\ \Delta\bar{S}_{lm} \end{bmatrix} = \begin{bmatrix} \bar{C}_{lm} - C_{lm}^U \\ \bar{S}_{lm} - S_{lm}^U \end{bmatrix}.$$

Assuming that the total mass of the level ellipsoid is the same as the mass of the Earth, the zero degree term vanishes (i.e.,  $\Delta\bar{C}_{00} = \bar{S}_{00} = 0$ ). Furthermore,



assuming that the centre of mass of the Earth and the level ellipsoid coincide with the origin of coordinate system, the disturbance potential vanishing degree 1 terms (i.e.,  $\bar{C}_{11} = \bar{C}_{10} = \bar{S}_{11} = 0$ ).

Eq. (2.13) can be written for a points at the mean sphere, which approximates the Earth's surface of radius  $r = R$ :

$$T(R, \theta, \lambda) = \sum_{l=2}^{\infty} \sum_{m=0}^l \left( \Delta \bar{C}_{lm}^T \cos m\lambda + \Delta \bar{S}_{lm}^T \sin m\lambda \right) \bar{P}_{lm}(\cos \theta),$$

where

$$\begin{bmatrix} \Delta \bar{C}_{lm}^T \\ \Delta \bar{S}_{lm}^T \end{bmatrix} = \frac{GM}{R} \begin{bmatrix} \Delta \bar{C}_{lm} \\ \Delta \bar{S}_{lm} \end{bmatrix} \quad (2.14)$$

are the Stokes coefficients associated with the disturbance potential of the Earth. From Eq. (2.9) and Eq. (2.10) it follows that the expressions for gravity disturbances and gravity anomalies on the sphere with radius  $r = R$  are

$$\delta g(R, \theta, \lambda) = \frac{GM}{R^2} \sum_{l=2}^{\infty} (l+1) \sum_{m=0}^l \left( \Delta \bar{C}_{lm} \cos m\lambda + \Delta \bar{S}_{lm} \sin m\lambda \right) P_{lm}(\cos \theta) \quad (2.15)$$

and

$$\Delta g(R, \theta, \lambda) = \frac{GM}{R^2} \sum_{l=2}^{\infty} (l-1) \sum_{m=0}^l \left( \Delta \bar{C}_{lm} \cos m\lambda + \Delta \bar{S}_{lm} \sin m\lambda \right) P_{lm}(\cos \theta), \quad (2.16)$$

respectively. From Eq. (2.15) and (2.16) it follows that the expression for the corresponding Stokes coefficient of the gravity disturbances and gravity anomalies are

$$\begin{bmatrix} \Delta \bar{C}_{lm}^{\delta g} \\ \Delta \bar{S}_{lm}^{\delta g} \end{bmatrix} = \frac{GM}{R^2} (l+1) \begin{bmatrix} \Delta \bar{C}_{lm} \\ \Delta \bar{S}_{lm} \end{bmatrix}, \quad (2.17)$$

and

$$\begin{bmatrix} \Delta \bar{C}_{lm}^{\Delta g} \\ \Delta \bar{S}_{lm}^{\Delta g} \end{bmatrix} = \frac{GM}{R^2} (l-1) \begin{bmatrix} \Delta \bar{C}_{lm} \\ \Delta \bar{S}_{lm} \end{bmatrix}, \quad (2.18)$$

respectively.

## 2.9 Global gravity field model

In April 2008, the National Geospatial-Intelligence Agency (NGA) released “the Earth Gravitational Model 2008” (EGM2008) (Pavlis et al., 2008). The model is complete to spherical harmonic degree and order 2159. It is a combined model based on information from CHAMP, GRACE satellite gravity missions as well as a global gravity anomaly database. In April 2011, a new combined global gravity field model EIGEN-6C (Förste et al., 2011) had been developed by GeoForschungsZentrum Potsdam and Groupe de Recherche de Geodesie Spatiale (GRGS) Toulouse. The EIGEN-6C gravity model is complete to the spherical harmonic degree and order 1420 and it is based on the data from CHAMP, GRACE, GOCE satellite gravity missions and terrestrial global gravity anomaly data provided by the Danish Technical University (DTU10 gravity model) (Anderson et al. 2009, Anderson 2010). Recently, EIGEN-6C2, a new combined global gravity field model complete to degree and order 1949 (10 km spatial resolution) is released by GFZ Potsdam and GRGS Toulouse (Förste et al., 2013). The EIGEN-6C2 model is based on data from GOCE together with data from previous satellite gravity missions, and surface gravity data from DTU10. These high-resolution, high-accuracy, and combined modern gravity models offer new opportunities to study different interfaces and the dynamics of various processes which occur inside the Earth.

The improved resolution and accuracy of available gravity field models enhance the interest of researchers to studies the interior of the Earth structure in detail especially in region where limited or inhomogeneous seismic data is available. These models provides an opportunity for improving our knowledge of basic crustal structure of the Earth.

## 2.10 Isostasy and crust models

The term Isostasy is used to describe the state of equilibrium to which the Earth lithosphere and asthenosphere tend, in the absence of external disturbance forces.

The alternative view of isostasy is the Archimedes principle of hydrostatic equilibrium. According to this principle, a lighter solid body always floats on the denser underlying fluid. From the hydrostatic equilibrium, the pressure generated by the column of the Earth crust at a given depth of compensation at the underlying mantle is constant, otherwise a lateral pressure gradient occurs, which causes the mantle material to move until a constant pressure condition is reached. The theory of isostasy states that a distribution of hydrostatic pressure exists below the surface of compensation (Torge, 1991).

The theory of isostasy is in line with the observation that the global Bouguer anomalies (free air gravity anomaly corrected for the effect of the topography above the geoid) have a systematic pattern over the globe. It is generally positive in the oceanic regions, mostly negative in the continental regions and shows strong correlation with the topographic heights. This means that the mass excess and deficiency are at least partially compensated by the corresponding mass distribution inside the Earth. According to the isostasy principle, the mass of mountains must be compensated by a mass deficit below it, while the mass deficit at an ocean basin must be compensated by an extra mass at depth. In the mid of the nineteenth century, two compensation mechanisms were proposed by Airy and Pratt.

1. The Airy model is based on constant density, where different topographic heights are compensated by changes in the lithospheric thickness (Airy, 1855, Heiskanen, 1958).
2. The Pratt model, where different topographic heights are compensated by lateral changes in the lithospheric density (Pratt, 1855, Hayford, 1909a, Hayford and Bowie, 1912).

### Airy isostatic model

Figure 2.2a illustrates the Airy isostatic model. The Airy model is based on a constant density  $\rho_0$  and varying thickness of crust columns (Torge, 1991).  $T_0$  is the thickness of normal column of crust which has the height  $H = 0$  above sea level. The continental column of mountain height  $H$  forms mountain roots of thickness  $d_{cont}$  beneath the normal column of crust, and the oceanic column of depth  $t$  forms anti-roots with thickness  $d_{ocean}$  beneath the oceanic column.

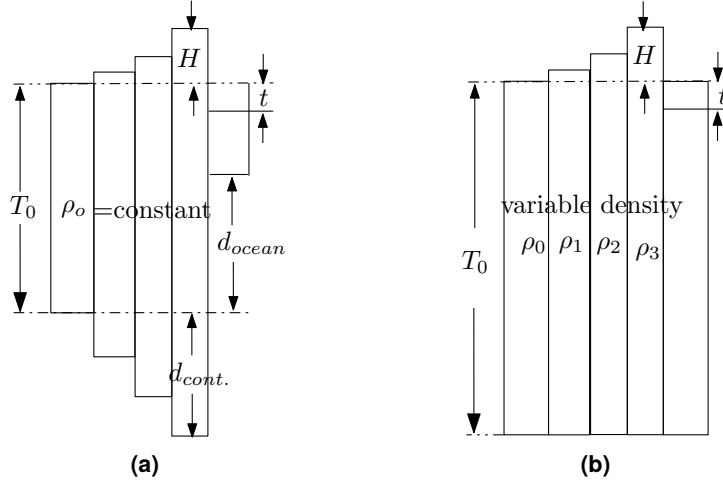


**Figure 2.2** (a) Isostatic model of Airy (b) Isostatic model of Pratt

According to the isostatic condition, the pressure  $p$  produced by a column of homogeneous density is given by

$$p = \frac{\text{weight}}{\text{area}} = \frac{\rho_0 g V}{\Delta S} = \rho_0 g h = \text{constant},$$

where  $g$  is gravity,  $V$  is the volume of the column,  $\Delta S$  is the column area,  $\rho_0$  is the column density and  $h$  is the total column thickness. If  $\rho_m$  and  $\rho_w$  represent the density of mantle and sea water, respectively, then the pressure exerted by the normal column having height  $H = 0$  is given by

$$p = \rho_0 g T_0 + \rho_m g d_{cont} \quad (2.19)$$

and pressure exerted by the continental column of mountain height  $H$  is given as

$$p = \rho_0 g H + \rho_0 g T_0 + \rho_0 g d_{cont}. \quad (2.20)$$

Similarly, for the oceanic column we have,

$$p = \rho_w g t + \rho_m g (d_{ocean} + d_{cont}) + \rho_0 g (T_0 - t - d_{ocean}) \quad (2.21)$$

According to the condition of hydrostatic equilibrium, from Eqs. (2.19) and (2.20) we get

$$(\rho_m - \rho_0) d_{cont} = \rho_0 H \quad (2.22)$$

for the continents equilibrium. Using Eqs. (2.19) and (2.21) we get

$$(\rho_m - \rho_0)d_{ocean} = (\rho_o - \rho_w)t \quad (2.23)$$

for oceanic equilibrium. Using the conventional values for the homogeneous density  $\rho_0 = 2670 \text{ kg/m}^3$ , mantle density  $\rho_m = 3270 \text{ kg/m}^3$ , and density of water  $\rho_w = 1030 \text{ kg/m}^3$  the relation for the thickness of the roots and anti-roots are given by,  $d_{cont} = 4.45H$ ,  $d_{ocean} = 3.72t$ , respectively.

The isostatic phenomena have a direct link with the observed gravity field of the Earth. The thickness  $T_0$  of the normal column of crust can be estimated using isostatic gravity anomalies obtained for different depths of compensation. Generally, for the depth of compensation equal to  $T_0=30$  to 40 km the gravity anomalies are independent of topographic height. This result is in line with the result from seismic studies, which show that the isostatic surface of compensation can be approximated by the Mohorovičić discontinuity.

### Pratt isostatic model

The Pratt model is based on the layer of constant thickness  $T_0$  with lateral variations in crust density  $\rho$  (Torge, 1991). The isostatic model of Pratt is illustrated in Figure 2.2b. The normal column of height  $H = 0$ , has a density  $\rho_0$ , continental columns have smaller densities, while oceanic columns have higher densities. According to the Pratt model the equilibrium condition can be written as

$$\rho_0 T_0 = \rho_{cont}(T_0 + H), \quad \text{for continents}$$

and

$$\rho_0 T_0 = \rho_w t + \rho_{ocean}(T_0 - t), \quad \text{for oceans.}$$

Using the values  $\rho_{cont} = 2670 \text{ kg/m}^3$ ,  $\rho_w = 1030 \text{ kg/m}^3$  for the normal crust density and sea water density, respectively, the relation for the densities of the continental column and oceanic column can be written as

$$\rho_{cont} = 2670 \frac{T_0}{T_0 + H},$$

and

$$\rho_{ocean} = \frac{2670T_0 - 1030t}{T_0 - t},$$

respectively.

Both Airy and Pratt isostatic models are based on local compensation. They assume that the compensation takes place along the vertical columns. In 1931, Vening Meinesz modified the Airy isostasy theory and introduced a regional instead of a local compensation. In this model the topography is considered as a load on unbreakable but yielding elastic crust. [Moritz \(2006\)](#) summarised the two models as, “*standing on the thin ice sheet, Airy will break through, but under Vening Meinesz ice is stronger and will bend but not break*”.

## 2.11 Gravimetric methods for the Moho geometry

Classical isostatic models are typically not able to model realistically the actual Moho geometry. First of all, this is because the isostatic mass balance depends on loading and effective elastic thickness, rigidity, rheology of the lithosphere and viscosity of the asthenosphere ([Watts, 2001](#)). Moreover, the glacial isostatic adjustment, present-day glacial melting, plate motion, mantle convection and other geodynamic processes contribute to the overall isostatic balance. [Kaban et al. \(1999\)](#), for instance, demonstrated that the isostatic mass balance takes place not only within the crust but essentially within the whole lithosphere (see [Kaban et al., 2004](#), [Tenzer et al., 2009a, 2012b](#)). Gravity data also contain a long-wavelength signal from mantle heterogeneities including the core-mantle geometry ([Sjöberg, 2009](#)). Therefore, gravimetric methods should optimally combine gravity and seismic data. An example of the combined data processing strategy is the study of [Braitenberg \(1999\)](#). They proposed a method based on the iterative 3-D gravity inversion with integrated seismic data for the Moho recovery.

Generally, seismic data are used in geophysical studies to determine the Moho geometry. Seismic methods provide a more realistic image of the Moho interface. However, due to the limited coverage of seismic observation, their application for the recovery of the Moho interface is difficult. In the absence or a low coverage with seismic data, gravimetric or combined gravimetric-seismic methods have to be used. Several gravimetric methods for finding the Moho depths have been developed and

applied in global and regional studies. Examples of the gravimetric methods include, but are not limited to, studies by [Oldenburg \(1974\)](#), [Cadek and Martinec \(1991\)](#), [Arabelos et al. \(2007\)](#), [Sjöberg \(2009\)](#), [Braitenberg et al. \(2010\)](#), [Sampietro \(2011\)](#), [Bagherbandi \(2012\)](#), [Bagherbandi and Eshagh \(2012\)](#), [Bagherbandi et al. \(2013\)](#), [Tenzer et al. \(2013\)](#).

**Parker method of gravity inversion:** The relation between Bouguer gravity anomalies  $\Delta g^B$  and the depth of an interface  $h(r)$  is given by [Parker \(1973\)](#)

$$F(\Delta g^B) = -2\pi G \Delta \rho e^{-|k|h_0} \sum_{l=1}^{\infty} \frac{|k|^{l-1}}{l!} F[h^l(\bar{r})], \quad (2.24)$$

where  $F(\Delta g)$  is the Fourier transform of the gravity anomalies,  $k$  is the wave number,  $h(r)$  is the interface depth,  $h_0$  is the mean depth of horizontal interface, and  $\bar{r}$  is the projection of the position  $r = (x, y, z)$  onto  $x - y$  plane. [Oldenburg \(1974\)](#) rearranged the above Parker's relation to

$$F[h(\bar{r})] = -\frac{F[\Delta g^B(\bar{r})] e^{-|k|h_0}}{2\pi \Delta \rho} - \sum_{l=2}^{\infty} \frac{|k|^{l-1}}{l!} F[h^l(\bar{r})]. \quad (2.25)$$

Eq. (2.25) can be used to compute the regional Moho depth from gravity anomalies iteratively,

The regional compensation model was adopted in the Parker-Oldenburg isostatic method ([Oldenburg, 1974](#)). [Moritz \(1990\)](#) utilized the Vening Meinesz inverse problem of isostasy for the Moho depth estimation. [Sjöberg \(2009\)](#) reformulated Moritz's problem, called herein the Vening Meinesz-Moritz (VMM) problem of isostasy, as that of solving a non-linear Fredholm integral equation of the first kind.

The isostatic mass balance is described commonly in terms of isostatic gravity anomalies. [Vajda et al. \(2007\)](#), however, argued that the definition of gravity disturbances was theoretically more appropriate in the context of gravimetric studies. Following this concept, [Tenzer and Bagherbandi \(2012\)](#) reformulated the VMM inverse problem of isostasy in terms of the isostatic gravity disturbances; see also [Bagherbandi et al. \(2013\)](#). They also demonstrated that the Moho depths from isostatic gravity disturbances better agreed with global seismic models than those based on isostatic gravity anomalies. The concept of isostatic gravity disturbances is used also for global lithospheric studies in ([Kaban et al., 1999, 2003, 2004](#))

Least-squares inversion of gravity data can be used to determine the Moho depth. It leads to an ill-posed problem due to lack of uniqueness. The non-uniqueness can be overcome if we take into account some restrictive assumptions to the density distribution. Normally, these assumptions are provided from the geology of the study area as well as from seismic sources. Furthermore, the Bouguer gravity should be corrected for the known short and long wavelength effects. The short wavelength signal are due to heterogeneities of the crust, while the long-wavelength are due to the deeper structure heterogeneities.

The geophysical inversion consists of two processes, one is called the forward process (method) and the other the inverse process. Before the inversion, the effects of shallow structures on the observed gravity must be removed, to obtain the gravity associated with the structures and Moho geometry. For this purpose the forward modeling technique have been used. Furthermore, for the Moho recovery, the gravity signal associated with deep structure deeper than the Moho must also be removed. For example, to remove the effects of topography, the Bouguer reduction is applied to the gravity data. In Bouguer reduction the gravitational attraction of a Bouguer plate of height  $h$  and density  $\rho$ , is subtracted from the observed gravity anomaly, i.e.,

$$\Delta g^B = \Delta g - 2\pi G \rho h.$$

The methodology used for the forward modeling of gravity signal is addressed in Chapters 3 and 4, while the inverse problem for the recovery of Moho is given in Chapter 6.

## 2.12 Vening Meinesz's Model (VMM)

Vening Meinesz's inverse problem deals with the recovery of the Moho depth  $h$ , using Bouguer gravity anomalies and the normal Moho depth  $h_0$  (mean Moho depth). Adopting the principle of solving Moritz's generalization of the Vening-Meinesz inverse problem of isostasy is based on generating the isostatic gravity disturbances/anomalies, such that these are equal to zero. The formulated problem is under the assumption of varying Moho depths  $h$ , and adopting a constant value of the Moho density contrast  $\Delta\rho = \rho_m - \rho_c$ ; where  $\rho_c$  and  $\rho_m$  denote the constant density of the Earth's crust and the uppermost mantle respectively (cf. [Vening Meinesz](#),



1931). The isostatic gravity disturbances  $\delta g^i$  at a position  $(r, \Omega)$  is then defined as (cf. [Tenzer and Bagherbandi, 2012](#))

$$\delta g^i(r, \Omega) = \delta g^{cs}(r, \Omega) + g^c(r, \Omega) = 0 \quad (2.26)$$

where  $\delta g^{cs}$  is the crust-stripped gravity disturbance,  $\Omega = (\phi, \lambda)$  denotes the spherical direction with spherical latitude  $\phi$  and longitude  $\lambda$ , and  $g^c$  is the gravitational attraction of isostatic compensation masses (e.g., [Moritz, 1990](#)), which fully compensate the crust-stripped gravity disturbances ( $\delta g^{cs}$ ). It can be written as (cf. [Sjöberg, 2009](#))

$$g^c = g_0^c + dg^c, \quad (2.27)$$

where

$$g_0^c = G\Delta\rho \iint_{\Omega'} \int_R^{R-h_0} \frac{r'^2(r-r'\cos\psi)}{l^3} dr' d\Omega'$$

and

$$dg^c = G\Delta\rho \iint_{\Omega'} \int_{R-h}^R \frac{r'^2(r-r'\cos\psi)}{l^3} dr' d\Omega', \quad (2.28)$$

where  $G$  is Newton's gravitational constant,  $R$  is the radius of a mean Earth sphere,  $r$  and  $r'$  are the distance from computation point and integration point, respectively,  $d\Omega' = \cos\phi' d\phi' d\lambda'$ ,  $\phi' \in [-\frac{\pi}{2}, \frac{\pi}{2}]$ ,  $\lambda' \in [0, 2\pi]$ ,  $\psi$  is the spherical distance between two points  $(r, \Omega)$  and  $(r', \Omega')$ , and  $l = \sqrt{r^2 + r'^2 - 2rr'\cos\psi}$ . From Eqs. (2.26), (2.27) and (2.28), we obtain

$$G\Delta\rho \iint_{\Omega'} \int_{R-h}^R \frac{r'^2(r-r'\cos\psi)}{l^3} dr' d\Omega' = -[\delta g^{cs} + g_0^c]$$

[Sjöberg \(2009\)](#) simplifies the above equation and formulates the VMM inverse problem of isostasy in the following generic form

$$-GR\Delta\rho \iint K(\psi, s) d\Omega' = f(r, \Omega) \quad (2.29)$$

where  $f(r, \Omega) = -[\delta g^{cs} + g_0^c]$ , the integral kernel  $K(\psi, s)$  in Eq. (2.29) is a function of parameters  $\psi$  and  $s$ ; and  $s = 1 - \frac{h}{R}$ . The spectral representation of  $K(\psi, s)$  reads (cf. [Sjöberg, 2009](#))

$$K(\psi, s) = \sum_{l=0}^{\infty} \frac{l+1}{l+3} (1-s^{l+3}) P_l(\cos\psi),$$

where  $P_l$  is the Legendre polynomial of degree  $l$ .

The expression given in Eq. (2.29) is a non-linear Fredholm integral equation of the first kind for the unknown Moho depths  $h$ . Its solution for finding the Moho depths was given by [Sjöberg \(2009\)](#) under a second-order approximation:

$$h(\Omega) = h_1(\Omega) + \frac{h_1^2(\Omega)}{R} - \frac{1}{32\pi R} \iint \frac{h_1^2(\Omega') - h_1^2(\Omega)}{\sin \frac{\psi}{2}} d\Omega' \quad (2.30)$$

The term  $h_1$  is given in the spectral domain using the following expression

$$h_1(\Omega) = \sum_{l=0}^{\infty} \left(2 - \frac{1}{l+1}\right) \sum_{m=-l}^l f_{l,m} Y_{l,m}(\Omega)$$

The coefficients  $f_{l,m}$  of the isostatic gravity disturbance functional  $f(r, \Omega)$  are defined as

$$f_{l,m} = \frac{1}{4\pi G \Delta \rho} \begin{cases} \delta g_{0,0}^{cs} - g_0^c & \text{if } l = 0 \\ \delta g_{l,m}^{cs} & \text{otherwise} \end{cases}$$

where  $\delta g_{l,m}^{cs}$  are the spherical harmonics coefficients of the crust stripped gravity disturbance  $\delta g^{cs}$ . The nominal compensation attraction (of zero-degree)  $g_0^c$  stipulated at the sphere of radius  $R$  is given by (cf. [Sjöberg, 2009](#))

$$g_0^c \simeq -4\pi G \Delta \rho h_0,$$

where  $h_0$  is the adopted global mean Moho depth.

---

## Analytical and semi-analytical methods for computing gravitational attraction and potential

An inhomogeneous density distribution inside the Earth (for example the bathymetry, ice and sedimentary layers effects) require that the corresponding signals are removed from gravity field data. Furthermore, one has to compute the effect of topographic masses above the geoid. The link between density distribution and gravitational attraction/potential is provided by the Newton volume integral. Various numerical methods are applied to evaluate the Newton's volume integral when studying the local gravity field. A simple form of the integration can be used, such as splitting the integration volume into right rectangular parallelepipeds (prisms) with constant density within each individual prism. [Bessel \(1813\)](#) derived a closed analytical expression for the gravitational potential of a prism. The potential-related formulae for a prism were studied also by [Zach \(1811\)](#), [Mollweide \(1813\)](#), [Everest \(1830\)](#) and [Mader \(1951\)](#). [Nagy et al. \(2000\)](#) summarized the closed analytical expressions for the potential and its first and second derivatives of a rectangular prism of homogeneous density. However, in most geological structures the constant density assumption is not practical. For this reason, some authors derived analytical expressions for volume elements with linearly or otherwise varying density distribution models. [Chai \(1988\)](#) computed gravity anomalies using a rectangular prism with density changing linearly with depth. [Gallardo-Delgado et al. \(2003\)](#) derived the analytical solution for the forward gravity modeling utilizing a rectangular prism with density varying according to a quadratic polynomial law. [García-Abdeslem](#)

(1992, 2005) introduced the analytical expression for the rectangular prism with depth dependent density distribution in the form of a cubic polynomial.

For efficient gravity field modeling of homogeneous/inhomogeneous density formations, the approximation of geological structures by more general geometrical forms than rectangular prisms has to be implemented. [Hubbert and King \(1948\)](#) introduced a methodology called the line integral approach; the surface or volume integrals are converted to line integrals after applying the Gauss divergence theorem. Following this idea, [Talwani et al. \(1959\)](#) applied the line integral approach to the polygon in 2-D. [Talwani and Ewing \(1960\)](#), [Collette \(1965\)](#) and [Takin and Talwani \(1966\)](#) decomposed the 3-D body into parallel, typically horizontal laminae. [Paul \(1974\)](#) and [Barnett \(1976\)](#) generalised this concept for a polyhedron in 3-D. [Pohánka \(1988\)](#) derived a simple algorithm for the attraction of a homogeneous polyhedral body using the line integral approach (see also [Pohánka, 1990](#), [Ivan, 1990](#)). The formulae for polyhedral bodies with homogeneous density were studied also by [Okabe \(1979\)](#), [Götze and Lahmeyer \(1988\)](#), [Kwok \(1991\)](#), [Holstein and Ketteridge \(1996\)](#), [Werner and Scheeres \(1996\)](#), [Holstein et al. \(1999\)](#) and [Holstein \(2002a,b\)](#). [Petrović \(1996\)](#) presented in more complete form the formulae for the potential and its derivatives using the line integral approach for arbitrary polyhedral bodies of homogeneous density (see also [Tsoulis and Petrović, 2001](#)).

Combining the benefits of using more generalized geometrical bodies, [Pohánka \(1988\)](#) introduced an optimum expression for the computation of gravity field (gravitational attraction) of a constant homogeneous density polyhedral body by means of line integrals. To avoid singular terms and obtain a maximal numerical accuracy and efficiency, [Pohánka \(1998\)](#) derived the optimum expression and proposed a simple computational algorithm for computing the gravity field (attraction) of a polyhedral body with linearly increasing density. An alternative expression was derived by [Hansen \(1999\)](#) for the gravitational attraction of a polyhedral body with linearly varying density. In gravimetric geoid modeling and related subjects not only the attraction-related term (direct effect) but also the potential-related terms (secondary indirect effects) are computed. Therefore, [Holstein \(2003\)](#) generalized their work having derived formulae also for the gravitational potential and its second derivatives.

Following the concept used by [Pohánka \(1988, 1998\)](#) in this chapter we derive the expression for computing the gravitational potential of an arbitrary polyhedral

body having a linearly varying density. Due to the singularities, the methods used for computing the gravitational attraction and potential need special attention. They arise depending on the location of computation point relative to the object. In comparison to the formula for the potential given by [Holstein \(2003\)](#), the main advantage of our approach is adopting the computational strategy developed by [Pohánka \(1988, 1998\)](#), so that our expressions have no singular terms. Furthermore, we propose a numerical scheme which efficiently combines various existing methods of solving the Newton's volume integral. We start this chapter from an overview of existing methods, the simple method using point mass approach (Section 3.1), then Gauss cubature (Section 3.2), then linear vertical mass approach (Section 3.3), then rectangular prism approach (Section 3.4) and finally using line integral analytical approach. The potential of an arbitrary polyhedral body having a linearly varying density is derived in Section 3.5. At the end we describe numerical experiments where the above mentioned methods are compared. We present our result over computational accuracy and efficiency of the methods in a graphical and tabulated form.

### 3.1 Point Mass Approach

A simple point mass approach can be applied to compute gravitational potential  $V(x, y, z)$  and the component of gravitational attraction  $g_x$ ,  $g_y$  and  $g_z$ . Consider a homogeneous rectangular prism having boundary from  $x'_1$  to  $x'_2$  along the x-axis, from  $y'_1$  to  $y'_2$  along y-axis and from  $z'_1$  to  $z'_2$  along z-axis. Using the most simple approximation of the gravitational potential of a prism is to replace it by a point mass located at the geometric centre of the prism:

$$V(x, y, z) = G \rho |\bar{l}|^{-1} (x'_2 - x'_1) (y'_2 - y'_1) (z'_2 - z'_1) \quad (3.1)$$

where  $\bar{l} = |\mathbf{r} - \bar{\mathbf{r}}'|$  is the euclidean distance between the computation point  $\mathbf{r}(x, y, z)$  and the geometrical centre of the rectangular prism  $\bar{\mathbf{r}}' = (\bar{x}', \bar{y}', \bar{z}')$ ;  $\bar{x}' = \frac{x'_2 - x'_1}{2}$ ,  $\bar{y}' = \frac{y'_2 - y'_1}{2}$ ,  $\bar{z}' = \frac{z'_2 - z'_1}{2}$ .

The components of gravitational attraction vector will be

$$g_x = G \rho \left[ \frac{(x - \bar{x}')}{|\bar{l}|^3} (x'_2 - x'_1) (y'_2 - y'_1) (z'_2 - z'_1) \right], \quad (3.2)$$

$$g_y = G \rho \left[ \frac{(y - \bar{y}')}{|\bar{l}|^3} (x'_2 - x'_1) (y'_2 - y'_1) (z'_2 - z'_1) \right]$$

$$g_z = G \rho \left[ \frac{(z - \bar{z}')}{|\bar{l}|^3} (x'_2 - x'_1) (y'_2 - y'_1) (z'_2 - z'_1) \right]$$

### 3.2 Gauss Cubature Approach

Gravitational potential of a homogeneous rectangular prism with dimension  $x_1$  to  $x_2$ ,  $y_1$  to  $y_2$ , and  $z_1$  to  $z_2$  is

$$V(\mathbf{r}) = G \rho \int_{x_1}^{x_2} \int_{y_1}^{y_2} \int_{z_1}^{z_2} \frac{1}{|\bar{l}|} dx' dy' dz', \quad (3.3)$$

where  $|\bar{l}| = \sqrt{(x - x')^2 + (y - y')^2 + (z - z')^2}$  is the Euclidean distance between the computation point  $\mathbf{r} = (x, y, z)$  and the integration point  $\mathbf{r}' = (x', y', z')$ . By integrating the right-hand side of Eq. (3.3) with respect to  $z'$  we get

$$V(\mathbf{r}) = -G \rho \int_{x_1}^{x_2} \int_{y_1}^{y_2} \left[ \ln \left[ (z - z') + |\bar{l}| \right] \right]_{z_1}^{z_2} dx' dy'. \quad (3.4)$$

After applying the Gauss cubature discretization, the expression for the gravitational potential of homogeneous rectangular prism is:

$$\begin{aligned} V(\mathbf{r}) = & -\frac{1}{4} G \rho (x'_2 - x'_1) (y'_2 - y'_1) \left[ \left[ f_v(x'_a, y'_a) + f_v(x'_b, y'_b) \right. \right. \\ & \left. \left. + f_v(x'_a, y'_b) + f_v(x'_b, y'_a) \right]_{z'_1}^{z'_2} \right] \end{aligned} \quad (3.5)$$

where the function  $f_v = \ln \left[ (z - z') + |\bar{l}| \right]$  is computed at the four Gauss nodes:

$$x'_a = \frac{x'_1 + x'_2}{2} + \frac{1}{\sqrt{3}} \frac{x'_2 - x'_1}{2}, \quad y'_a = \frac{y'_1 + y'_2}{2} + \frac{1}{\sqrt{3}} \frac{y'_2 - y'_1}{2}$$

$$x'_b = \frac{x'_1 + x'_2}{2} - \frac{1}{\sqrt{3}} \frac{x'_2 - x'_1}{2}, \quad y'_b = \frac{y'_1 + y'_2}{2} + \frac{1}{\sqrt{3}} \frac{y'_2 - y'_1}{2}.$$

The expression for the vertical components of the gravitational attraction vector reads:

$$\begin{aligned} g_x &= -G\rho \int_{x_1}^{x_2} \int_{y_1}^{y_2} ||l|^{-1}|_{z_1}^{z_2} dy' dz' \\ &= -\frac{1}{4}G\rho (y'_2 - y'_1) (z'_2 - z'_1) \left[ \left[ f_g(y'_a, z'_a) + f_g(y'_b, z'_b) \right. \right. \\ &\quad \left. \left. + f_g(y'_a, z'_b) + f_g(y'_b, z'_a) \right]_{x_1}^{x_2} \right], \end{aligned} \quad (3.6)$$

$$\begin{aligned} g_y &= -G\rho \int_{x_1}^{x_2} \int_{y_1}^{y_2} ||l|^{-1}|_{z_1}^{z_2} dx' dz' \\ &= -\frac{1}{4}G\rho (x'_2 - x'_1) (z'_2 - z'_1) \left[ \left[ f_g(x'_a, z'_a) + f_g(x'_b, z'_b) \right. \right. \\ &\quad \left. \left. + f_g(x'_a, z'_b) + f_g(x'_b, z'_a) \right]_{y_1}^{y_2} \right], \end{aligned} \quad (3.7)$$

$$\begin{aligned} g_z &= -G\rho \int_{x_1}^{x_2} \int_{y_1}^{y_2} ||l|^{-1}|_{z_1}^{z_2} dx' dy' \\ &= -\frac{1}{4}G\rho (x'_2 - x'_1) (y'_2 - y'_1) \left[ \left[ f_g(x'_a, y'_a) + f_g(x'_b, y'_b) \right. \right. \\ &\quad \left. \left. + f_g(x'_a, y'_b) + f_g(x'_b, y'_a) \right]_{z_1}^{z_2} \right], \end{aligned} \quad (3.8)$$

where  $f_g = |l|^{-1}$

In Gauss cubature approach one analytical integration ( in the  $z$  direction) and two numerical integrations ( in the  $x$  and  $y$  direction) are used.

### 3.3 Linear Vertical Mass /Semi-analytical Approach

The equations for the vertical mass approach are most easily expressed in terms of spherical coordinates  $(r, \phi, \lambda)$ . The gravitational potential and the vertical component of the gravitational attraction vector generated by a volume element of a sphere having homogeneous density are given by (cf. [Martinec, 1998](#)):

$$\begin{aligned}
 V(\mathbf{r}) = & G \rho \Delta\phi' \Delta\lambda' \cos\phi \left| \frac{1}{2} (|\mathbf{r}'| + 3|\mathbf{r}| \cos\psi) |\mathbf{l}| \right. \\
 & \left. + \frac{1}{2} |\mathbf{r}|^2 (3 \cos^2\psi - 1) \ln \left| \frac{|\mathbf{r}'| \cos\psi + |\mathbf{l}|}{|\mathbf{r}'|} \right| \right|_{r'_1}^{r'_2} \quad (3.9)
 \end{aligned}$$

and

$$\begin{aligned}
 g(\mathbf{r}) = & -G \rho \Delta\phi' \Delta\lambda' \cos\phi \left| |\mathbf{l}|^{-1} (|\mathbf{r}'|^2 + 3|\mathbf{r}|^2) \cos\psi + |\mathbf{l}|^{-1} (1 - 6 \cos^2\psi) |\mathbf{r}| |\mathbf{r}'| \right. \\
 & \left. + |\mathbf{r}| (3 \cos^2\psi - 1) \ln \left| \frac{|\mathbf{r}'| - |\mathbf{r}| \cos\psi + |\mathbf{l}|}{|\mathbf{r}'|} \right| \right|_{r'_1}^{r'_2} \quad (3.10)
 \end{aligned}$$

where  $\phi$  is the latitude,  $\lambda$  is the longitude,  $\psi$  is the spherical angle between computation point  $\mathbf{r}$  and integration point  $\mathbf{r}'$ ,  $\cos\psi = \sin\phi' \sin\phi + \cos\phi' \cos\phi \cos(\lambda' - \lambda)$ ; and the Euclidean distance is computed from:  $|\mathbf{l}| = \sqrt{|\mathbf{r}^2| + |\mathbf{r}'^2| - 2|\mathbf{r}| |\mathbf{r}'| \cos\psi}$ .

### 3.4 Homogeneous Rectangular Prism Method

The rectangular prism method is used when the topography in the region of interest is represented by a regular grid. The method is often used for precise gravity field modeling at the vicinity of the computation point. Eq. (2.1) solved analytically for a homogeneous rectangular prism ([Mader, 1951](#), [Nagy, 1966](#), [Gruninger, 1991](#), [Nagy et al., 2000, 2002](#), [Heck and Seitz, 2007](#)), results in the following formula for the



potential in Cartesian coordinate system:

$$\begin{aligned}
V(x, y, z) = & G \rho \sum_{i=1}^2 \sum_{j=1}^2 \sum_{k=1}^2 (-1)^{i+j+k} \\
& \times \left[ X_i Y_j \ln \left| \frac{Z_k + r_{ijk}}{\sqrt{X_i^2 + Y_j^2}} \right| + Y_j Z_k \ln \left| \frac{X_i + r_{ijk}}{\sqrt{Y_j^2 + Z_k^2}} \right| \right. \\
& + Z_k X_i \ln \left| \frac{Y_j + r_{ijk}}{\sqrt{Z_k^2 + X_i^2}} \right| - \frac{1}{2} \left( X_i^2 \tan^{-1} \frac{Y_j Z_k}{X_i r_{ijk}} \right. \\
& \left. \left. + Y_j^2 \tan^{-1} \frac{Z_k X_i}{Y_j r_{ijk}} + Z_k^2 \tan^{-1} \frac{X_i Y_j}{Z_k r_{ijk}} \right) \right], \quad (3.11)
\end{aligned}$$

with  $X_i = x - x_i$ ,  $Y_j = y - y_j$ ,  $Z_k = z - z_k$  and  $r_{ijk} = \sqrt{X_i^2 + Y_j^2 + Z_k^2}$ .

Here the point  $r(x, y, z)$  is the computational point and  $r(x_i, y_j, z_k)$  are the integration point.

Similarly, the vertical components of the gravitational attraction vector at a point  $r(x, y, z)$  reads (Mader, 1951, Gruninger, 1991, Nagy, 1966, Nagy et al., 2000, 2002, Heck and Seitz, 2007):

$$\begin{aligned}
g_z = & G \rho \sum_{i=1}^2 \sum_{j=1}^2 \sum_{k=1}^2 (-1)^{i+j+k} \times \left[ X_i \ln \left| \frac{Y_j + r_{ijk}}{\sqrt{X_i^2 + Z_k^2}} \right| + Y_j \ln \left| \frac{X_i + r_{ijk}}{\sqrt{Y_j^2 + Z_k^2}} \right| \right. \\
& \left. - Z_k \tan^{-1} \frac{X_i Y_j}{Z_k r_{ijk}} \right]. \quad (3.12)
\end{aligned}$$

The other two components of gravitational attraction vector can be obtained from Eq. ((3.12)) by cyclic permutation, i.e.,

$$\begin{aligned}
g_x = & G \rho \sum_{i=1}^2 \sum_{j=1}^2 \sum_{k=1}^2 (-1)^{i+j+k} \times \left[ Y_j \ln \left| \frac{Z_k + r_{ijk}}{\sqrt{X_i^2 + Y_j^2}} \right| + Z_k \ln \left| \frac{Y_j + r_{ijk}}{\sqrt{X_i^2 + Z_k^2}} \right| \right. \\
& \left. - X_i \tan^{-1} \frac{Y_j Z_k}{X_i r_{ijk}} \right]; \quad (3.13)
\end{aligned}$$

$$g_y = G\rho \sum_{i=1}^2 \sum_{j=1}^2 \sum_{k=1}^2 (-1)^{i+j+k} \times \left[ Z_k \ln \left| \frac{X_i + r_{ijk}}{\sqrt{Y_j^2 + Z_k^2}} \right| + X_i \ln \left| \frac{Z_k + r_{ijk}}{\sqrt{X_i^2 + Y_j^2}} \right| - Y_j \tan^{-1} \frac{X_i Z_k}{Y_j r_{ijk}} \right]. \quad (3.14)$$

### 3.5 Line Integral Analytical Method

It was mentioned in Chapter 2 (see Eqs. 2.9 and 2.10), that the computation of gravity disturbances require the computation of gravity attraction, while for gravity anomalies both gravity attraction and potential are pre requisite. The formula for computing gravity attraction of polyhedral body with linearly varying density have been derived by Pohánka, 1988. Therefore, following the concept used by Pohánka (1988, 1990), we derive the optimum expression for computing the gravitational potential of polyhedral body with a linearly varying density. The expression for the gravitational attraction of a polyhedral body with homogeneous density is given in Pohánka (1988). The formula for gravitational attraction of polyhedral body with linearly increasing density is given by Pohánka (1998). In comparison to the formula for the gravitational potential given by Holstein (2003), the main advantage of adopting the computational strategy developed by Pohánka (1988, 1990) is that our expressions does not have singular terms. We also demonstrate that the algorithm for computing the gravitational attraction proposed by Pohánka (1988) can directly be applied for computing the potential.

Let us consider a linearly varying density distribution (cf. Pohánka, 1998):

$$\rho(\mathbf{r}') = \rho_0 + \rho_1 \cdot \mathbf{r}', \quad (3.15)$$

where  $\rho_0$  is the value of density at a suitably chosen origin of the local coordinate system used for a description of the density model within the volume  $D$  of the polyhedral body and  $\rho_1$  is the gradient of the linear density distribution function. Combining Eqs. (2.1) and (3.15), we get

$$V(\mathbf{r}) = G (\rho_0 + \rho_1 \cdot \mathbf{r}) \iiint_D \frac{1}{|\mathbf{r}' - \mathbf{r}|} d\tau' + G \rho_1 \cdot \iiint_D \frac{\mathbf{r}' - \mathbf{r}}{|\mathbf{r}' - \mathbf{r}|} d\tau'. \quad (3.16)$$

Using the identities

$$\nabla_{\mathbf{r}'} \cdot \frac{\mathbf{r}' - \mathbf{r}}{|\mathbf{r}' - \mathbf{r}|} = \frac{2}{|\mathbf{r}' - \mathbf{r}|}, \quad \nabla_{\mathbf{r}'} |\mathbf{r}' - \mathbf{r}| = \frac{\mathbf{r}' - \mathbf{r}}{|\mathbf{r}' - \mathbf{r}|},$$

Next, we can re-write Eq. (3.16) as

$$V(\mathbf{r}) = G \frac{\rho_0 + \rho_1 \cdot \mathbf{r}}{2} \iiint_D \nabla_{\mathbf{r}'} \cdot \frac{\mathbf{r}' - \mathbf{r}}{|\mathbf{r}' - \mathbf{r}|} d\tau' + G \rho_1 \cdot \iiint_D \nabla_{\mathbf{r}'} |\mathbf{r}' - \mathbf{r}| d\tau'. \quad (3.17)$$

To convert the volume integrals on the right-hand side of Eq. (3.17) to the surface integrals, the Gauss divergence theorem is applied. If  $\mathbf{f}(\mathbf{r}')$  is a vector function with integrable gradient in the domain  $D$ , it holds:

$$\iiint_D \nabla_{\mathbf{r}'} \cdot \mathbf{f}(\mathbf{r}') d\tau' = \oiint_S \mathbf{f}(\mathbf{s}') \cdot d\boldsymbol{\sigma}',$$

where the surface element vector  $d\boldsymbol{\sigma}'$  is defined as the product of the unit normal vector  $\mathbf{n}(\mathbf{s}')$  oriented outwards from the volume  $D$  and the scalar surface element  $d\sigma'$  at the point  $\mathbf{s}'$  on the surface  $S$ , i.e.  $d\boldsymbol{\sigma}' = \mathbf{n}(\mathbf{s}') d\sigma'$ . Correspondingly, if  $f(\mathbf{r}')$  is a scalar function with integrable gradient in the domain, the Gauss divergence theorem holds

$$\iiint_D \nabla_{\mathbf{r}'} f(\mathbf{r}') d\tau' = \oiint_S f(\mathbf{s}') d\sigma'.$$

The application of the Gauss divergence theorem to Eq. (3.17) yields:

$$V(\mathbf{r}) = G \frac{\rho_0 + \rho_1 \cdot \mathbf{r}}{2} \oiint_S \frac{\mathbf{s}' - \mathbf{r}}{|\mathbf{s}' - \mathbf{r}|} \cdot d\boldsymbol{\sigma}' + G \rho_1 \cdot \oiint_S |\mathbf{s}' - \mathbf{r}| d\sigma', \quad (3.18)$$

where  $|\mathbf{s}' - \mathbf{r}|$  is the Euclidean distance between the computation point  $\mathbf{r}$  and the running integration point  $\mathbf{s}'$  on the surface  $S$ .

We further define the surface integrals on the right-hand side of Eq. (3.18) as a sum of the surface integrals over the polyhedral faces  $\{S_k : k = 1, 2, \dots, K\}$ , where  $K$  is the total number of the faces. At any surface point  $\mathbf{s}'$  of the  $k$ -th polyhedral face  $S_k$  we

have  $d\sigma' = \mathbf{n}_k d\sigma'$ , where  $\mathbf{n}_k$  is the unit normal vector oriented outwards from the polyhedral face  $S_k$ . Hence,

$$\begin{aligned} V(\mathbf{r}) &= G \frac{\rho_0 + \rho_1 \cdot \mathbf{r}}{2} \sum_{k=1}^K \iint_{S_k} \frac{\mathbf{s}' - \mathbf{r}}{|\mathbf{s}' - \mathbf{r}|} \cdot \mathbf{n}_k d\sigma' + G \sum_{k=1}^K \rho_1 \cdot \iint_{S_k} \mathbf{n}_k |\mathbf{s}' - \mathbf{r}| d\sigma' \\ &= G \sum_{k=1}^K \left[ \frac{\rho_0 + \rho_1 \cdot \mathbf{r}}{2} \mathbf{n}_k \cdot \iint_{S_k} \frac{\mathbf{s}' - \mathbf{r}}{|\mathbf{s}' - \mathbf{r}|} d\sigma' + \rho_1 \cdot \mathbf{n}_k \iint_{S_k} |\mathbf{s}' - \mathbf{r}| d\sigma' \right], \end{aligned} \quad (3.19)$$

In accordance with (Pohánka, 1998), we denote

$$\mathbf{G}_k(\mathbf{r}) = \iint_{S_k} \frac{\mathbf{s}' - \mathbf{r}}{|\mathbf{s}' - \mathbf{r}|} d\sigma' \quad (3.20)$$

and

$$H_k(\mathbf{r}) = \iint_{S_k} |\mathbf{s}' - \mathbf{r}| d\sigma'. \quad (3.21)$$

The gravitational potential in Eq. (3.19) then takes the following form

$$V(\mathbf{r}) = G \sum_{k=1}^K \left[ \frac{\rho_0 + \rho_1 \cdot \mathbf{r}}{2} \mathbf{n}_k \cdot \mathbf{G}_k(\mathbf{r}) + \rho_1 \cdot \mathbf{n}_k H_k(\mathbf{r}) \right]. \quad (3.22)$$

The analytical solution of the surface integral in the vector function  $\mathbf{G}_k(\mathbf{r})$  (Eq. 3.20) was derived by Pohánka (1998). We use a similar procedure for finding a closed analytical solution of the surface integral in the scalar function  $H_k(\mathbf{r})$ . Firstly, we apply the Gauss divergence theorem for converting the surface integral to a sum of line integrals along the closed polygon which forms the boundary of the polyhedral face  $S_k$ . If  $\mathbf{h}_k(\mathbf{s}')$  is a vector function with integrable gradient in the domain  $S_k$ , and  $\mathbf{n}_k \cdot \mathbf{h}_k(\mathbf{s}') = 0$  (i.e. the vector  $\mathbf{h}_k(\mathbf{s}')$  lies in the plane of the polyhedral face  $S_k$ ), it holds

$$\iint_{S_k} \nabla_{\mathbf{s}'} \cdot \mathbf{h}(\mathbf{s}') d\tau' = \oint_{L_k} \mathbf{h}(\mathbf{l}') \cdot d\boldsymbol{\xi}', \quad (3.23)$$

where the line element vector  $d\xi'$  at the point  $l'$  on the curve  $L_k$  is orthogonal to the curve  $L_k$  and to the vector  $\mathbf{n}_k$ , and oriented outwards from the face  $S_k$ . To convert the surface integral in Eq. (3.21) to a sum of line integrals, we have to find a vector function  $\mathbf{h}(s')$  in the domain  $S_k$  which satisfies the following two conditions:

$$\nabla_{s'} \cdot \mathbf{h}(s') = |s' - r| \quad (3.24)$$

and

$$\mathbf{n}_k \cdot \mathbf{h}_k(s') = 0. \quad (3.25)$$

For this purpose, we decompose the vector  $s' - r$  into two sub-components; the first component  $(s' - r)_{\parallel}$  is parallel to the polyhedral face  $S_k$ , and the second component  $(s' - r)_{\perp}$  is perpendicular it, i.e.,

$$(s' - r)_{\perp} = Z_k \mathbf{n}_k, \quad Z_k = \mathbf{n}_k \cdot (s' - r), \quad (3.26)$$

$$(s' - r)_{\parallel} = s' - r - (s' - r)_{\perp} = s' - r - \mathbf{n}_k \mathbf{n}_k \cdot (s' - r). \quad (3.27)$$

It follows from the second condition (cf. Eq. (3.25)) that the vector  $\mathbf{h}(s')$  must lie in the plane of the polyhedral face  $S_k$ . Therefore, we can write

$$\mathbf{h}_k(s') = (s' - r)_{\parallel} g(\rho_k, z_k), \quad (3.28)$$

where  $g(\rho_k, z_k)$  is a scalar function to be found in order to satisfy the first condition given in Eq. (3.24). The parameters  $\rho_k$  and  $z_k$  read:

$$\rho_k = |(s' - r)_{\parallel}|, \quad z_k = |Z_k|.$$

The substitution of Eq. (3.28) into Eq. (3.24) yields:

$$\nabla_{s'} \cdot [(s' - r)_{\parallel} g(\rho_k, z_k)] = |s' - r| \quad (3.29)$$

or

$$g(\rho_k, z_k) \nabla_{s'} \cdot (s' - r)_{||} + (s' - r)_{||} \cdot \nabla_{s'} g(\rho_k, z_k) = |s' - r|. \quad (3.30)$$

Since  $\nabla_{s'} \cdot (s' - r)_{||} = 2$ , Eq. (3.30) becomes:

$$2g(\rho_k, z_k) + (s' - r)_{||} \cdot \nabla_{s'} g(\rho_k, z_k) = |s' - r|, \quad (3.31)$$

where  $(s' - r)_{||} \cdot \nabla_{s'} = \rho_k \frac{\partial}{\partial \rho_k}$  (cf. Pohánka, 1998).

Realising that  $(s' - r) = (s' - r)_{||} + (s' - r)_{\perp} = (s' - r)_{||} + Z_k \mathbf{n}_k$ , we re-write the right-hand side of Eq. (3.31) as follows:

$$|s' - r| = \sqrt{|(s' - r)_{||}|^2 + |Z_k|^2} = \sqrt{\rho_k^2 + z_k^2}. \quad (3.32)$$

From Eq. (3.31) and Eq. (3.32), we get

$$\frac{1}{\rho_k} \frac{\partial}{\partial \rho_k} [\rho_k^2 g(\rho_k, z_k)] = \sqrt{\rho_k^2 + z_k^2}. \quad (3.33)$$

The general solution of Eq. (3.33) is found to be

$$g(\rho_k, z_k) = \frac{1}{3\rho_k^2} \left[ (\rho_k^2 + z_k^2)^{\frac{3}{2}} + c \right], \quad (3.34)$$

where  $c$  is an arbitrary integration constant. However, in order to have the function  $h_k(s')$  which satisfies the condition of the applicability of the Gauss divergence theorem (that the function  $h(s')$  has the integrable gradient in the whole domain  $S_k$ ), we have to treat the singularity when  $\rho_k \rightarrow 0$ . The condition  $\lim_{\rho_k \rightarrow 0} g(\rho_k, z_k) = 0$  is met only if  $c = -z_k^3$ . The expression in Eq. (3.34) then becomes

$$g(\rho_k, z_k) = \frac{1}{3\rho_k^2} \left[ (\rho_k^2 + z_k^2)^{\frac{3}{2}} - z_k^3 \right]. \quad (3.35)$$

The right-hand side of Eq. (3.35) is finally rearranged as follows

$$g(\rho_k, z_k) = \frac{1}{3} \left[ \sqrt{\rho_k^2 + z_k^2} + \frac{z_k^2}{\sqrt{\rho_k^2 + z_k^2 + z_k}} \right]. \quad (3.36)$$

Substituting Eq. (3.36) to Eq. (3.28), we get

$$h(s') = \frac{(s' - r)_{||}}{3} \left( \sqrt{\rho_k^2 + z_k^2} + \frac{z_k^2}{\sqrt{\rho_k^2 + z_k^2} + z_k} \right). \quad (3.37)$$

Consequently, the substitution of Eqs. (3.26), (3.27) and Eq. (3.32) to Eq. (3.37) yields

$$h(s') = \frac{s' - r - \mathbf{n}_k \mathbf{n}_k \cdot (s' - r)}{3} \left[ |(s' - r)| + \frac{|\mathbf{n}_k \cdot (s' - r)|^2}{|(s' - r)| + |\mathbf{n}_k \cdot (s' - r)|} \right]. \quad (3.38)$$

From Eqs. (3.21) and (3.23), the function  $H_k(\mathbf{r})$  becomes

$$H_k(\mathbf{r}) = \oint_{L_k} h(l') \cdot d\xi'. \quad (3.39)$$

Finally, the substitution of Eq. (3.38) into Eq. (3.39) yields:

$$H_k(\mathbf{r}) = \oint_{L_k} \frac{l' - r - \mathbf{n}_k \mathbf{n}_k \cdot (l' - r)}{3} \left[ |(l' - r)| + \frac{|\mathbf{n}_k \cdot (l' - r)|^2}{|(l' - r)| + |\mathbf{n}_k \cdot (l' - r)|} \right] \cdot d\xi', \quad (3.40)$$

where  $|(l' - r)|$  is the Euclidean distance between the computation point  $\mathbf{r}$  and the running integration point  $l$  on the polygon  $L_k$ . Since the vector  $d\xi'$  is perpendicular to the vector  $\mathbf{n}_k$ , i.e.  $\mathbf{n}_k \cdot d\xi' = 0$ , we write

$$H_k(\mathbf{r}) = \oint_{L_k} \frac{l' - r}{3} \left[ |(l' - r)| + \frac{|\mathbf{n}_k \cdot (l' - r)|^2}{|(l' - r)| + |\mathbf{n}_k \cdot (l' - r)|} \right] \cdot d\xi'. \quad (3.41)$$

By analogy with the notation used in Pohánka (1988), the polygon segments  $\{L_{k,l} : l = 1, 2, \dots, L(k)\}$  form the closed polygon  $L_k$  of the polyhedral face  $S_k$ ;  $L(k)$  is the total number of polygon segments  $L_{k,l}$  of the polyhedral face  $S_k$ . We further denote the position vectors  $\mathbf{a}_{k,l}$  and  $\mathbf{a}_{k,l+1}$  of the end points of the polygon segment  $L_{k,l}$  (note that the vertices of the polyhedral face  $S_k$  are numbered counter-clockwise as viewed from outside, and  $\mathbf{a}_{k,L(k)+1} = \mathbf{a}_{k,1}$ ). For every polygon segment  $L_k$  we define the unit vectors  $\boldsymbol{\mu}_{k,l}$  and  $\boldsymbol{\nu}_{k,l}$ . The unit vector  $\boldsymbol{\mu}_{k,l}$  is parallel to the polygon segment  $L_{k,l}$  and has the same orientation. It reads

$$\boldsymbol{\mu}_{k,l} = \frac{\mathbf{a}_{k,l+1} - \mathbf{a}_{k,l}}{d_{k,l}}, \quad (3.42)$$

where  $d_{k,l}$  is the length of the segment  $L_{k,l}$  i.e.

$$d_{k,l} = \left| \mathbf{a}_{k,l+1} - \mathbf{a}_{k,l} \right|. \quad (3.43)$$

The unit vector  $\boldsymbol{\nu}_{k,l}$  is perpendicular to the polygon segment  $L_k$  and lies in the plane of the polyhedral face  $S_k$ . It reads:

$$\boldsymbol{\nu}_{k,l} = \boldsymbol{\mu}_{k,l} \times \mathbf{n}_k. \quad (3.44)$$

We define the position vector  $\mathbf{l}'$  of a point on the polygon segment  $L_{k,l}$  as a function of the unit vector  $\boldsymbol{\mu}_{k,l}$  in the following form:

$$\mathbf{l}' = \mathbf{a}_{k,l} + \boldsymbol{\mu}_{k,l} \xi' \quad (0 \leq \xi' \leq d_{k,l}). \quad (3.45)$$

Similarly, we define the line element vector  $d\xi'$  as vector parallel to the unit vector  $\boldsymbol{\nu}_{k,l}$ :

$$d\xi' = \boldsymbol{\nu}_{k,l} d\xi', \quad (3.46)$$

where  $d\xi'$  is the scalar line element of the polygon segment  $L_{k,l}$ .

Since  $\mathbf{n}_k \cdot \boldsymbol{\mu}_{k,l} = 0$ , the quantity  $\mathbf{n}_k \cdot (\mathbf{l}' - \mathbf{r}) = \mathbf{n}_k \cdot (\mathbf{a}_{k,l} - \mathbf{r})$  in Eq. (3.41) is the perpendicular distance between the computation point and the polyhedron face  $k$ . It neither depends on  $\xi'$  nor on the index  $l$ . Let us denote this quantity equal to  $z_k(\mathbf{r}) = |\mathbf{Z}_k(\mathbf{r})|$

$$z_k(\mathbf{r}) = |\mathbf{n}_k \cdot (\mathbf{l}' - \mathbf{r})| = |\mathbf{n}_k \cdot (\mathbf{a}_{k,1} - \mathbf{r})|. \quad (3.47)$$

The line integral in Eq. (3.41) then takes the following form

$$H_k(\mathbf{r}) = \oint_{L_k} \frac{\mathbf{l}' - \mathbf{r}}{3} \left[ |\mathbf{l}' - \mathbf{r}| + \frac{z_k^2}{|\mathbf{l}' - \mathbf{r}| + z_k} \right] \cdot d\xi'. \quad (3.48)$$



The polygon  $L_k$  in Eq. (3.48) is further rewritten as a sum of the polygon segments  $L_{k,l}$ . After substituting Eqs. (3.45) and (3.46) to Eq. (3.48), we have

$$H_k(\mathbf{r}) = \sum_{l=1}^{L(k)} \int_0^{d_{k,l}} \frac{\boldsymbol{\nu}_{k,l} \cdot (\mathbf{a}_{k,l} - \mathbf{r} + \boldsymbol{\mu}_{k,l} \xi')}{3} \left[ |\mathbf{a}_{k,l} - \mathbf{r} + \boldsymbol{\mu}_{k,l} \xi'| + \frac{z_k^2(\mathbf{r})}{|\mathbf{a}_{k,l} - \mathbf{r} + \boldsymbol{\mu}_{k,l} \xi'| + z_k(\mathbf{r})} \right] d\xi'.$$

Since  $\boldsymbol{\nu}_{kl} \cdot \boldsymbol{\mu}_{kl} = 0$ , we arrive at

$$H_k(\mathbf{r}) = \sum_{l=1}^{L(k)} \int_0^{d_{k,l}} \frac{\boldsymbol{\nu}_{k,l} \cdot (\mathbf{a}_{k,l} - \mathbf{r})}{3} \left[ |\mathbf{a}_{k,l} - \mathbf{r} + \boldsymbol{\mu}_{k,l} \xi'| + \frac{z_k^2(\mathbf{r})}{|\mathbf{a}_{k,l} - \mathbf{r} + \boldsymbol{\mu}_{k,l} \xi'| + z_k(\mathbf{r})} \right] d\xi'. \quad (3.49)$$

We decompose the vector  $\mathbf{a}_{k,l} - \mathbf{r}$  in Eq. (3.49) into the vector components  $\boldsymbol{\mu}_{k,l}$ ,  $\boldsymbol{\nu}_{k,l}$  and  $\mathbf{n}_k$ , and adopt the following notation (cf. Pohánka, 1998, Eqs. 28 and 29):

$$\begin{aligned} \boldsymbol{\mu}_{k,l}(\mathbf{r}) &= \boldsymbol{\mu}_{k,l} \cdot (\mathbf{a}_{k,l} - \mathbf{r}) \\ w_{k,l}(\mathbf{r}) &= \boldsymbol{\nu}_{k,l} \cdot (\mathbf{a}_{k,l} - \mathbf{r}) \\ Z_k(\mathbf{r}) &= \mathbf{n}_k \cdot (\mathbf{a}_{k,l} - \mathbf{r}) \end{aligned} \quad (3.50)$$

From Eqs. (3.45) and (3.50), we write:

$$|\mathbf{l}' - \mathbf{r}| = |\mathbf{a}_{k,l} - \mathbf{r} + \boldsymbol{\mu}_{k,l} \xi'| = \sqrt{(\boldsymbol{\mu}_{k,l}(\mathbf{r}) + \xi')^2 + w_{k,l}^2(\mathbf{r}) + z_k^2(\mathbf{r})}. \quad (3.51)$$

The substitution of Eqs. (3.50) and (3.51) into Eq. (3.49) yields:

$$\begin{aligned} H_k(\mathbf{r}) &= \sum_{l=1}^{L(k)} \int_0^{d_{k,l}} \frac{w_{k,l}(\mathbf{r})}{3} \left[ \sqrt{(\boldsymbol{\mu}_{k,l}(\mathbf{r}) + \xi')^2 + w_{k,l}^2(\mathbf{r}) + z_k^2(\mathbf{r})} \right. \\ &\quad \left. + \frac{z_k^2(\mathbf{r})}{\sqrt{(\boldsymbol{\mu}_{k,l}(\mathbf{r}) + \xi')^2 + w_{k,l}^2(\mathbf{r}) + z_k^2(\mathbf{r})} + z_k(\mathbf{r})} \right] d\xi'. \end{aligned}$$

Furthermore, after applying the substitution  $\mu_{k,l} + \xi' = \xi$ , we get:

$$H_k(\mathbf{r}) = \sum_{l=1}^{L(k)} \int_{\mu_{k,l}}^{\nu_{k,l}} \frac{w_{k,l}(\mathbf{r})}{3} \left[ \sqrt{\xi^2 + w_{k,l}^2(\mathbf{r}) + z_k^2(\mathbf{r})} + \frac{z_k^2(\mathbf{r})}{\sqrt{\xi^2 + w_{k,l}^2(\mathbf{r}) + z_k^2(\mathbf{r})} + z_k(\mathbf{r})} \right] d\xi, \quad (3.52)$$

where

$$\nu_{k,l} = \mu_{k,l} + d_{k,l}. \quad (3.53)$$

Denoting

$$\Phi(\mu, \nu, w, z) = \int_{\mu}^{\nu} \frac{w}{\sqrt{\xi^2 + w^2 + z^2} + z} d\xi \quad (3.54)$$

and

$$\Phi_3(\mu, \nu, w, z) = \int_{\mu}^{\nu} w \sqrt{\xi^2 + w^2 + z^2} d\xi, \quad (3.55)$$

we finally arrive at

$$H_k(\mathbf{r}) = \frac{1}{3} \sum_{l=1}^{L(k)} \left[ z_k^2(\mathbf{r}) \Phi(\mu_{k,l}(\mathbf{r}), \nu_{k,l}(\mathbf{r}), w_{k,l}(\mathbf{r}), z_k(\mathbf{r})) + \Phi_3(\mu_{k,l}(\mathbf{r}), \nu_{k,l}(\mathbf{r}), w_{k,l}(\mathbf{r}), z_k(\mathbf{r})) \right]. \quad (3.56)$$

The closed analytical expression for  $\Phi$  reads ([Pohánka, 1988, 1998](#)):

$$\Phi(\mu, \nu, w, z) = w L(\mu, \nu, w, z) + 2z A(\mu, \nu, w, z), \quad (3.57)$$

where

$$L(\mu, \nu, w, z) = \ln \frac{\sqrt{\nu^2 + w^2 + z^2} + \nu}{\sqrt{\mu^2 + w^2 + z^2} + \mu} \quad (3.58)$$

and

$$A(\mu, \nu, w, z) = -\arctan \frac{2w(\nu - \mu)}{T^2(\mu, \nu, w, z) - (\nu - \mu)^2 + 2zT(\mu, \nu, w, z)}. \quad (3.59)$$

By integrating the right-hand side of Eq. (3.55), we get

$$\Phi_3(\mu, \nu, w, z) = \frac{w}{4}(\nu - \mu) \left[ \frac{(\nu + \mu)^2}{T(\mu, \nu, w, z)} + T(\mu, \nu, w, z) \right] + \frac{w}{2}(w^2 + z^2)L(\mu, \nu, w, z), \quad (3.60)$$

where

$$T(\mu, \nu, w, z) = \sqrt{\mu^2 + w^2 + z^2} + \sqrt{\nu^2 + w^2 + z^2}. \quad (3.61)$$

The expression for numerical calculation of the vector function  $G(\mathbf{r})$  in Eq. (3.22) was derived by (Pohánka, 1998, Eqs. (33), (34) and (35)) in the following form:

$$\begin{aligned} \mathbf{G}_k(\mathbf{r}) = & \sum_{l=1}^{L(k)} \left[ \Phi_2(\mu_{k,l}(\mathbf{r}), \nu_{k,l}(\mathbf{r}), w_{k,l}(\mathbf{r}), \mathbf{Z}_k(\mathbf{r})) \boldsymbol{\nu}_{k,l} \right. \\ & \left. + \mathbf{Z}_k(\mathbf{r}) \Phi(\mu_{k,l}(\mathbf{r}), \nu_{k,l}(\mathbf{r}), w_{k,l}(\mathbf{r}), \mathbf{Z}_k(\mathbf{r})) \mathbf{n}_k \right], \end{aligned} \quad (3.62)$$

where the expression for  $\Phi_2$  reads:

$$\begin{aligned} \Phi_2(\mu_{k,l}(\mathbf{r}), \nu_{k,l}(\mathbf{r}), w_{k,l}(\mathbf{r}), \mathbf{Z}_k(\mathbf{r})) = & \frac{1}{4}(\nu - \mu) \left[ \frac{(\nu + \mu)^2}{T(\mu, \nu, w, z)} + T(\mu, \nu, w, z) \right] + \\ & + \frac{1}{2}(w^2 + z^2)L(\mu, \nu, w, z). \end{aligned} \quad (3.63)$$

Comparing the expressions for  $\Phi_3$  and  $\Phi_2$  in Eqs. (3.60) and (3.63), the following relation between them is obtained

$$\Phi_3(\mu, \nu, w, z) = w \Phi_2(\mu, \nu, w, z). \quad (3.64)$$

Utilising Eq. (3.64), the expression for the scalar function  $H_k(\mathbf{r})$  in Eq. (3.56) becomes

$$H_k(\mathbf{r}) = \frac{1}{3} \sum_{l=1}^{L(k)} \left[ z_k^2 \Phi(\mu_{k,l}(\mathbf{r}), \nu_{k,l}(\mathbf{r}), w_{k,l}(\mathbf{r}), z_k(\mathbf{r})) + w_{k,l}(\mathbf{r}) \Phi_2(\mu_{k,l}(\mathbf{r}), \nu_{k,l}(\mathbf{r}), w_{k,l}(\mathbf{r}), Z_k(\mathbf{r})) \right]. \quad (3.65)$$

The vectors  $\mu_{k,l}$  and  $\nu_{k,l}$  are perpendicular to  $\mathbf{n}_k$ , i.e.  $\mathbf{n}_k \cdot \mu_{k,l} = 0$  and  $\mathbf{n}_k \cdot \nu_{k,l} = 0$ . From Eq. (3.63), it also follows that

$$\Phi_2(\mu_{k,l}(\mathbf{r}), \nu_{k,l}(\mathbf{r}), w_{k,l}(\mathbf{r}), Z_k(\mathbf{r})) = \Phi_2(\mu_{k,l}(\mathbf{r}), \nu_{k,l}(\mathbf{r}), w_{k,l}(\mathbf{r}), z_k(\mathbf{r})).$$

The substitution of the functions  $G_k(\mathbf{r})$  and  $H_k(\mathbf{r})$  from Eqs. (3.62) and (3.65) to Eq. (3.22) then yields

$$\begin{aligned} V(\mathbf{r}) = & G \sum_{k=1}^K \left[ \sum_{l=1}^{L(k)} \left( \frac{\rho_0 + \rho_1 \cdot \mathbf{r}}{2} Z_k(\mathbf{r}) + \rho_1 \cdot \mathbf{n}_k z_k^2(\mathbf{r}) \right) \Phi(\mu_{k,l}(\mathbf{r}), \nu_{k,l}(\mathbf{r}), w_{k,l}(\mathbf{r}), z_k(\mathbf{r})) \right. \\ & \left. + \sum_{l=1}^{L(k)} \frac{\rho_1 \cdot \mathbf{n}_k}{3} w_{k,l} \Phi_2(\mu_{k,l}(\mathbf{r}), \nu_{k,l}(\mathbf{r}), w_{k,l}(\mathbf{r}), z_k(\mathbf{r})) \right]. \quad (3.66) \end{aligned}$$

As seen from (3.22), only those components of the function  $G_k(\mathbf{r})$  contribute to the potential which are parallel to the surface normal (i.e. the components along the unit normal vector  $\mathbf{n}_k$ ).

The expression for the potential in Eq. (3.66) has very close resemblances with the formula for the attraction derived by (Pohánka, 1998, Eq. 52). To obtain the final form of (3.66), we follow the same way as Pohánka proposed. We introduce a small positive number  $\epsilon$  in order to avoid any undefined operations when the computation point is near the surface of the polyhedral body ( cf. Pohánka, 1988, 1998). The functions  $\Phi(\mu, \nu, w, z)$  and  $\Phi_2(\mu, \nu, w, z)$  are replaced by the functions  $\Phi(\mu, \nu, w, z, \epsilon)$  and  $\Phi_2(\mu, \nu, w, z, \epsilon)$ , respectively:

$$\begin{aligned} V(\mathbf{r}) = & G \sum_{k=1}^K \sum_{l=1}^{L(k)} \left[ \left( \frac{\rho_0 + \rho_1 \cdot \mathbf{r}}{2} Z_k(\mathbf{r}) + \rho_1 \cdot \mathbf{n}_k z_k^2(\mathbf{r}) \right) \Phi(\mu_{k,l}(\mathbf{r}), \nu_{k,l}(\mathbf{r}), w_{k,l}(\mathbf{r}), z_k(\mathbf{r}), \epsilon) \right. \\ & \left. + \sum_{l=1}^{L(k)} \frac{\rho_1 \cdot \mathbf{n}_k}{3} w_{k,l} \Phi_2(\mu_{k,l}(\mathbf{r}), \nu_{k,l}(\mathbf{r}), w_{k,l}(\mathbf{r}), z_k(\mathbf{r}), \epsilon) \right], \quad (3.67) \end{aligned}$$

where

$$\Phi(\mu, \nu, w, z, \epsilon) = wL(\mu, \nu, w, z + \epsilon) + 2zA(\mu, \nu, w, z + \epsilon), \quad (3.68)$$

and

$$\Phi_2(\mu, \nu, w, z, \epsilon) = \frac{1}{4}(\nu - \mu) \left[ \frac{(\nu + \mu)^2}{T(\mu, \nu, w, z + \epsilon)} + T(\mu, \nu, w, z + \epsilon) \right] + \frac{1}{2}(w^2 + z^2)L(\mu, \nu, w, z + \epsilon). \quad (3.69)$$

Eq. (3.67) represents the potential of an arbitrary polyhedral body with a linearly varying density distribution. Setting  $\rho_1 = 0$  in Eq. (3.67) gives the expression for the potential generated by a homogeneous polyhedral body:

$$V(\mathbf{r}) = \frac{G\rho_0}{2} \sum_{k=1}^K \sum_{l=1}^{L(k)} Z_k(\mathbf{r}) \Phi(\mu_{k,l}(\mathbf{r}), \nu_{k,l}(\mathbf{r}), w_{k,l}(\mathbf{r}), z_k(\mathbf{r}), \epsilon). \quad (3.70)$$

The gravitation attraction vector for the polyhedral body with linearly varying density reads (Pohánka, 1998, Eq. (58)):

$$\begin{aligned} \mathbf{g}(\mathbf{r}) = & -G \sum_{k=1}^K \sum_{l=1}^{L(k)} \left[ \left( (\rho_0 + \rho_1 \cdot \mathbf{r} + \rho_1 \cdot \mathbf{n}_k Z_k(\mathbf{r})) \Phi(\mu_{k,l}(\mathbf{r}), \nu_{k,l}(\mathbf{r}), w_{k,l}(\mathbf{r}), z_k(\mathbf{r}), \epsilon) \right. \right. \\ & + \left. \left. \rho_1 \cdot \nu_k \Phi_2(\mu_{k,l}(\mathbf{r}), \nu_{k,l}(\mathbf{r}), w_{k,l}(\mathbf{r}), z_k(\mathbf{r}), \epsilon) \right) \mathbf{n}_k \right. \\ & \left. - \frac{1}{2} Z_k(\mathbf{r}) \Phi(\mu_{k,l}(\mathbf{r}), \nu_{k,l}(\mathbf{r}), w_{k,l}(\mathbf{r}), z_k(\mathbf{r}), \epsilon) \rho_1 \right], \quad (3.71) \end{aligned}$$

Setting  $\rho_1 = 0$  in Eq. (3.71), gives the expression for the gravitational attraction vector generated by a homogeneous polyhedral body:

$$\mathbf{g}(\mathbf{r}) = -G \rho_0 \sum_{k=1}^K \mathbf{n}_k \sum_{l=1}^{L(k)} \Phi(\mu_{k,l}(\mathbf{r}), \nu_{k,l}(\mathbf{r}), w_{k,l}(\mathbf{r}), z_k(\mathbf{r}), \epsilon). \quad (3.72)$$

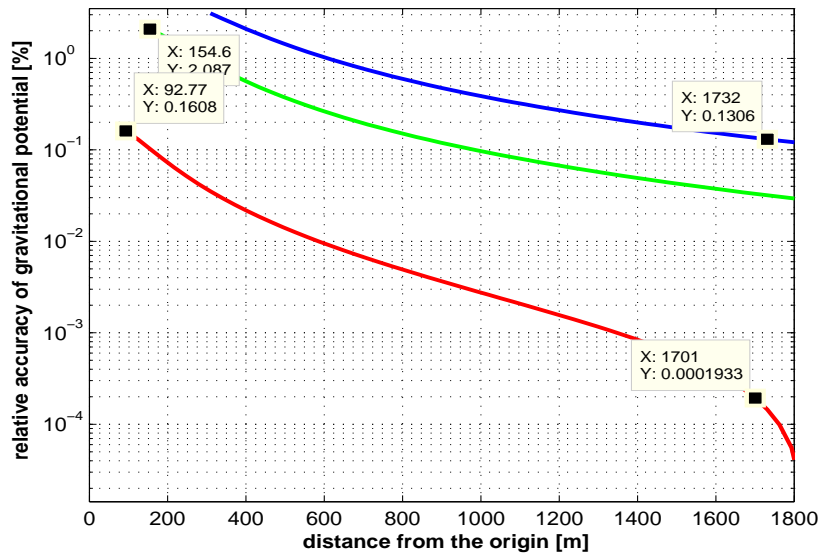
We have derived by means of line integrals the analytical formula for the gravitational potential of an arbitrary polyhedral body having a linearly varying density. The corresponding analytical formula for the components of the gravitational attraction vector was given by Pohánka (1998). As seen from Eq. (3.22), the derivation of the expression for gravitational potential was reduced to finding only the closed

analytical solution for the surface integral in the scalar function  $H_k(\mathbf{r})$ , while the solution for the surface integral in the vector function  $\mathbf{G}_k(\mathbf{r})$  was already derived in Pohánka (1998). We further adopted the optimized expressions from Pohánka (1988, 1990) by reducing the number of logarithm and arctangent terms, treating the undefined operations (e.g. expressions of the type  $0/0$ ) and improving the precision of numerical operations when the computation point is far away from the polyhedral body. The expressions and uniform algorithm for computing the gravitational potential and attraction are numerically very simple and valid for any point in space and need no special care for the points near or on the surface of the polyhedral body. The designed algorithm for calculation of the gravitational potential and attraction generated by polyhedral body having a linearly varying density is given in Appendix A.

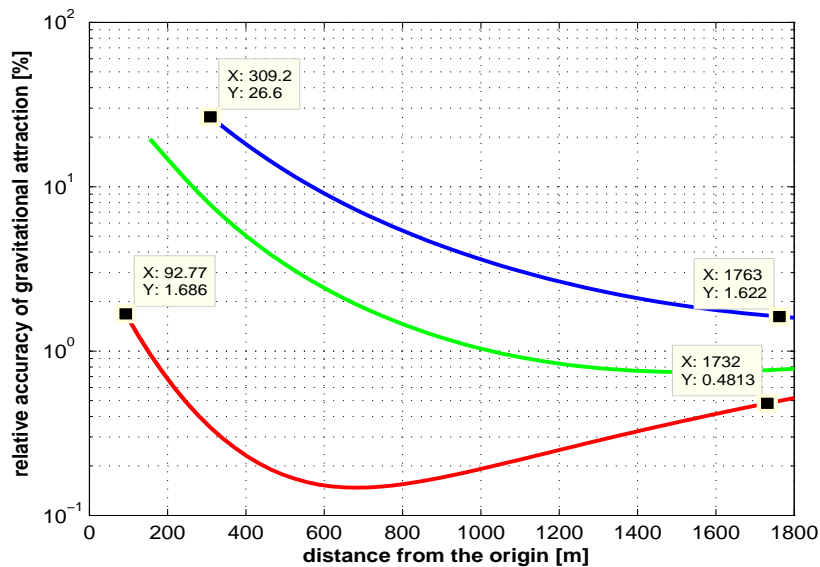
### 3.6 Test For Numerical Accuracy And Efficiency

A numerical experiment was conducted for three different sizes of rectangular prism having base areas equal to  $30 \times 30 \text{ m}^2$ ,  $150 \times 150 \text{ m}^2$ , and  $300 \times 300 \text{ m}^2$ , each prism having constant height of 100 m.. First, analytical methods were used to compute the gravitational potential and gravitational attraction. The analytical methods, namely line integral approach and rectangular prism approaches were applied. After that the linear vertical mass, the Gauss cubature and point mass approach were applied. In this experiment the computation point is taken in such a way that it start just from the vicinity of the body and span to distance of approximately 1800 m away from the body. Only the horizontal  $x$  direction of the computation point is changing. The  $y$  and  $z$ - values for the computation points is constant and represent the centre of the body. For the semi-analytical linear vertical mass approach, we have consider the spherical shell of the same dimension of above prisms. The prism methods assume a planer approximation and it give best result at the computation point near to the body, while the semi-analytical methods used spherical approximation and give best result for the far-zone computation.

The relative accuracy of the linear vertical mass, Gauss cubature, and point mass approach with respect to the analytical methods of rectangular prism approach at the vicinity of the body up to a distance of 1800 m are calculated. Figures 3.1a and

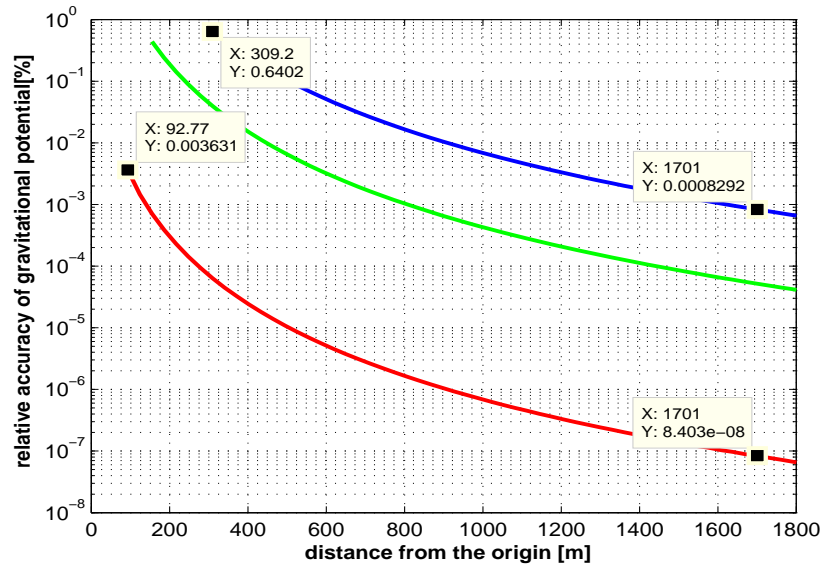


(a)

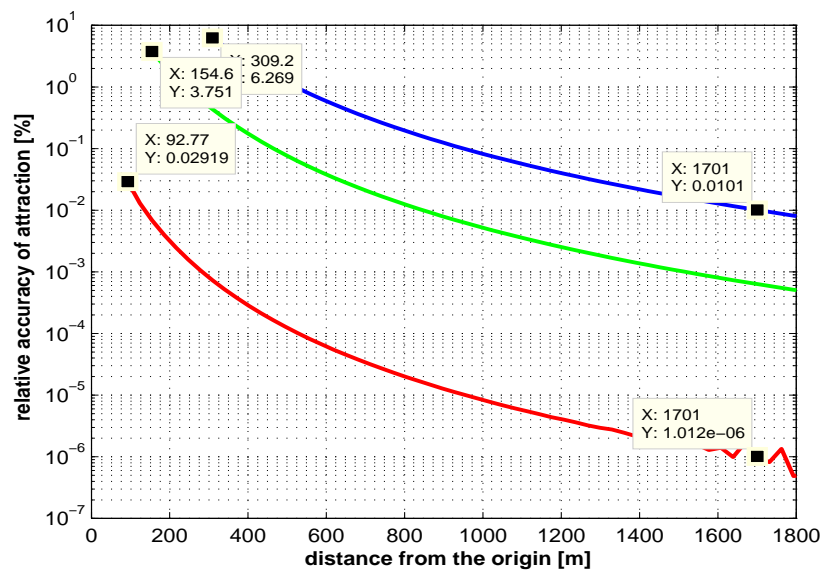


(b)

**Figure 3.1** The inaccuracy of linear vertical mass approach relative to prism method (a) gravitational potential and (b) gravitational attraction. Red, green, and blue colour represent the computation for a spherical shell of the same dimension of a prisms of the height 100 m and the base area,  $30 \times 30 \text{ m}^2$ ,  $150 \times 150 \text{ m}^2$ , and  $300 \times 300 \text{ m}^2$ , respectively.



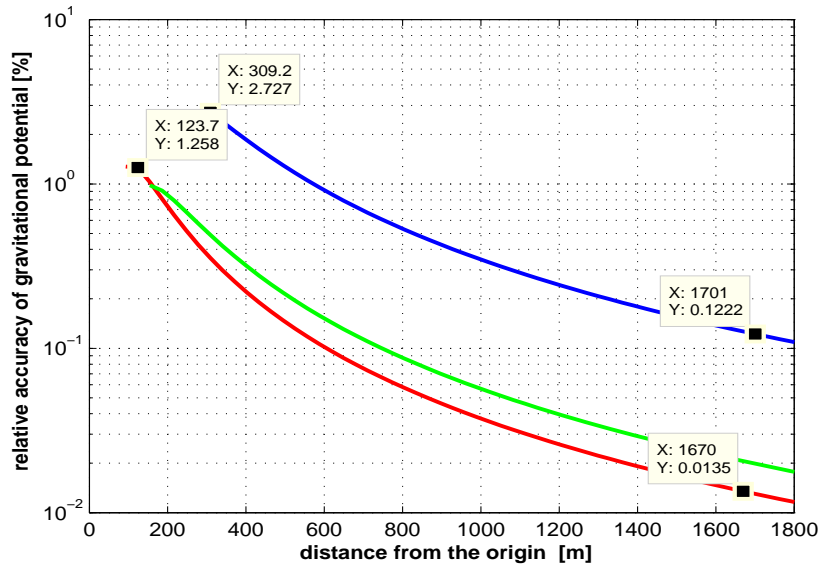
(a)



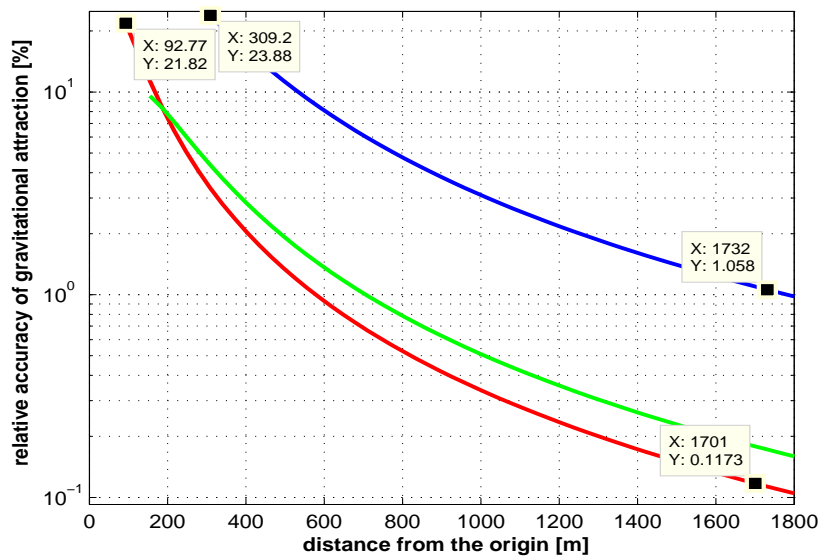
(b)

**Figure 3.2** The inaccuracy of Gauss cubature approach relative to prism method (a) gravitational potential and (b) gravitational attraction. Red, green, and blue colour represent the computation for prisms of the height 100 m and the base area, 30x30 m<sup>2</sup>, 150x150 m<sup>2</sup>, and 300x300 m<sup>2</sup>, respectively.





(a)



(b)

**Figure 3.3** The inaccuracy of the point mass approach. relative to prism method (a) gravitational potential and (b) gravitational attraction. Red, green, and blue colour represent the computation for prisms of the height 100 m and the base area,  $30 \times 30 \text{ m}^2$ ,  $150 \times 150 \text{ m}^2$ , and  $300 \times 300 \text{ m}^2$ , respectively.

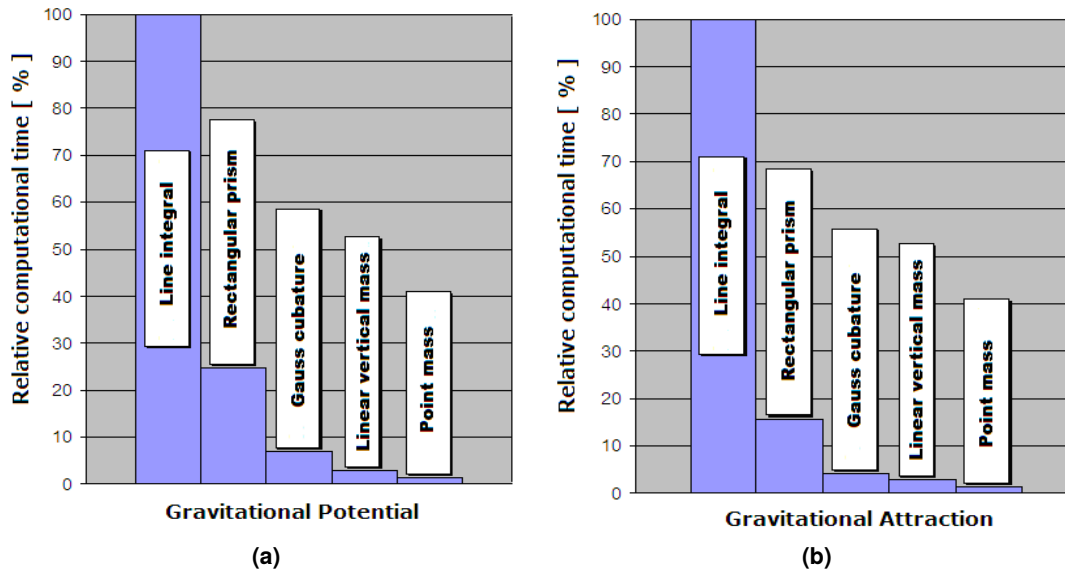


**Figure 3.4** The relative time efficiency with respect to the line integral analytical method (a) potential (b) attraction.

[3.1b](#) describes the relative precision of linear vertical mass approach with respect to analytical methods for gravitational potential and attraction, respectively. The relative accuracy of the Gauss cubature methods is shown in Figures [3.2a](#), and [3.2b](#) for gravitational potential and gravitational attraction, respectively, while the corresponding relative accuracy of the point mass approach is shown in Figures [3.3a](#) and [3.3b](#). The Gauss cubature approach is more accurate than the linear vertical mass and the point-mass approaches. The relative accuracy of computing the gravitational potential and gravitational attraction reaches to 99.9% and 99%, respectively, if the computation point is 600 m away from the centre of the body, provided that the geographical resolution of input data i.e., terrain model resolution is higher than  $300 \times 300 \text{ m}^2$  (see Figures. [3.2a](#) and [3.2b](#)). The relative precision of computing the gravitational potential better than 99% can be achieved by the linear vertical mass approach if the computation point is 600 m away from the source and the geographical resolution of input data is  $300 \times 300 \text{ m}^2$  or higher (see Figure. [3.1a](#)). The same relative accuracy of computing the gravitational attraction by the linear vertical mass approach is, however guaranteed only if  $30 \times 30 \text{ m}^2$  geographical resolution of input data is used for the linear vertical mass approach (cf. Figure [3.1b](#)). From this experiment we observed that more than 99% numerical accuracy can be archived by using the semi-analytical method, when the computation point is away at-least 6 times the size of the body (Figures [3.1a](#) and [3.1b](#)).

The comparison of the time-efficiency of the analytical (line integral/prism methods), semi-analytical (linear vertical mass) and numerical methods (Gauss cubature and point mass) applied for computing the gravitational potential and attraction is given in Figure.3.4. The time-efficiency is provided in terms of the relative computation time. The line integral approach is the most time-consuming (cf. Figure. 3.4). The rectangular prism approach is less time-consuming; it requires 25% of the total time otherwise needed for computing the potential by line integral approach, and less than 15% for computing the attraction. The time efficiency of the semi-analytical methods is similar, reducing the calculation time by an order of magnitude compared to the line integral approach. The point-mass approach is the most time-efficient. Compared with the line integral approach, it reduces the calculation time by almost two orders of magnitude.

The use of the numerical point-mass approach is inadequate when the computation point is within the source body vicinity up to 1 arc-min. It introduces large errors, especially in computing the gravitational attraction. Based on the above comparison we adopted a scheme in which the region around the computation point is divided into different zones, namely, inner zone, near-zone and far-zone. The inner zone comprises all prisms with a spherical distance not exceeding 5 km of the computation point. The near zone comprises all prisms between the inner zone and the spherical distance of 50 km from the computation point, and rest is far zone. We choose analytical methods for the inner zone and near zone and semi analytical method for the far zone computation. The most suitable method in each particular zone is applied. For near zone computation the rectangular prism method is appropriate. For the rest of the globe i.e., in the far zone linear vertical mass approach are the best option. Further detailed are given in the next chapter.

### 3.7 Summary

In this chapter different analytical, semi-analytical and numerical methods for calculating the gravitational attraction and potential were presented. Near to the computation point the use of analytical methods provides better accuracy. Away from the source body the semi-analytical linear vertical mass approach is used. The optimal and efficient expressions for computing the potential of a polyhedral body with constant or linearly varying density were derived for the first time. The relative

accuracy of these methods and their time efficiency were compared. Furthermore, the optimal choice of a particular method for gravity field calculation with in a particular zone, i.e., inner, near and far zone were discussed. In this research we have used the more accurate analytical method for the inner-zone and near-zone computation and semi-analytical methods for the far-zone computation.

---

## Global maps of the CRUST 1.0 crustal component stripped gravity field

One of the major sources of information about the Earth's structure is its gravity field. In studies of the Moho boundary geometry, the gravitational effect of the topography density, bathymetry, ice, sediments, and other crust residual density effects are modelled and are subsequently removed from the observed gravity. To that end, a technique known as “stripping” has been used. In stripping procedure, forwards modeling has been used to modeled the gravitational corrections due to residual densities and subsequently applied these corrections to the gravity data, so that to unmask the remaining gravitational signal from the source of interest. The strongest signal in gravity data is due to topographic relief onshore and ocean bottom relief offshore. Due to this signal the observed gravity data show little correlation with the Moho geometry and are relatively rough. The gravitational effects of the reference (e.g., constant average density) topographic masses onshore and sea water density contrast offshore can be removed from the gravity data by means of topographic and bathymetric stripping corrections, respectively. The next strongest signal in the gravity data is due to the ice density contrast, sedimentary layers and crustal/lithospheric density variations. A crustal/lithospheric model should be adopted or produced to compute the crustal or lithospheric stripping correction. In this latter step various approaches may be taken depending on the purpose of the study, (e.g., [Kaban et al., 1999](#), [Kaban and Schwintzer, 2001](#), [Kaban et al., 2003](#), [2004](#) for global studies and [Bielik, 1988](#), [Artemjev and Kaban, 1994](#), [West et al. \(1995\)](#), [Kaban and Schwintzer \(2001\)](#), [Zeyen et al. \(2002\)](#), [Dérerová et al. \(2006\)](#), [Braun et al. \(2007\)](#), [Tassara et al. \(2007\)](#), [Alvey et al. \(2008\)](#), [Jiménez-Munt et al.](#)

(2008); and references therein for regional investigations). For global studies the best currently available global crustal models are CRUST 2.0 (Bassin et al., 2000) and the publicly-available CRUST 1.0 (Laske et al., 2013), which is an upgrade of the early CRUST 2.0 model. For our purpose, we have used the boundaries and laterally varying densities of different layers of CRUST 1.0.

When the gravimetric inverse problem is formulated in terms of gravitational attraction, the anomalous gravity data required as input in the inversion are usually gravity disturbances (e.g., Vajda and Vaníček, 2006, Vajda et al., 2007). The normal gravity values are subtracted from the observed gravity values according to the definition of the gravity disturbance. This has two implications (Vajda and Vaníček, 2006, Vajda et al., 2008). Firstly, the surface of the reference ellipsoid (not the geoid) is the bottom interface of topographic masses globally, as well as the upper interface of all residual density defining the stripping corrections. Secondly, Earth's crust density is replaced with a reference density of  $2670 \text{ kg/m}^3$ , and is the background density distribution model against which the residual density used in stripping corrections are defined. These two conditions must be satisfied in order to keep the consistency between decomposing the real Earth's subsurface density distribution and the observed gravity disturbances (cf. Vajda and Vaníček, 2006, Vajda et al., 2008).

Our aim here is to evaluate on a global scale the gravity disturbances and anomalies corrected for the attraction of the topography (ellipsoid-referenced topographic correction), the ocean residual density effect (ellipsoid-referenced bathymetry stripping correction), ice residual density, sedimentary layer residual density and the crustal residual density (down to the Moho-discontinuity). We have used the gravity disturbances for the estimation of crust-mantle density contrast as well as for the recovery of Moho geometry, whereas the gravity anomaly have used for the crust-mantle density contrast only. We take into account the global distribution of ice, sediments, and consolidated crustal components based on the CRUST 1.0 model (crustal stripping correction). The crustal stripping correction is computed and applied in several consecutive steps: (1) the attractions of the topography and residual density (relative to the constant reference crustal density of  $2670 \text{ kg/m}^3$ ) of the bathymetry, ice, and the soft and hard sediments; and (2) the attractions of the residual density (relative to the constant reference crustal density of  $2670 \text{ kg/m}^3$ ) of the upper, middle, and lower consolidated crust according to the CRUST 1.0 model. The application of the topographic and stripping corrections of the above steps (1)

and (2) removes the topographic masses above the reference ellipsoid and transforms the volumetric domain between the ellipsoid and the Moho discontinuity globally (disregarding the heterogeneities within topography other than sediments and ice, and disregarding the crustal heterogeneities not accounted for by the CRUST 1.0 density model) into a crust with a constant density of  $2670 \text{ kg/m}^3$ . The gravity disturbances computed at the stripping stage correspond to an Earth model of no topography above the ellipsoid, constant crust down to the Moho interface, and real density below the Moho interface. The strongest signal in these gravity disturbances is due to geometry of the Moho interface. We expect that this type of gravity disturbances is best suited for refining the Moho geometry.

All the step-wise corrections are presented in detail in Section 4.1, while the gravity disturbances and gravity anomalies with the individual corrections applied are described in Section 4.2. We refer to the bathymetrically-stripped and topographically corrected gravity disturbances/anomalies as “BT gravity disturbances/anomalies”.

The gravity disturbances/anomalies are computed globally at the Earth’s surface using the spherical harmonic coefficients complete to degree 180 from the EIGEN-6C2 model (which represents roughly 100 km resolution in terms of half-wavelengths). To define the computation points, we have used the topography of CRUST 1.0 model. The topographic, bathymetry, ice, upper sediment, middle sediment, lower sediment, upper crust, middle crust and lower crust stripping corrections are computed on a  $1^\circ \times 1^\circ$  grid of the geocentric spherical coordinates. The computed corrections are applied to the gravity data.

## 4.1 Corrections to gravity disturbances and anomalies

Our aim is to evaluate and compute the gravity disturbances and gravity anomalies on a global scale, which are corrected for the effects of topography, bathymetry, ice and the crustal residual density. Assuming a global distribution of ice, sediments, and crustal components based on the CRUST 1.0 model, the total crust correction is split into several components:

1. Corrections due to the attraction of topographic masses above the reference ellipsoid, and the bathymetry residual density.

2. Corrections due to the residual density of the ice, upper, middle, and lower sediments from the CRUST 1.0 model.
3. Correction due to the residual density of the upper, middle, and lower crust from the CRUST 1.0 model.

The gravity disturbance in spherical approximation is given by

$$\delta g = -\frac{\partial T}{\partial r}, \quad (4.1)$$

and gravity anomaly is given by

$$\Delta g = -\frac{\partial T}{\partial r} - \frac{2T}{r} = \delta g - \frac{2T}{r}, \quad (4.2)$$

where  $r = R + h$ ,  $R$  is the radius of a sphere which approximates the Earth, and  $h$  is the height of computational point above the ellipsoid.

There are two types of corrections; first one is given by the first term ( $-\frac{\partial T}{\partial r}$ ) in the right hand side of Eq. (4.2), whereas, the second one is given by the second term ( $\frac{2}{r}T$ ). The first correction is termed as the Direct Correction (DC), while the second one is called the Indirect Correction (IDC). Due to the definition of gravity anomalies, the IDC is only applicable to gravity anomalies, whereas, the DC is applicable to both gravity disturbances and gravity anomalies. The mathematical expressions for the direct and secondary indirect correction are given by

$$\text{DC} = \frac{\partial}{\partial r} \delta V, \quad (4.3)$$

and

$$\text{IDC} = \frac{2\delta V}{r}, \quad (4.4)$$

respectively, where  $\delta V$  is the potential generated by residual mass density, and is given by

$$\delta V = G \iiint_{v'} \frac{\delta \rho}{l} dv',$$

where  $\delta \rho$  is the residual mass density, which is the difference between actual density of a layer of crust and reference crust density of  $2670 \text{ kg/m}^3$ ,  $v'$  is the volume of the



layer, and  $l = \sqrt{(x - x')^2 + (y - y')^2 + (z - z')^2}$  is the distance between the computation point  $p(x, y, z)$  and integration point  $q(x', y', z')$ .

Total Correction (TC) is the sum of Direct Correction and Indirect Correction, and is given by

$$\text{TC} = \frac{\partial}{\partial r} \delta V + \frac{2}{r} \delta V. \quad (4.5)$$

In the next section the description of different computational schemes for these corrections are discussed.

### 4.1.1 Topographic stripping corrections

We have used a combination of different analytical and semi-analytical methods for the computation of gravitational corrections. To get sufficient numerical accuracy and save computational time we used the combination of analytical and semi-analytical methods. In the close proximity of computational point, we have used analytical methods, while, in case of more distance from the computational point, we have used semi-analytical methods. The global ellipsoid-referenced topographic correction has been computed using the following analytical and semi-analytical computational formulae:

- (a) Analytical constant density polyhedral method given by Eq. (3.72) .
- (b) Analytical constant density rectangular prism method given by Eq. (3.12).
- (c) Semi-analytical method for constant density spherical shell given by Eq. (3.10).

For every computation point, the Earth surface is divided into an inner-zone, near-zone, and far-zone. The inner-zone comprises all prisms with a spherical distance not exceeding 5 km from the computation point. The near-zone comprises of all prisms between the inner-zone and far-zones within a spherical distance not exceeding 50 km from the computation point. The remaining globe is considered as the far-zone. The analytical homogeneous density polyhedral method given by Eq. (3.72) has been used for the computation of topographic correction in the inner-zone. The constant density prism methods given by Eqs. (3.12) and semi-analytical method for constant density spherical shell given by Eq. (3.10) are used for the computation of near and far-zone contribution, respectively. For numerical efficient computation and to avoid the singularities, we have used analytical polyhedral method for the inner-zone

**Table 4.1** Statistics of ellipsoid-referenced direct correction

Direct correction (Relative to 2670 kg/m <sup>3</sup> )	Min (mGal)	Max (mGal)	Mean (mGal)
Topography	-657	-17	-68
Bathymetry	129	705	331
Ice	2	319	21
Sediments	15	174	45
Crust	-527	-170	-289

**Table 4.2** Statistics of ellipsoid-referenced indirect correction

Indirect correction (Relative to 2670 kg/m <sup>3</sup> )	Min (mGal)	Max (mGal)	Mean (mGal)
Topography	68	262	110
Bathymetry	-898	-515	-704
Ice	-108	-9.7	-22
Sediments	-120	-60	-85
Crust	487	668	567

computation of gravity correction. For the computation in the inner zone the Global Digital Elevation Model (DEM) GTOPO30C which has a resolution of 30'' × 30'' (provided by U.S. Geological Survey (USGS)) has been used. For the computation in the near and far zone the 1' × 1' global elevation model from ETOPO1 (Amante and Eakins, 2009) has been applied. Both models GTOPO30C and ETOPO1 provide the mean elevation height at the corresponding grid cell. The average topographic density 2670 kg/m<sup>3</sup> is adopted. The ellipsoid-referenced topographic correction to the gravity disturbances varies from -657 to -17 mGal with mean of -68 mGal and standard deviation of 100 mGal (see Table 4.1). The largest topographic correction are located in the mountainous regions and the smallest over the oceanic areas and flat regions (see Figure 4.1a).

The statistics of the ellipsoid-referenced direct, secondary indirect and total corrections are given in Tables 4.1, 4.2 and 4.3, respectively. The corresponding maps of direct and indirect corrections are given in Figure 4.1a, while the total correction is presented in Figure 4.2a.

#### 4.1.2 Bathymetric stripping correction

The ellipsoid-referenced bathymetry correction, which is the removal of the attraction of the ocean water density contrast enclosed between the surfaces of the reference

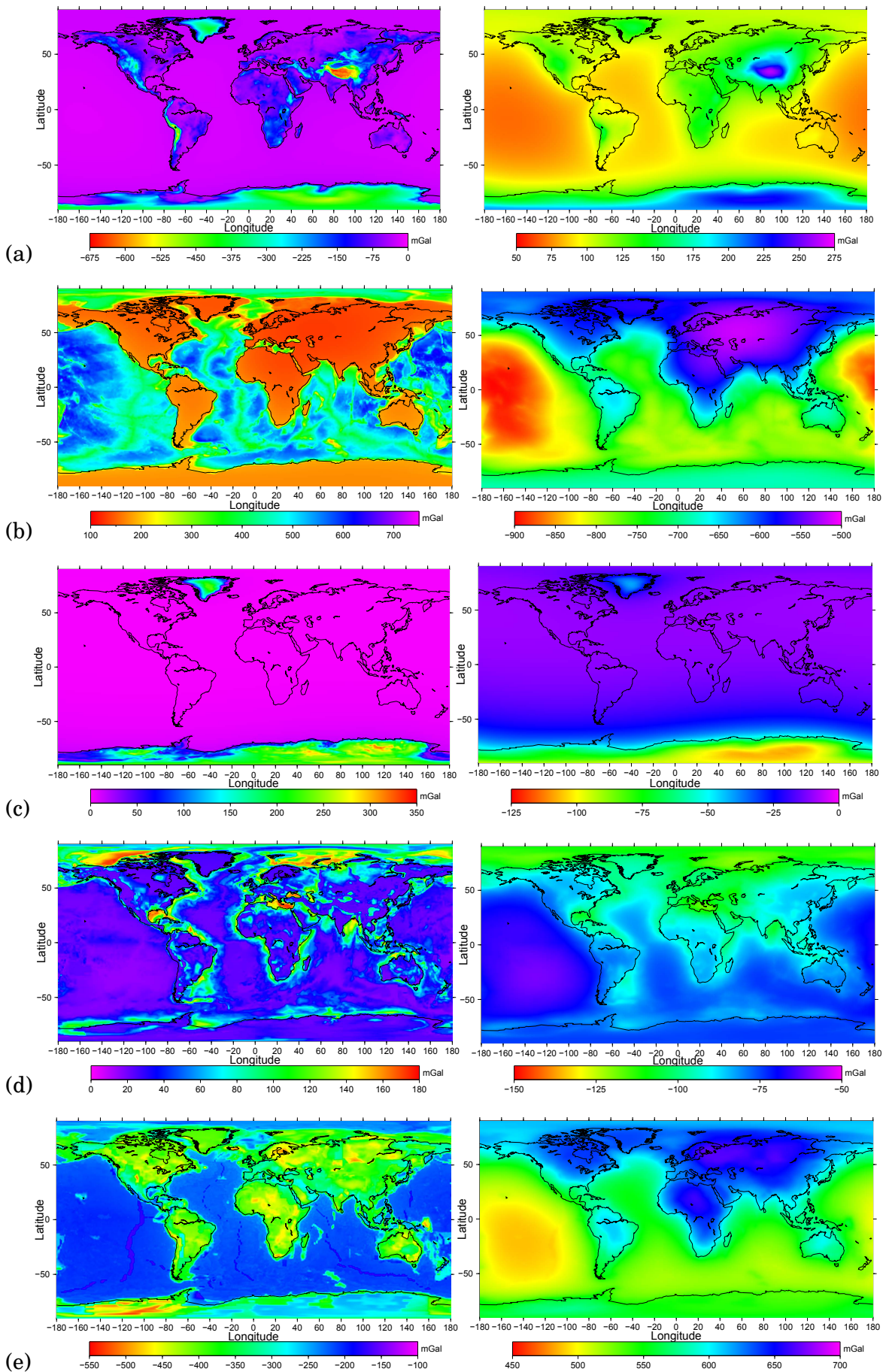


**Figure 4.1** Direct corrections (left), and the secondary indirect corrections (right) (a) topography, (b) bathymetric, (c) ice, (d) sediments, and (e) crust.

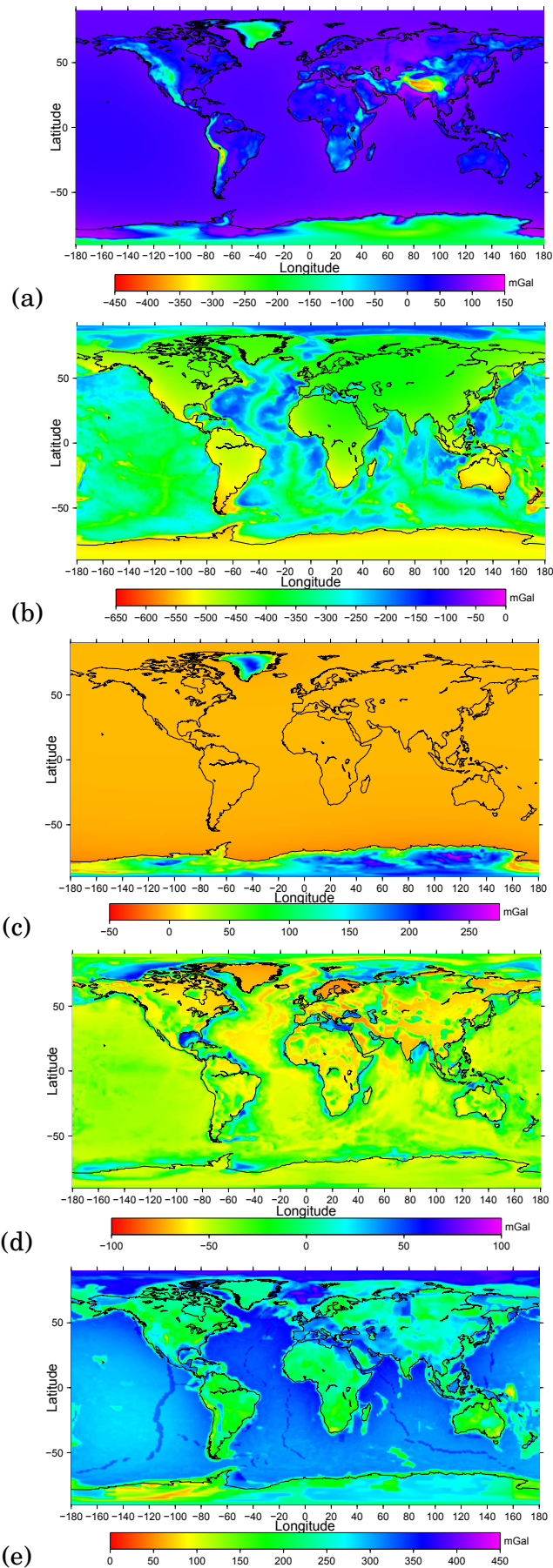


**Figure 4.2** Total corrections: (a) topography, (b) bathymetry, (c) ice, (d) sediments and (e) crust.

**Table 4.3** Statistics of ellipsoid-referenced total correction

Total correction (Relative to $2670 \text{ kg/m}^3$ )	Min (mGal)	Max (mGal)	Mean (mGal)
Topography	-415	137	42
Bathymetry	-642	-62	-373
Ice	-52	218	-1
Sediments	-84	68	-40
Crust	45	412	278

ellipsoid and the sea bottom, is computed as follows. For the inner-zone we have used the ETOPO1,  $1' \times 1'$  global bathymetry model. The computation has been performed using the analytical constant density polyhedral method given by Eq. (3.72). The constant density prism methods given by Eqs. (3.12) and semi-analytical method for constant density spherical shell given by Eq. (3.10) are used for the computation of near and far-zone contribution, respectively. The mean value of the ocean residual density of  $-1640 \text{ kg/m}^3$  (i.e., the difference between the mean ocean seawater density of  $1030 \text{ kg/m}^3$  and the reference crustal density of  $2670 \text{ kg/m}^3$ ) is adopted. The ellipsoid-referenced bathymetry correction to the gravity disturbances varies from 129 to 705 mGal with the mean of 331 mGal and the standard deviation of 163 mGal. The maxima are located above the oceanic trenches, and the minima in the central parts of the continental regions. The oceanic trenches and the convergent ocean-to-continent tectonic plate boundaries represent the regions with the largest variations of the bathymetry correction.

The statistics of direct, secondary indirect and total correction related to the bathymetry are given in Tables 4.1, 4.2, and 4.3, respectively. The corresponding maps of direct and indirect corrections are given in Figure 4.1b, while the total correction is presented in Figure 4.2b. The bathymetric correction takes up maximum values in deep ocean areas and minimum values on the continents (see Figure 4.1b).

### 4.1.3 Ellipsoid-referenced topographic and bathymetric stripping correction

In the beginning of the chapter, we have argued that the geophysical interpretation of gravity data requires the computation of the ellipsoid-referenced topographic and bathymetric corrections, as opposed to the commonly used geoid-referenced ones. Figure 4.3 illustrates the difference between the ellipsoid-referenced and

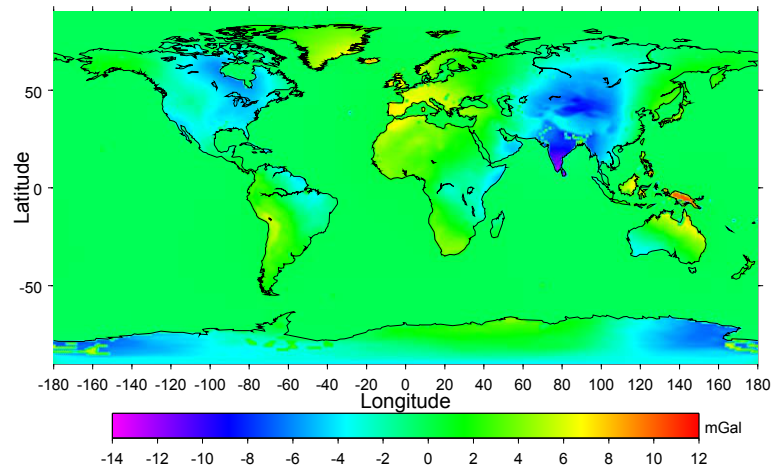


**Figure 4.3** The difference between the ellipsoid-referenced and geoid-referenced bathymetric and topographic correction.

geoid-referenced bathymetric and topographic corrections. Though the magnitude of the correction is rather small, the differences are systematic over larger areas, and therefore, they must be taken into account.

The difference between the geoid-referenced and the ellipsoid-referenced global topographic corrections is the gravitational attraction of the ocean water enclosed between the surfaces of the geoid and reference ellipsoid (liquid topography offshore), accounting for the water surplus or deficiency, and the gravitational attraction of the topographic masses onshore (of constant reference topographic density) enclosed between the same two surfaces. The spherical harmonic coefficients of EIGEN-6C2 (Förste et al., 2013) complete to degree and order 180 were used to compute the global geoidal undulations. The attraction due to liquid topography (of constant mean ocean water density of  $1030 \text{ kg/m}^3$ ) is positive everywhere over the oceans, because the computation points (offshore) are on the geoid (sea surface), thus either above the water surplus (positive geoidal undulations) or below the water deficit (negative geoidal undulations). It varies between 0 and 4.5 mGal with the mean of 0.7 mGal and standard deviation of 0.8 mGal. The attraction of the solid topographic masses onshore enclosed between the surfaces of the geoid and reference-ellipsoid varies between  $-12.2$  and  $10.3$  mGal with mean of  $-0.4$  mGal and standard deviation of 2.0 mGal. The ellipsoid-referenced topographic correction is obtained by subtracting the attractions of topographic and ocean masses enclosed between the geoid and reference ellipsoid from the geoid-referenced topographic correction.

The ellipsoid-referenced bathymetry correction has been obtained by subtracting

from the geoid-referenced bathymetry correction the attraction of the ocean water residual density ( $-1640 \text{ kg/m}^3$ ) offshore enclosed between the geoid and reference-ellipsoid. The correction varies between  $-7.2$  and  $0.0$  mGal with mean of  $-1.0$  mGal and standard deviation of  $1.2$  mGal.

#### 4.1.4 Ice stripping corrections

We have used the ice data from ETOPO1 model. We have computed the ice stripping corrections for the three zone as mentioned in the previous section. The adopted value of the ice residual density is  $-1757 \text{ kg/m}^3$  (i.e., the difference between the mean ice density of  $913 \text{ kg/m}^3$  and the reference crustal density of  $2670 \text{ kg/m}^3$ ). The statistics of direct, secondary indirect and total correction related to the ice are given in Tables 4.1, 4.2 and 4.3, respectively. The maps of direct stripping and secondary indirect stripping correction are presented in Figure 4.1c. The map of the total correction is depicted in Figure 4.2c. The maximum and minimum values of the ice correction are  $319$  mGal and  $2$  mGal, respectively, while the standard deviation is  $56$  mGal. For ice correction the maximum value is found at the region of Antarctica and Greenland, whereas the remaining parts of the globe has the minimum value (see Figure 4.1c).

#### 4.1.5 Sediment corrections

The  $1^0 \times 1^0$  global data set of the upper, middle and lower sediment thickness and density from the CRUST 1.0 is used to compute the sediment stripping correction. The values of residual density of sediment, i.e., the difference between the actual laterally varying sediment density and the reference crust density have been used for the stripping correction of sediments. Information about sediments in CRUST 1.0 is taken over from an independent model produced by Laske (1997). The maximum total thickness of marine sediments reaches  $20$  km, and the average thickness is about  $1.2$  km. The thickness of sediment at the bottom of deep oceans is less than  $2$  km. Large sediment accumulations are beneath marginal seas, with maximum sediment thickness. The largest sediment accumulation are due to river discharge. The sediment accumulations at oceanic sedimentary basin is typically very low.

We have adopted the same strategy as for the ice stripping correction. Each individual stripping correction (for upper, middle and lower sediment layers) has been computed and then added to make the total sediment correction. We have used the laterally varying densities of upper, middle and lower sediments and have taken the sediment residual density as the difference of actual sediment density and the reference crustal density of  $2670 \text{ kg/m}^3$ . The maxima of the correction are located over the areas with largest sediment deposits in the continental shelves and the Caspian Sea region. The minima are in Greenland and Antarctica, and across the central parts of the Pacific, Atlantic, and the Indian Ocean. The statistics of direct, indirect and total corrections related to sediments are given in Tables 4.1, 4.2 and 4.3, respectively. The maps of direct corrections and indirect corrections are given in Figure 4.1d, and the total correction map is shown in Figure 4.2d. It has a maximum value of 174 mGal, a minimum value of 15 mGal with a mean value of 31 mGal over the globe.

#### 4.1.6 Crustal corrections

The  $1^0 \times 1^0$  global data of the density and thickness of the upper, middle, and lower crust components from the CRUST 1.0 have been used to compute the stripping corrections for the remaining consolidated crust. We have taken into account the laterally varying densities of each individual crust layer. The inhomogeneity of upper, middle and lower crust are mostly far away from the computation point (Earth surface) as compared to previously mentioned corrections, therefore we neglect the inner zone and work with only two zones; one is the near zone with a radius of 50 km, and the other is the far zone which corresponds to the remainder of the globe. For the computation of the corrections we used the analytical prism method for the near zone and the semi-analytical method for the far zone, respectively. The statistics of direct, secondary indirect and total correction related to the corresponding crustal components are given in Tables 4.1, 4.2 and 4.3, respectively. The maps of direct and secondary indirect corrections are given in Figure 4.1e and the total correction is shown in Figure 4.2e. The maximum value for the total crust correction is -170 mGal, minimum of -527 mGal and mean value of -289 mGal for the Earth crust. The minima is found in the Himalaya region and maxima in the oceanic region.



## 4.2 Stripped gravity disturbances and gravity anomalies

We have used the EIGEN-6C2 model (Förste et al., 2013) to compute gravity disturbances and gravity anomalies on a one-degree global equal-angular grid. The resulting gravity disturbances and gravity anomalies are shown in Figures 4.4a and 4.4b, respectively. The stripped corrected gravity disturbances and gravity anomalies has been obtained by subsequent applications of the individual corrections as described in Section 4.1. Statistics of the stepwise stripped corrected gravity disturbances and gravity anomalies are summarized in Tables 4.4 and 4.5, respectively.

The expressions for the crust stripped gravity disturbance  $\delta g^{\text{TBISC}}$  and the corresponding gravity anomaly  $\Delta g^{\text{TBISC}}$ , is given by

$$\delta g^{\text{TBISC}} = \delta g + \Delta g_{rs} = \delta g + g^t + g^b + g^i + g^s + g^c, \quad (4.6)$$

and

$$\Delta g^{\text{TBISC}} = \delta g^{\text{TBISC}} - \frac{2}{r} (T + V^t + V^b + V^i + V + V^c), \quad (4.7)$$

where  $r$  is the geocentric radius of the computation point;  $T$  is the disturbance gravity potential;  $\Delta g_{rs} = g^t + g^b + g^i + g^s + g^c$ , is the sum of gravitational attraction due to residual density.  $V^t$ ,  $V^b$ ,  $V^i$ ,  $V^s$  and  $V^c$  are the gravitational potentials generated by the topography and residual density of ocean, ice, sediments, and remaining anomalous density structures within the Earth's crust, respectively. The respective gravitational attractions in Eq. (4.6) are denoted as  $g^t$ ,  $g^b$ ,  $g^i$ ,  $g^s$  and  $g^c$ .

The topographically-corrected gravity disturbances  $\delta g^{\text{T}}$  and gravity anomalies  $\Delta g^{\text{T}}$  are depicted in Figures 4.5a and 4.5b, respectively. Compared to the original gravity disturbances, the topographically-corrected gravity disturbances  $\delta g^{\text{T}}$  change significantly in the mountainous regions and become predominantly negative revealing the presence of the isostatic compensation.

The bathymetrically and topographically corrected gravity disturbances  $\delta g^{\text{TB}}$  and gravity anomalies  $\Delta g^{\text{TB}}$  (see Figures 4.5c and 4.5d) are computed by applying the bathymetry correction to the topographically-corrected gravity disturbances and anomalies. Since the bathymetric correction over the continental areas is small

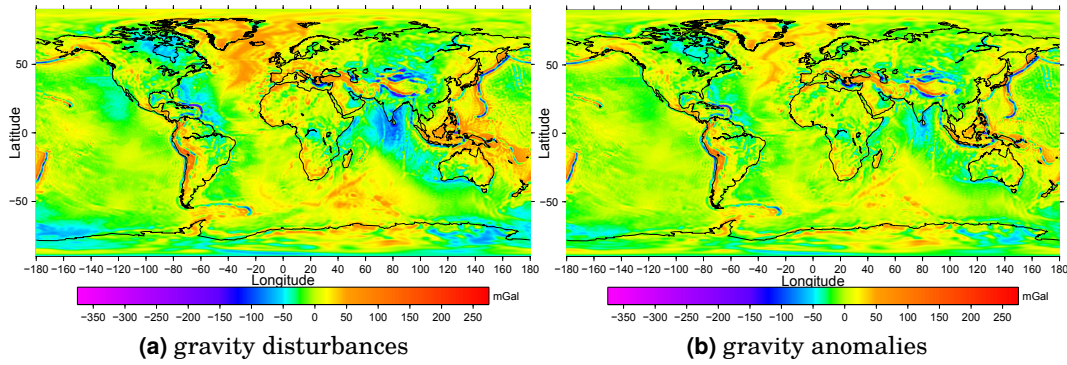


**Figure 4.4** (a) Gravity disturbances ( $\delta g$ ) (b) gravity anomalies ( $\Delta g$ ) at the Earth's surface.

**Table 4.4** Statistics of sequentially corrected gravity disturbances (the superscripts 'T' stands for topography; 'TB' for topography and bathymetry; 'TBI' for topography, bathymetry, and ice; 'TBIS' for topography, bathymetry, ice, and sediments; and 'TBISC' for topography, bathymetry, ice, sediments, and crust).

Gravity disturbances	Min (mGal)	Max (mGal)	Mean (mGal)
$\delta g$	-303	294	-0.7
$\delta g^T$	-637	191	-70
$\delta g^{TB}$	-499	656	261
$\delta g^{TBI}$	-496	659	283
$\delta g^{TBIS}$	-474	687	328
$\delta g^{TBISC}$	-906	466	39

and has mostly a long-wavelength character, the higher-frequency pattern of the gravity disturbance signal onshore remains almost unchanged. Over the oceans, the application of the bathymetric correction to the topographically-corrected gravity disturbance show the global pattern of the oceanic lithospheric plates.

The ice and sediment residual density stripping corrections transform the volumetric domain of the global ice mass (Greenland and Antarctica) and global sediments from their actual densities to the constant reference crustal density. The laterally-varying densities for upper, middle and lower sediments from CRUST 1.0 model have been used. The ice and sediment corrected gravity disturbances  $\delta g^{TBIS}$  and gravity anomalies  $\Delta g^{TBIS}$  are shown in Figures 4.5e and 4.5f, respectively. Compared to the bathymetry and topography corrections, the signature of the ice and sediment corrections is less noticeable. The ice correction changed the topo-

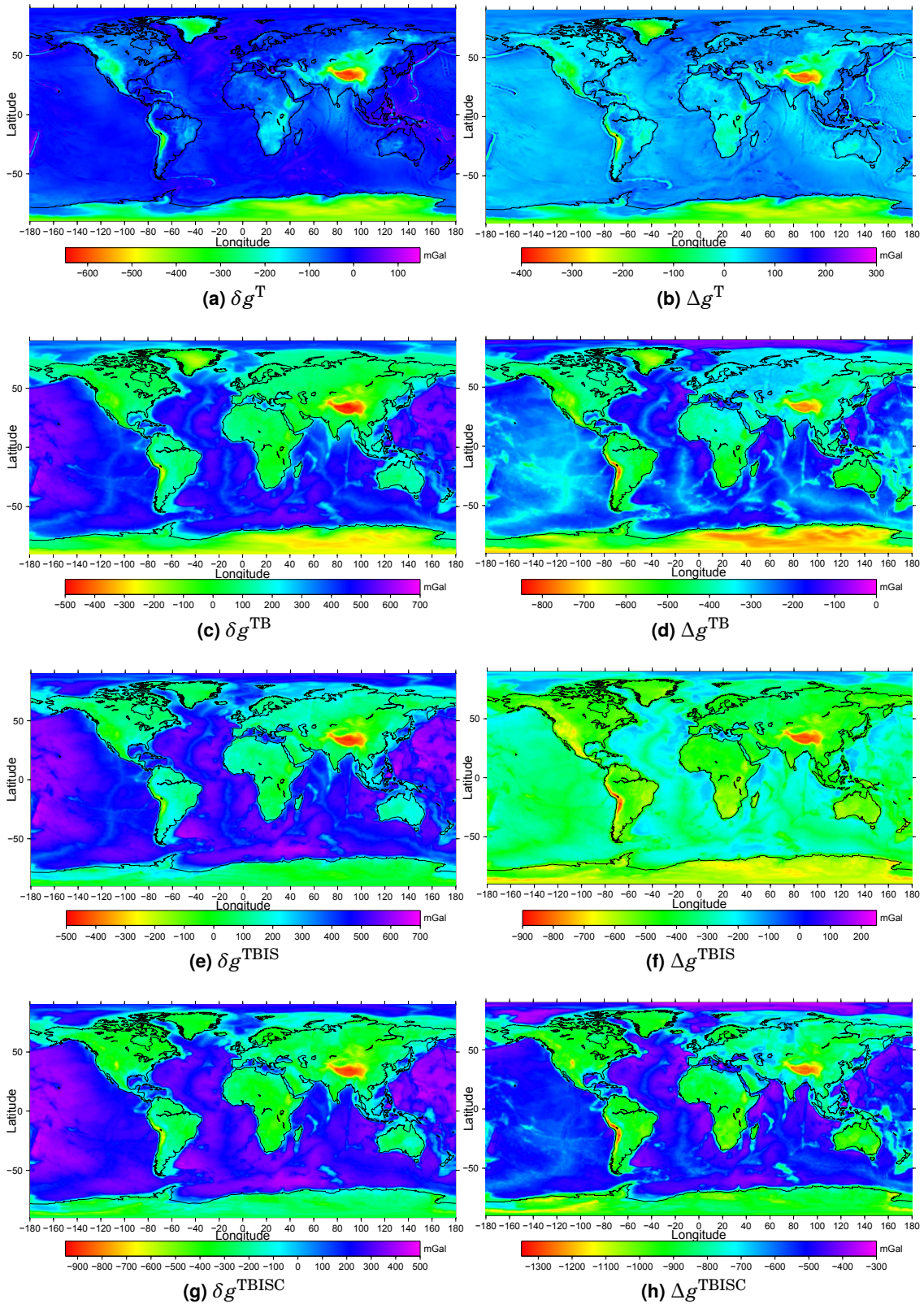


**Figure 4.5** Gravity disturbances (left) and gravity anomalies (right), from top to bottom: sequentially corrected for topography, bathymetry, ice and sediments, and crust heterogeneities.

**Table 4.5** Statistics of sequentially-corrected gravity anomalies.

Gravity anomalies	Min (mGal)	Max (mGal)	Mean (mGal)
$\Delta g$	-282	284	-0.5
$\Delta g^T$	-376	259	41
$\Delta g^{TB}$	-822	-14	-331
$\Delta g^{TBI}$	-833	-23	-332
$\Delta g^{TBIS}$	-889	-32	-372
$\Delta g^{TBISC}$	-1345	-297	-662

graphically and bathymetrically corrected gravity disturbances  $\delta g^{TB}$  in Greenland and Antarctica. The sediment correction primarily changed the topographically and bathymetrically corrected gravity disturbances over the areas with the largest sediment thickness at continental shelves and in the Caspian Sea region.

The remaining consolidated crust residual density correction replaces the density of the upper, middle, and lower CRUST 1.0 crustal components with the constant reference density of  $2670 \text{ kg/m}^3$ . When this correction is applied to the ice, sediment, topographically and bathymetrically corrected gravity disturbances  $\delta g^{TBIS}$  and gravity anomalies  $\Delta g^{TBIS}$ , it produces corrected gravity disturbances  $\delta g^{TBISC}$  and gravity anomalies  $\Delta g^{TBISC}$ , shown in Figures 4.5g and 4.5h, respectively. The consolidated gravity disturbances  $\delta g^{TBISC}$  and gravity anomalies  $\Delta g^{TBISC}$  corresponds to a model Earth consisting of no topography, a constant  $2670 \text{ kg/m}^3$  reference crust density down to the Moho interface, and the real Earth's sub-Moho density distribution. The statistics of consolidated crust-stripped gravity disturbances and gravity anomalies are given in Tables 4.4 and 4.5, respectively.

### 4.3 Accuracy of the corrections applied

It is important to consider the model uncertainties associated with the topography and the crust when the corrections are computed. The uncertainties in modelling the global topographic correction relatively to the average topographic density are difficult to estimate in the global field due to the lack of knowledge on the actual topographic density globally. They may be anticipated at the level of a few tens of

mGal. The uncertainties in modelling the global bathymetry correction due to the deviation of the actual seawater density from constant model ocean water density (of about -10 to 20 kg/m<sup>3</sup>) are up to 1.5 mGal. [Tenzer et al. \(2012a\)](#) reported an error up to 17 mGal, based on errors in gravity modeling. The uncertainties in the remaining corrections are also hard to estimate, but may be anticipated at the level from a few tens to about 100 mGal over continents and up to 40 mGal over oceans ([Kaban et al., 2003](#)). They are mostly due to the heterogeneities of the consolidated crust, especially over continents.

## 4.4 Discussion

To match the resolution of the CRUST 1.0 global crustal models, we have computed the global corrections and the global gravity disturbances and anomalies at  $1^{\circ} \times 1^{\circ}$  grid on the Earth surface. A higher spatial resolution may be adopted once a global crustal model of higher resolution becomes available. Our objective was to compute and apply global crustal stripping corrections, based on a best currently available global crustal model. The upper, middle and lower sediments components, as well as density variability, reflect to a certain degree the increasing density of sediments with depth due to compaction. In regional studies, a more accurate dependence of sediment density on depth may be adopted for sedimentary basins (cf. [Artemjev et al., 1994](#)). In spite of the already-conducted investigations, there is still room for further improvements, by incorporating new or more accurate geophysical/geoscientific constraints and by improving the crustal models used when computing stripping corrections.

[Tenzer et al. \(2009a\)](#) computed topography, bathymetry, ice, sediment, and crust residual density corrections, and sequentially corrected gravity disturbances. For these corrections, they have used data of CRUST 2.0 model. The values of our computed corrections are comparable with the results of [Tenzer et al. \(2009a\)](#). Our estimated values for topography and sediments corrections are slightly greater than the earlier estimated values. Whereas, our estimated values of bathymetry and ice corrections are slightly lower. These difference are probably due to a higher resolution and accuracy of CRUST 1.0, as compared to CRUST 2.0. [Bagherbandi et al. \(2013\)](#) computed the topography, bathymetry and sediment corrections and gravity disturbances using data of CRUST 2.0 model in spectral domain . His results

are also comparable with our result, there are slightly differences of few mGal in bathymetry, and sediments corrections. The minimum and maximum values for the topographic correction from the study of [Tenzer et al. \(2009a\)](#) is -619 mGal 71 mGal, and from the study of [Bagherbandi et al. \(2013\)](#) -659 mGal and -19 mGal, and from this study -657 mGal and -17 mGal, respectively. Similarly, for bathymetric correction, from the study of [Tenzer et al. \(2009a\)](#) is 129 mGal 715 mGal, and from the study of [Bagherbandi et al. \(2013\)](#) 127 mGal and 650 mGal, and from this study 129 mGal and 705 mGal, respectively.

## 4.5 Summary

The global topographic, bathymetric, ice, sediments and crust stripping corrections for the major known residual density are computed using the input data from GTOPO30C, ETOPO1, and CRUST 1.0 models. These corrections are applied to clean gravity disturbances and gravity anomalies from signal due to topography, bathymetry and the inhomogeneity of the crust assuming a known residual density. The residual density include the effects of sea water, ice, sediments, and upper, middle, lower crust and are taken relatively to the adopted value of the reference crustal density of  $2670 \text{ kg/m}^3$ . Furthermore, we compute the correction due to the masses enclosed between the geoid and the surface of reference ellipsoid.

In next chapter, the correlation of gravity fields functionals (gravity disturbances and gravity anomalies) with different physical interfaces (topography, bathymetry, and Moho) are discussed. We will demonstrate that corrected gravity disturbances, are highly correlated with the a priori Moho as compared to the corrected gravity anomalies. These highly-correlated (with Moho) gravity disturbances and anomalies are used to investigate the global crust-mantle density contrast, which is treated as a constant in the Moho recovery from gravity data.

---

## Estimation of global crust-mantle density contrast

In this chapter we investigate the correlation of gravity disturbances and anomalies with topography, bathymetry and Moho depth. The purpose of this investigation is to show that the application of sequential correction to gravity field functionals reduces nuisance signals in gravity data and hence make them best suited for the recovery of global Moho density contrast. Our investigation is based on to find the correlation between the sequentially corrected gravity disturbances/anomalies with the prior Moho model from CRUST 1.0. We will show that the gravity disturbances data are more correlated with Moho depth than gravity anomalies data. Furthermore, we apply an empirical method to estimate the global Moho density contrast using gravity disturbances and anomalies. In this method, we replace the Earth crust with mantle density using different values of crust-mantle density contrast and then estimate the correlation between the updated gravity disturbances and anomalies with the Moho depth. The value that yields zero correlation is selected as an estimate of the actual crust-mantle density contrast. For this estimation we use the Moho depth from a priori model, in our case from CRUST 1.0.

The estimation of the crust-mantle density contrast is done using two types of gravity data, namely the consolidated crust-stripped gravity disturbances and the corresponding gravity anomalies. The consolidated crust stripped gravity disturbances differ significantly from the corresponding gravity anomalies due to large contributions of the secondary indirect effects. The methodology used for the preparation of gravity data and computation of correlation is discussed in Section 5.1.

The correlation of gravity disturbances and anomalies with topography, bathymetry and Moho depth are discussed in Sections 5.2, 5.3 and 5.4, respectively. The global crust-mantle density contrast is estimated in Section 5.5. Finally, the summary and conclusions are given in Section 5.6.

The density contrast of crust-mantle is traditionally assumed to be  $600 \text{ kg/m}^3$  (e.g., Heiskanen, 1967). Martinec (1994) have claimed that this value corresponds well with the Moho density contrast only over the ocean. For the continental areas, he estimated crust-mantle density contrast of  $280 \text{ kg/m}^3$  by minimising the external gravitational potential induced by the Earth's topographic masses and the Moho discontinuity. The continental Moho density contrast of  $200 \text{ kg/m}^3$  has been reported by Goodacre (1972) for Canada. Dziewonski and Anderson (1981) (see Table 1) adopted the value of  $480 \text{ kg/m}^3$  for the global crust-mantle density contrast in the definition of the Preliminary Reference Earth Model (PREM). In PREM the value of density contrast is derived using seismic reflection data. The density contrast across the Moho boundary has also been determined regionally from seismological studies using the wave receiver functions (e.g., Niu and James, 2002, Julia, 2007). The results of these studies indicate that the density contrast across Moho may regionally vary from  $160 \text{ kg/m}^3$  (for the mafic lower crust) to  $440 \text{ kg/m}^3$  (for the felsic lower crust). Tenzer et al. (2009b) estimated that the average value of the crust-mantle density contrast is about  $520 \text{ kg/m}^3$ . Recently, Sjöberg (2011a) have solved Moritz's generalisation of the Vening-Meinesz inverse problem of isostasy, and have estimated that the Moho density contrast varies globally from  $81.5 \text{ kg/m}^3$  in the Pacific region to  $988 \text{ kg/m}^3$  in Tibet, with the average values of  $678 \pm 78$  and  $334 \pm 108 \text{ kg/m}^3$  for the continental and oceanic areas, respectively. That research has also concluded that the global average of the Moho density contrast is  $448 \pm 187 \text{ kg/m}^3$ . This estimated value ( $480 \text{ kg/m}^3$ ) is approximately 7% smaller than the value adopted ( $480 \text{ kg/m}^3$ ) in PREM.

We adopt the reference crustal density of  $2,670 \text{ kg/m}^3$ . This value is often assumed for the upper continental crust in geological and gravity surveys, geophysical exploration, gravimetric geoid modelling, compilation of regional gravity maps, and other applications. Although this density value is widely used, its origin remains partially obscure. Woollard (1966) argues that this density was used for the first time by Hayford (1912). In reviewing several studies seeking a representative average density from various rock type formations, Hinze (2003) argued that this value was used earlier by Hayford (1909b) for gravity reduction. Hayford (1909b) referred to



Harkness (1891) who averaged five published values of surface rock density. Harkness (1891) value of  $2,670 \text{ kg/m}^3$  was confirmed later, for instance, by Gibb (1968), who estimated an average density for the surface rocks in a significant portion of the Canadian Precambrian shield from over 2,000 individual measurements of rock samples. Woollard (1962) examined more than 1,000 rock samples and estimated that the average basement (crystalline) rock density is about  $2,740 \text{ kg/m}^3$ . Subrahmanyam (1981) determined that crystalline rocks in India have an average density of  $2,750 \text{ kg/m}^3$  in low-grade metamorphic terrains and  $2,850 \text{ kg/m}^3$  in high-grade metamorphic terrains. We note here that the choice of the reference crustal density is somewhat optional, depending on a particular purpose of the study. For example, for the regional studies, one needs to work with the values that better correspond to the region.

When solving the inverse problem for the Moho recovery most of the author assume a constant value of the Moho density contrast. For example, Tugume et al. (2013) has been used a constant value of crust-mantle density contrast  $200 \text{ kg/m}^3$ . They have also tested different contrast values between 100 to  $300 \text{ kg/m}^3$  with an interval of  $50 \text{ kg/m}^3$ , and have claimed that the results didn't show much variation of crust thickness.

The presented study is based on using most recent gravity field model together with crust models. There are two major reasons for estimating the average value of the crust-mantle density contrast. In the context of a global recovery of the Moho density interface from gravimetric data, this value is a required parameter in the functional model relating the (known) consolidated crust stripped gravity disturbances and (unknown) crustal-thickness data. We have removed all the nuisance signals and replaced the crust with constant reference density and hence the data only contain the signal due to Moho density contrast. When speaking of the Moho interface density contrast or the crust-mantle density contrast, we have to distinguish between the contrast of the lower crust with respect to the upper mantle, and the average crust density with respect to the mantle. The consolidated crust stripped gravity field (used to estimate the crust-mantle density contrast) describes the gravity field generated by the Earth of which all the masses outside the Earth's ellipsoid are removed and the known crust density distribution is replaced by a reference crustal density. We have used two type of gravity data i.e., gravity disturbances and gravity anomalies for the investigation of correlation and for the crust-mantle density contrast. There are two reason for taking the two type of gravity data. One

is to demonstrate that after applying the sequential correction to gravity disturbances and gravity anomalies remove successfully the signals due to topography, bathymetry, ice, sediment, and other inhomogeneities of the crust and hence its correlation with Moho geometry is increases. The other reason is to demonstrate that the gravity disturbances have the most prominent local nature i.e., the link between the density variations and gravity disturbances is more prominent as compared to gravity anomalies. The gravity anomalies have the term associated with indirect effect. The indirect effect are directly associated with potential. The signal related to the potential decay slowly as compare to the signal related to the attraction, and hence the gravity anomalies contains more signals from mantle heterogeneities and other deeper structure as compare to the gravity disturbances.

## 5.1 Methodology

Pearson's correlation coefficient (Pearson, 1896) is used to describe the correlation of the topography, bathymetry, and Moho depth with gravity disturbances and anomalies.

The correlation coefficient  $k_{ab}$  for two data set  $a$  and  $b$  is given by

$$k_{ab} = \frac{\sum_{i=1}^I (a_i - \bar{a})(b_i - \bar{b})}{(I-1)\sigma_a\sigma_b}, \quad (5.1)$$

where  $\bar{a}$  and  $\bar{b}$  are the average values of  $a$  and  $b$  over the area of study, respectively;  $\sigma_a$  and  $\sigma_b$  are the corresponding standard deviations, and  $I$  quantifies the total number of data points in the area of study. The average values are computed using the latitudinal dependent weights:

$$\bar{a} = \frac{\sum_{i=1}^I a_i \cdot \cos \phi_i}{\sum_{i=1}^I \cos \phi_i},$$

where  $\phi$  is the spherical latitude.

The standard deviations are given by

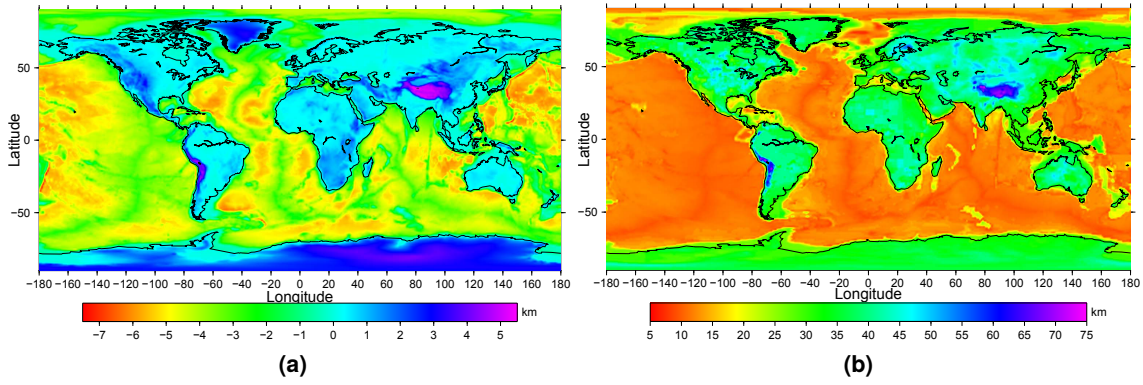


**Figure 5.1** (a) The global topography and bathymetry, (b) The depth of the Moho boundary;  $1^0 \times 1^0$  discrete data from CRUST 1.0.

$$\sigma_a = \sqrt{\frac{\sum_{i=1}^I (a_i - \bar{a})^2}{(I - 1)}},$$

The correlations are investigated globally for the gravity disturbances and gravity anomalies. The global topography and bathymetry used for the correlation are shown in Figure 5.1a. The Moho depth (shown in Figure 5.1b) used for the calculation of correlation is taken from  $1^0 \times 1^0$  CRUST 1.0 model (Laske et al., 2013).

## 5.2 Correlation of gravity field quantities with topography

The relation between various step-wise corrected stripped gravity disturbances evaluated at the Earth's surface and the corresponding topographic height  $H$  of the computation points above the geoid is shown in Figure 5.2. The corresponding correlation coefficients computed over the continents are given in Table 5.1. As it is depicted in Figure 5.2a, there is no significant correlation between the observed gravity disturbances ( $\delta g$ ) and the topographic height  $H$ . It reveals the isostatic compensation of the Earth crust. The corresponding correlation coefficients have the value of only 0.10 (see Table 5.1). A significant correlation of the topography corrected gravity disturbances ( $\delta g^T$ ) and bathymetry corrected gravity disturbances ( $\delta g^{TB}$ ) with the topography is depicted in Figures 5.2b and 5.2c, respectively. In both cases, the dispersion of gravity disturbances at a particular computation point is mostly within 100 mGal, except over the oceans and the regions with low elevations,

where it reaches about 150 mGal and 200 mGal for the topography corrected gravity disturbances ( $\delta g^T$ ) and for the bathymetry corrected gravity disturbances ( $\delta g^{TB}$ ), respectively. On the other hand, the dispersion of observed gravity disturbance ( $\delta g$ ) is more than 300 mGal. The decrease in dispersion of gravity data reveals that they get smoothed by the application of topography and bathymetry corrections. Over the continents, the topography corrected gravity disturbances ( $\delta g^T$ ) have the highest negative correlation (among all the investigated types of gravity disturbances) with the topography, i.e., -0.97 (see Table 5.1). This large negative correlation is mainly due to the presence of the isostatic compensation in the mountain regions. It means that in the absence of topography correction the gravity corresponds to the isostatically adjusted Earth. The bathymetry-corrected gravity disturbances has nearly the same correlation with the topography over the continents (i.e., -0.96). The application of the ice and sediment corrections to the bathymetry-corrected gravity disturbances significantly reduces the correlation with the topography: to -0.72. Compared to the bathymetry-corrected gravity disturbances the dispersion of ( $\delta g^{TBIS}$ ) is larger as shown in Figure 5.2d. The reason is that the application of the ice correction to the bathymetry-corrected gravity disturbances ( $\delta g^{TB}$ ) substantially decreases a large negative contribution of the topographical correction. Consequently, it increases the dispersion of gravity disturbances over the ice sheets in Antarctica and Greenland. Analogically, the application of the sediment correction increases the dispersion of gravity disturbances over the continental regions with large sediment deposits, due to the fact that the densities of the upper, middle, and lower sediment components are lower than the adopted average topographical reference crust density. The application of the crust correction which results in the consolidated crust stripped gravity disturbances ( $\delta g^{TBISC}$ ) further decreases the absolute value of the correlation coefficient to -0.52. The reason of this decrease is the reduction of excess masses in the crust.

The correlation of the observed gravity disturbances and gravity anomalies with the topography is similar (the difference is merely 0.04, as shown in Table 5.1). Nevertheless, the correlation coefficient of the stripped gravity disturbances and the corresponding gravity anomalies with the topography are not very similar (see Table 5.1). It also reveals that gravity anomalies are less correlated with topography than the gravity disturbances. As early stated the gravity disturbances have prominent features associated with local variations in the density and hence it successfully remove the signals due to different inhomogeneities. Furthermore, the gravity

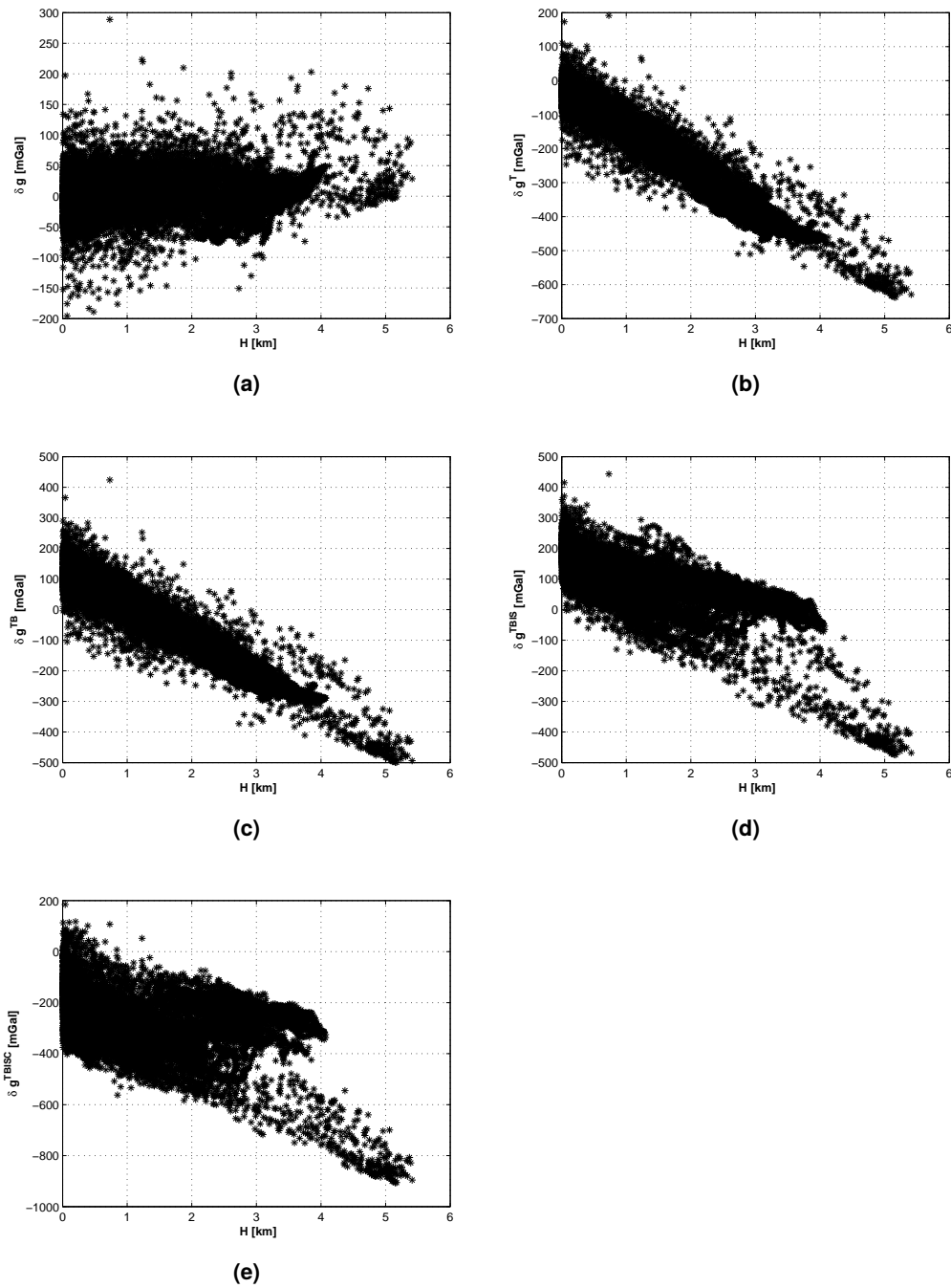


**Figure 5.2** The relation between the topography  $H$  and sequentially corrected gravity disturbances: (a) observed  $\delta g$ , (b) topography corrected  $\delta g^T$ , (c) topography and bathymetry corrected  $\delta g^{TB}$ , (d) topography, bathymetry, ice, and sediment corrected  $\delta g^{TBIS}$  and (e) topography, bathymetry, ice, sediment and consolidated crust corrected  $\delta g^{TBISC}$ .

**Table 5.1** Pearson's correlation of the sequentially corrected gravity field quantities with the topography  $H$  over the continents.

Type	Gravity disturbances	Gravity anomalies
Earth	0.14	0.10
Topography corrected	-0.97	-0.94
Topography and bathymetry (TB) corrected	-0.96	-0.90
Topography, bathymetry, ice and sediment corrected (TBIS)	-0.72	-0.65
Topography, bathymetry, ice, sediment and crust corrected (TBISC)	-0.52	-0.42

disturbances contains less signal of deep inhomogeneities as compared to gravity anomalies.

### 5.3 Correlation of gravity field quantities with bathymetry

The relation between the stripped gravity disturbances evaluated at the ocean surface and the ocean depth  $D$ , taken from CRUST 1.0 is shown in Figure 5.3. The observed gravity disturbances ( $\delta g$ ) are practically uncorrelated with the bathymetry over the oceans as shown in Figure 5.3a, their correlation is only -0.22 (see Table 5.2). The dispersion of the gravity disturbances evaluated at the ocean surface is mostly within the range of 250 mGal. As shown in Figure 5.3b, the application of the topography correction to the observed gravity disturbances at the ocean surface changed this dispersion to about 200 mGal over the shelf seas. The correlation of the topography corrected gravity disturbances ( $\delta g^T$ ) with bathymetry increases to 0.26. Due to the location of topography (mostly away from ocean surface), the application of topography correction reduces the dispersion of gravity data only slightly. The application of the bathymetry correction to the topography corrected gravity disturbances leads to a strong correlation between the bathymetry corrected

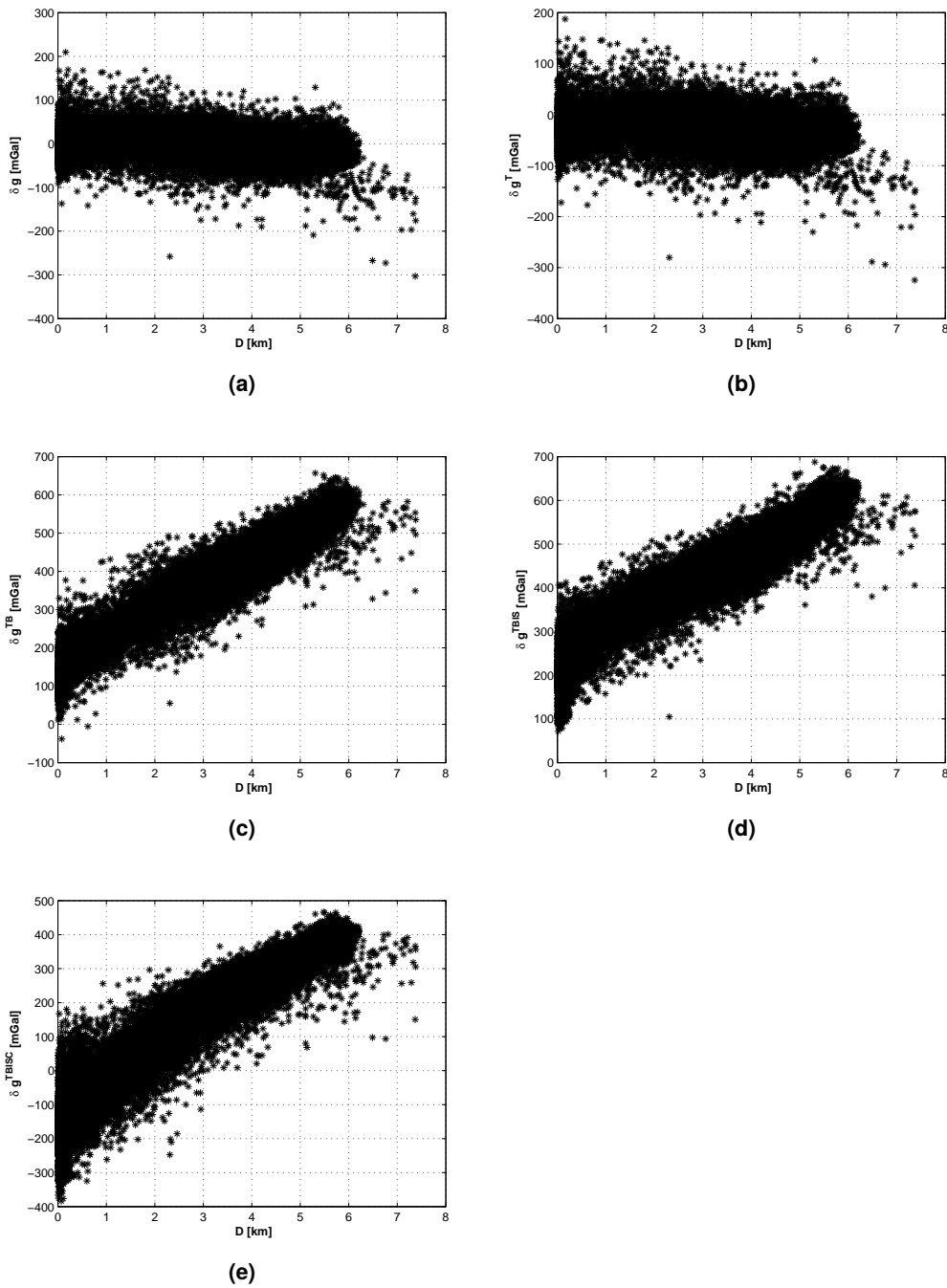


**Figure 5.3** The relation between the Ocean depth  $D$  and sequentially corrected gravity disturbances: (a) observed  $\delta g$ , (b) topography corrected  $\delta g^T$ , (c) topography and bathymetry corrected  $\delta g^{TB}$ , (d) topography, bathymetry, ice and sediment corrected  $\delta g^{TBIS}$ , and (e) topography, bathymetry, ice, sediment and consolidated crust corrected  $\delta g^{TBISC}$ .

**Table 5.2** Pearson's correlation of the sequentially corrected gravity field quantities with the bathymetry.

Type	Gravity disturbances	Gravity anomalies
Earth	-0.22	-0.23
Topographically corrected	0.26	0.43
Topography and bathymetry (TB) corrected	0.96	0.70
Topography, bathymetry, ice and sediment corrected (TBIS)	0.96	0.76
Topography, bathymetry, ice, sediment and crust corrected (TBISC)	0.95	0.81

gravity disturbances ( $\delta g^{\text{TB}}$ ) and the ocean floor depths  $D$ . The magnitude of the topography and bathymetry corrected gravity disturbances increases with the depth  $D$  of the oceans. Compared to the topography corrected gravity disturbances ( $\delta g^{\text{T}}$ ), the dispersion of the topography and bathymetry corrected gravity disturbances remains almost unchanged. The application of the ice and sediment corrections to the topography and bathymetry corrected gravity disturbances ( $\delta g^{\text{TB}}$ ) does not change the predominantly linear trend in the relationship between the topography and bathymetry corrected gravity disturbances and the ocean floor depths. But the dispersion of corrected gravity disturbances ( $\delta g^{\text{TBIS}}$ ) significantly decreases over the shelf seas, as shown in Figure 5.3d. The correlation coefficient between gravity disturbances ( $\delta g^{\text{TBIS}}$ ) and the bathymetry reaches 0.96. The linear trend and the dispersion of the gravity disturbances remains almost unchanged after applying the crust correction. Similarly, the correlation of the crust corrected gravity disturbances ( $\delta g^{\text{TBISC}}$ ) with the bathymetry over the oceans decreases only slightly, to 0.95.

The correlation between the consolidated crust stripped gravity disturbances and gravity anomalies with the bathymetry over the oceans is summarised in Table 5.2. The observed gravity anomalies ( $\Delta g$ ) have almost the same correlation with the bathymetry over the oceans as the observed gravity disturbances ( $\delta g$ ) (see Table 5.2). The correlation between the step-wise stripped gravity anomalies and the



bathymetry, is also comparable to the correlation in the case of gravity disturbances, although it stays lower in all the cases.

## 5.4 Correlation of gravity field quantities with Moho

The relation between the step-wise stripped gravity disturbances evaluated at the Earth's surface and the depths of the Moho boundary  $H_m$  from the CRUST 1.0 model is shown in Figure 5.4. It can be observed that the sequential application of the corrections to the observed gravity disturbances increases the correlation with the Moho boundary. This is also confirmed by the correlation coefficients given in Table 5.3. The observed gravity disturbances ( $\delta g$ ) are practically uncorrelated globally with the Moho boundary. The dispersion of the gravity disturbances at a given Moho depth is mostly within 400 mGal. After applying the topography correction to the observed gravity disturbances, the correlation with the Moho boundary increases to -0.54. This can also be observed in Figure 5.4b, which shows a tendency of decreasing the topography corrected gravity disturbances ( $\delta g^T$ ) with an increase in the Moho depth  $H_m$  beneath the continental regions. The application of the bathymetry correction further enhances this tendency and extends it to the ocean area. The correlation of the topography and bathymetry corrected gravity disturbances with the Moho boundary increases to -0.89. Finally, the application of the ice, sediment, and crust corrections increases the absolute value of the correlation coefficient with the Moho boundary to 0.95.

Similar to the observed gravity disturbances, the observed gravity anomalies are uncorrelated with the Moho relief, most probably due to the isostatic balance of the Earth's lithosphere. The step-wise application of the corrections significantly increases the correlation of the gravity anomalies with the Moho boundary (see Table 5.3). The correlation of gravity anomalies corrected for all effects reaches in absolute value of 0.88. The correlation of gravity disturbances with Moho is higher as compared to that of gravity anomalies. It again confirmed that gravity disturbances have prominent feature of local density variation as compared to gravity anomalies.

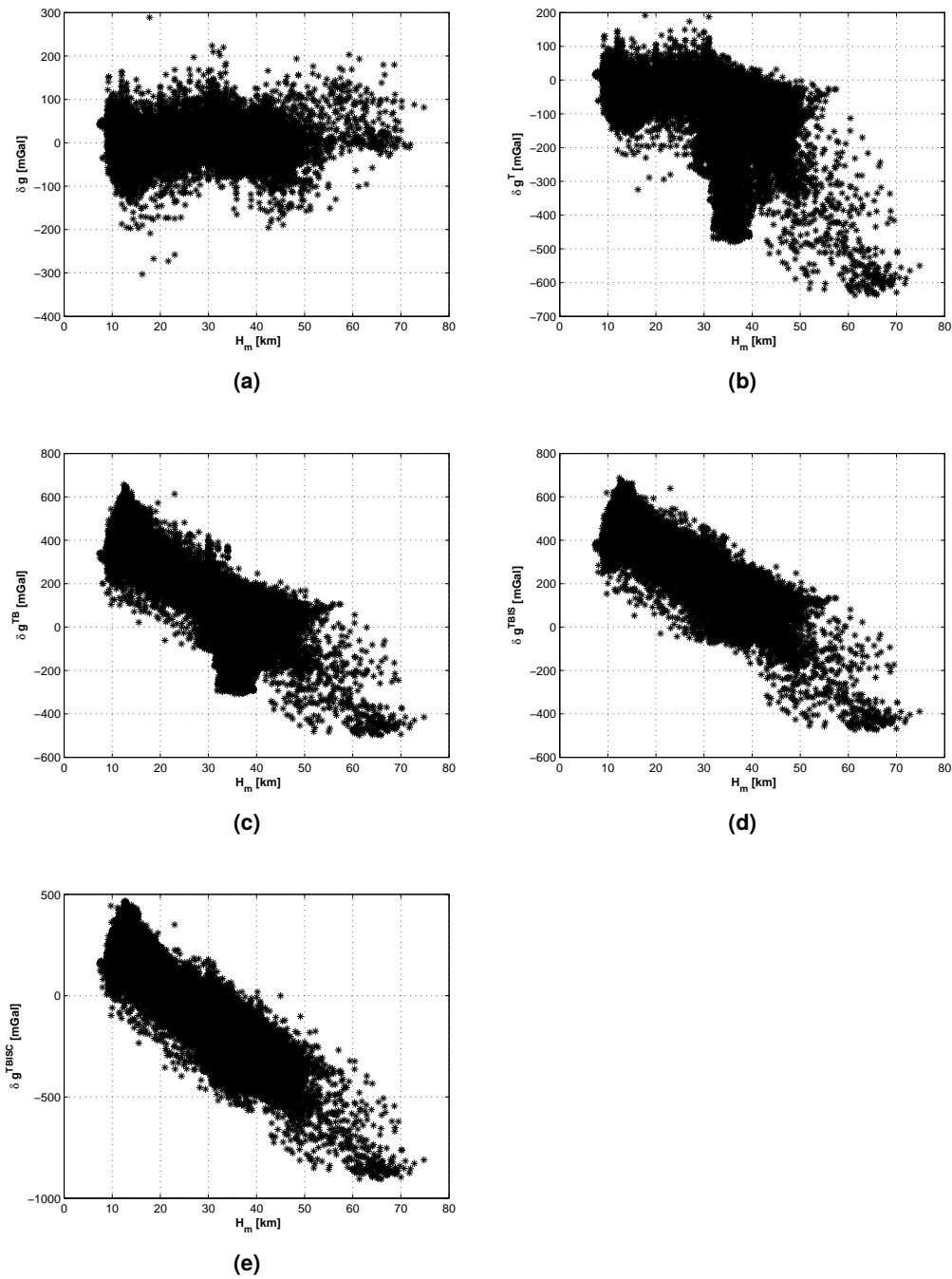


**Figure 5.4** The relation between the Moho depth  $H_m$  and sequentially corrected gravity disturbances: (a) observed  $\delta g$ , (b) topography corrected  $\delta g^T$ , (c) topography and bathymetry corrected  $\delta g^{TB}$ , (d) topography, bathymetry, ice, and sediment corrected  $\delta g^{TBIS}$ , and (e) topography, bathymetry, ice, sediment and consolidated crust corrected  $\delta g^{TBISC}$ .

**Table 5.3** Pearson's correlation of the sequentially corrected gravity field quantities with the Moho depth  $H_m$  from CRUST 1.0.

Type	Gravity disturbances	Gravity anomalies
Earth	-0.01	0.03
Topography corrected	-0.54	-0.45
Topography and bathymetry (TB) corrected	-0.89	-0.72
Topography, bathymetry, ice and sediment corrected (TBIS)	-0.91	-0.74
Topography, bathymetry, ice, sediment and crust corrected (TBISC)	-0.95	-0.88

## 5.5 Estimation of the Moho density contrast

We estimated the Moho density contrast in two different ways: using the crust-stripped gravity disturbances, and using the crust-stripped gravity anomalies. The Moho depth  $H_m$  from CRUST 1.0 model has been exploited. We use an empirical technique in which the absolute correlation between the Moho depth from CRUST 1.0 model and the updated consolidated crust stripped gravity disturbances ( $\delta g_{\text{updated}}$ ) or gravity anomalies ( $\Delta g_{\text{updated}}$ ) is minimized. The updated stripped gravity disturbances and anomalies are obtained by adding a contribution (attraction) related to the density contrast between the reference crust and the upper most mantle to stripped gravity disturbances and anomalies. Mathematically, the updated gravity disturbance ( $\delta g_{\text{updated}}$ ) is given by:

$$\delta g_{\text{updated}} = \delta g^{\text{TBISC}} + \frac{\Delta \rho_m}{2670} \cdot g_{2.67c}, \quad (5.2)$$

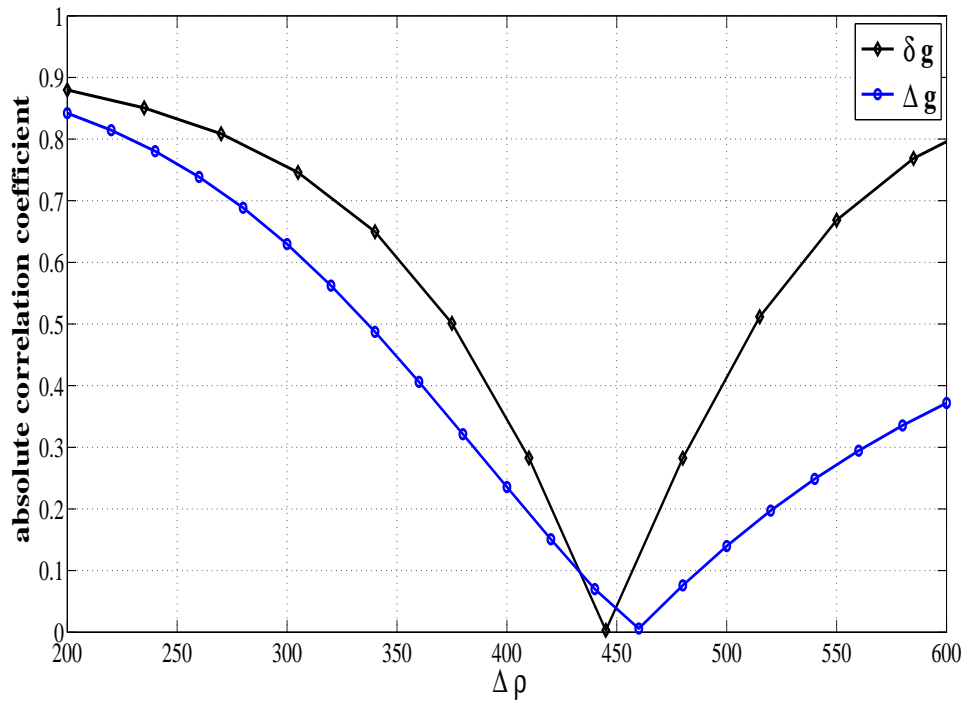
where  $\Delta \rho_m$  is the Moho density contrast in  $\text{kg/m}^3$  and  $g_{2.67c}$  is the gravitational attraction generated by a crust having the reference density of  $2670 \text{ kg/m}^3$  and bounded by the ellipsoid and the Moho interface from CRUST 1.0. The first term on the right hand side of Eq. (5.2) corresponds to the gravity disturbances generated by

the homogeneous crust of density  $2670 \text{ kg/m}^3$  and the other term is the crust-mantle density contrast contribution. The term  $\delta g_{\text{updated}}$  (gravity disturbances) represents the crust replaced by a material of the mantle density.

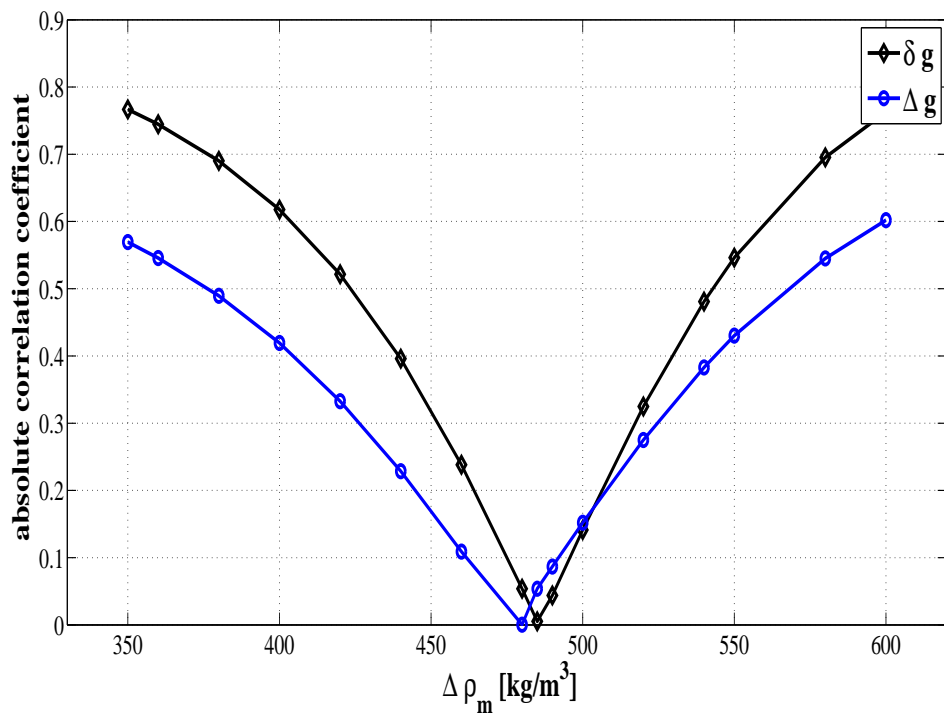
Figure 5.5a shows the plot of absolute correlation between Moho depth  $H_m$  and updated gravity disturbances ( $\delta g_{\text{updated}}$ ) and gravity anomalies ( $\Delta g_{\text{updated}}$ ), as functions of Moho density contrast. This figure is based on the results generated by using the CRUST 1.0 model for gravity stripping correction, and Moho depths for correlation were taken from CRUST 1.0. We have estimated the values of the Moho density contrast corresponding to the lowest correlation coefficients as  $445 \text{ kg/m}^3$  and  $460 \text{ kg/m}^3$ , in case of gravity disturbances and anomalies, respectively. The difference in these two values are due to the removal of indirect effect on the compensation attraction, when using gravity anomalies. The adopted reference crustal density and the estimated values of the Moho density contrast yield the values of  $3115 \text{ kg/m}^3$  and  $3130 \text{ kg/m}^3$  for the global average density of the upper-most mantle based on gravity disturbances and anomalies, respectively. Figure 5.5b is the plot of absolute correlation with Moho depth with our earlier study based on CRUST 2.0 model. In that study CRUST 2.0 were used for stripping corrections, as well as for defining the Moho geometry for the correlation. The values of the Moho density contrast (based on CRUST 2.0 Model) corresponding to the lowest correlation coefficient are  $485 \text{ kg/m}^3$  and  $481 \text{ kg/m}^3$  for gravity disturbances and anomalies, respectively.

These estimated value based on CRUST 2.0 are very similar to the theoretical value of  $480 \text{ kg/m}^3$  adopted in the definition of PREM. These values of the crust-mantle density contrast differ by about 7% from the global average of the Moho density contrast of  $448 \text{ kg/m}^3$  estimated by [Sjöberg \(2011a\)](#). The value of  $445 \text{ kg/m}^3$  based on CRUST 1.0 model and gravity disturbances agrees with the value reported by [Sjöberg \(2011a\)](#). We have used this value when solving the inverse problem for the Moho geometry (Chapters 6-7).

It is observed that the density contrast for gravity anomalies, when using CRUST 2.0, is smaller than for gravity disturbances, but for CRUST 1.0 is the opposite. The only possible explanation for this change is a higher accuracy of CRUST 1.0 model as compared to CRUST 2.0.



(a)



(b)

**Figure 5.5** The absolute Pearson's correlation between the updated crust stripped gravity data and the Moho depths for different values of the Moho density contrast. Diamonds represent gravity disturbances and circles gravity anomalies (a) using CRUST 1.0 Model (b) using CRUST 2.0

## 5.6 Summary

We have computed and applied the topographic and crust-stripping corrections to observed gravity data. The step-wise corrected gravity data have been used for the analysis of the correlation with the crust thickness. We have demonstrated that the crust-stripped gravity disturbances have the largest correlation with the crust thickness as compared to other sequentially corrected gravity disturbances and anomalies. We have demonstrated that the application of stripped correction to gravity disturbances and gravity anomalies improves its correlation with the Moho geometry. It confirmed that the gravity data is successfully cleaned from nuisance signals related to crust inhomogeneities. Furthermore, we have demonstrated the correlation of gravity disturbances with the Moho is higher than the gravity anomalies. It confirmed the local nature of the link between the density variations and gravity disturbances. Therefore, we concluded that gravity disturbances are the most appropriate type of input data for the recovery of Moho geometry as compared to gravity anomalies.

We have used the crust-stripped gravity data and the CRUST1.0 crust-thickness data to estimate the global average value of the crust-mantle density contrast. This is performed by minimising the correlation between the consolidated crust-stripped gravity data and crust thickness data by adding the crust-mantle density contrast to the original reference crustal density of  $2670 \text{ kg/m}^3$ . Our estimated values are  $445 \text{ kg/m}^3$  and  $460 \text{ kg/m}^3$  for gravity disturbances and anomalies, respectively.

The adopted reference crustal density of  $2,670 \text{ kg/m}^3$  and the estimated values yields the values for the upper mantle density of  $3115 \text{ kg/m}^3$  and  $3130 \text{ kg/m}^3$  for gravity disturbances and gravity anomalies, respectively. First of these values of Moho density contrast has been used as input, when solving the inverse problem for the Moho geometry as discussed in Chapter 6.

---

## Recovery of the Moho geometry as an inverse problem

In this chapter, we formulate the functional model for the Moho geometry recovery. This model is established by linking the spherical harmonic coefficients of residual input gravity data (gravity disturbances) with the Moho undulations. The preparation of input gravity data (spherical harmonics coefficients) is presented. Furthermore, we describe the solution strategy for the most probable model of Moho depths using the least-squares estimation method. We discuss the regularisation issue and derive the expressions for the elements of the regularisation matrix. Moreover, we present a combined approach for Moho recovery in which the Moho models from seismic sources are used as an additional input. Subsequently, the estimation of proper weights for each individual data set is discussed. For this purpose, we have used Variance Components Estimation (VCE) procedure.

We used the input data in the form of spherical harmonic coefficients. The motivation to use the input data in the form of spherical harmonic coefficients is a need to suppress the gravity signal due to the deep Earth structure, i.e., the signal due to the core-mantle boundary and heterogeneity of the mantle as well as the impact of the difference between the normal gravity field and its approximation adopted in Eq. (6.6). For this purpose, we have removed the low-degree coefficients from the data vector, and have applied tailored weights to the remaining coefficients.

## 6.1 Residual gravity data as input for the computation of the Moho geometry

In our study, the residual input data are defined as the difference between the observations (observed gravity disturbances ) and the reference gravity disturbances:

$$g_{res} = g - g_0, \quad (6.1)$$

where  $g$  = observations,  $g_0$  = reference gravity and  $g_{res}$  is the residual gravity.

We can further write  $g_0$  as the sum of reference gravity generated by crust ( $g_c$ ), generated by mantle ( $g_m$ ) and centrifugal acceleration ( $Z$ ) of the Earth i.e.,

$$g_0 = g_c + g_m + Z. \quad (6.2)$$

To take into account inhomogeneities in the crust, we further split the crust contribution to gravity into two parts:

1. The part  $g_{2.67c}$  generated by standard crust having nominal density of 2670 kg/m<sup>3</sup>, and
2. The residual part  $\Delta g_{rs}$  generated by the residual density  $\delta\rho$ ,

where  $\delta\rho = \rho_a - \rho_{2.67c}$ , and  $\rho_a$  and  $\rho_{2.67c}$  are the actual crust density taken from a model and nominal crust density, respectively:

$$g_c = g_{2.67c} + \Delta g_{rs}. \quad (6.3)$$

Now from Eq. (6.2) and (6.3) we can write

$$g_0 = \Delta g_{rs} + g_{2.67c} + g_m + Z \quad (6.4)$$

Let us introduce a parameter  $\beta$  (relative density contrast) as,

$$\beta = \frac{\Delta\rho}{\rho_{2.67c}} = \frac{\rho_m}{\rho_{2.67c}} - 1,$$



where  $\rho_m$  is the mantle density, and  $\Delta\rho = \rho_m - \rho_{2.67c}$ , is the crust-mantle density contrast.

Now, we can add and subtract the term  $\beta g_{2.67c}$  from Eq. (6.4):

$$\begin{aligned} g_0 &= \Delta g_{rs} + g_{2.67c} + \beta g_{2.67c} - \beta g_{2.67c} + g_m + Z \\ &= \Delta g_{rs} + (1 + \beta)g_{2.67c} - \beta g_{2.67c} + g_m + Z, \end{aligned} \quad (6.5)$$

The value  $\gamma = (1 + \beta)g_{2.67c} + g_m + Z$ , which can be interpreted as an approximation of the normal field. It is the gravitational attraction of the Earth, whose crust density is replaced by mantle density. Therefore, Eq. (6.5) turns into

$$g_0 = \gamma + \Delta g_{rs} - \beta g_{2.67c}. \quad (6.6)$$

By inserting the value of  $g_0$  from Eq (6.6) into Eq. (6.1), we get

$$g - g_0 = g - \gamma - \Delta g_{rs} + \beta g_{2.67c} \quad (6.7)$$

Now, in view of the definition of gravity disturbance  $\delta g = g - \gamma$ , Eq. (6.7) is further reduced to

$$g_{res} = \delta g - \Delta g_{rs} + \beta g_{2.67c} \quad (6.8)$$

or

$$g_{res} = \delta g - (\Delta g_{rs} - \beta g_{2.67c}) = \delta g - \delta g_r, \quad (6.9)$$

where  $\delta g_r = \Delta g_{rs} - \beta g_{2.67c}$ ,  $\Delta g_{rs}$  is the sum of gravitational attraction (stripping corrections) of the residual part of the crust having residual density  $\delta\rho$ . and  $\beta$  is parameter which is estimated from the values of crust-mantle density contrast  $\Delta\rho$  and nominal crust density. The term  $\Delta g_{rs}$  are described in Eq. (4.6). In the next section, we have described the procedure for the computation of spherical harmonic coefficients of residual gravity disturbances ( $\delta g_r$ ). To get the spherical harmonic coefficients of input gravity disturbances, we subtracted the spherical

harmonic coefficients of residual gravity disturbances from that of observed gravity disturbances. By doing so, we have used the spherical harmonic coefficients of observed gravity disturbances without further processing, and hence minimized the processing error.

## 6.2 Computation of spherical harmonic coefficients of gravity disturbance (residual part $\delta g_r$ )

For the preparation of input data for the Moho recovery, we first compute the spherical harmonic coefficients of residual gravity disturbances  $\delta g_r$  (see Eq. (6.9)) and then the estimated spherical harmonic coefficients are subtracted from the spherical harmonic coefficients of observed gravity disturbance (according to Eq. (6.9)). The later ones are obtained from the EIGEN-6C2 model after subtracting the coefficients of normal field (for  $l$  even and  $m=0$ ).

The residual gravity disturbances and corresponding spherical harmonic coefficients are linked by Eq. (6.10). That expression can be written as follow:

$$Ax = d \quad (6.10)$$

where  $x = [\bar{C}_{0,0}, \bar{C}_{1,0}, \dots, \bar{C}_{LL}, \bar{S}_{1,1}, \bar{S}_{1,2}, \dots, \bar{S}_{LL}]^T$  is the unknown vector composed of spherical harmonic coefficients,  $d = [\delta g_1, \delta g_2, \dots, \delta g_J]^T$  is the observation vector composed of residual gravity disturbances computed on the Earth surface, and  $A$  is the design matrix.

The unknown spherical harmonics coefficients are found as the least-square solution of Eq. (6.10).

## 6.3 Linear Model for Moho configuration recovery

The updated Moho model  $z(\theta, \lambda)$  can be written as

$$z(\theta, \lambda) = z_0(\theta, \lambda) + \sum_{ij} b_{ij} \Psi_{ij}(\theta, \lambda), \quad (6.11)$$

where  $\theta$  is the co-latitude,  $\lambda$  is the longitude,  $i$  and  $j$  are the indices of the node at which the Moho are estimated. The indices  $i$  and  $j$  are taken along the latitudinal direction and the longitudinal direction, respectively.  $z$  is the updated Moho depth to be found,  $z_0$  is the input Moho depth taken from the reference model (CRUST 1.0),  $b_{ij}$  is the unknown Moho correction at node  $ij$ , and  $\Psi_{ij}$  is the basis function given by,

$$\Psi_{ij}(\theta, \lambda) = \begin{cases} \left(1 - \frac{|\theta - \theta_i|}{\Delta\theta}\right) \left(1 - \frac{|\lambda - \lambda_j|}{\Delta\lambda}\right) & \text{if } |\theta - \theta_i| < \Delta\theta \text{ and } |\lambda - \lambda_j| < \Delta\lambda \\ 0 & \text{otherwise,} \end{cases}$$

where  $\Delta\theta$  and  $\Delta\lambda$  are cell sizes in the latitudinal and longitudinal direction, respectively. The function  $\Psi_{ij}$  is equal to 1 at node  $ij$  and reaches zero at the outer border of the cells adjacent to the node  $ij$ .

Let the surface density  $s$  i.e., the mass per unit area, be defined as

$$s = \rho b,$$

where  $\rho$  is mass density (mass per unit volume) and  $b$  is the height of the volume element.

The expression for surface density variation  $\delta s_{ij}$  associated with variation of the Moho depth at the node  $ij$  is subsequently given by

$$\delta s_{ij}(\theta, \lambda) = \Delta\rho \Psi_{ij}(\theta, \lambda) \cdot b_{ij}, \quad (6.12)$$

where  $\Delta\rho$  is the density contrast at the Moho boundary, which is estimated in Chapter 5.

The variation of the spherical harmonic coefficients  $\delta C_{lm}$  of the Earth's gravity disturbances associated with the variation of surface density  $\delta s$  on the surface of a sphere is given by (described in Appendix B):

$$\delta \bar{C}_{lm,ij} = \frac{\bar{R}^2}{M(2l+1)} \left(\frac{\bar{R}}{R}\right)^l \iint_{\Omega} \delta s(\theta', \lambda') \bar{Y}_{lm}(\theta', \lambda') d\Omega'. \quad (6.13)$$

where  $R$  is the radius of a mean sphere, which approximate the Earth, and  $\tilde{R} = R - z_0$ ,  $z_0$  is the reference Moho depth taken from the reference model (CRUST 1.0), and  $d\Omega'$  is an element of the unit sphere  $\Omega'$ .

In view of the value of  $\delta s$  from Eq. (6.12), Eq. (6.13) turns into

$$\delta\tilde{C}_{lm} = \frac{\tilde{R}_{ij}^2}{M(2l+1)} \left(\frac{\tilde{R}}{R}\right)^l \iint_{\Omega} \Delta\rho b \bar{Y}_{lm}(\theta', \lambda') d\Omega'$$

By taking discrete of integration domain, and neglecting the Moho undulation at the vicinity of node  $ij$ , the variations of spherical harmonic coefficients becomes:

$$\delta\tilde{C}_{lm,ij} = \sum_{ij} \frac{\tilde{R}_{ij}^2}{M(2l+1)} \left(\frac{\tilde{R}_{ij}}{R}\right)^l \Delta\rho \cdot b_{ij} \iint_{\Omega} \Psi_{ij}(\theta', \lambda') \bar{Y}_{lm}(\theta', \lambda') d\Omega'. \quad (6.14)$$

Eq. (6.14) represents a linear problem which links the variation of spherical harmonic coefficients of gravity disturbances  $\delta C_{lm}$  (observations) with the Moho undulations  $b_{ij}$  (unknown parameters). An element of the design matrix  $A$  for this linear inverse problem can be obtained as:

$$A_{lm,ij} = \frac{\partial(\delta\tilde{C}_{lm,ij})}{\partial b_{ij}} = \sum_{ij} \frac{\tilde{R}_{ij}^2}{M(2l+1)} \left(\frac{\tilde{R}_{ij}}{R}\right)^l \Delta\rho \iint_{\Omega} \Psi_{ij}(\theta', \lambda') \bar{Y}_{lm}(\theta', \lambda') d\Omega'. \quad (6.15)$$

## 6.4 Least-squares estimation

The unknown Moho model parameters  $b_{ij}$  are arranged as a vector  $x$  of length  $u$ . The residual spherical harmonic coefficients are arranged as an observation vector  $d$  of length  $n$ . Then Eq. (6.14) can be written in matrix-vector notation

$$Ax = d, \quad (6.16)$$

where  $A$  is the  $n \times u$  design matrix.

The final model is obtained by the addition of the reference model to the computed model corrections.

The data to be inverted contain noise. If it is random Gaussian and having the zero mean, then the functional model of Moho corrections from gravity data Eq. (6.16) may be interpreted as a standard Gauss-Markov model:

$$E\{d\} = Ax, \quad D\{d\} = C_d,$$

where  $E$  and  $D$  denote the expectation and the dispersion operator, respectively, and  $C_d$  is the variance-covariance matrix of data noise.

In the absence of a prior information, the weighted least-square solution is obtained by minimizing the quadratic function

$$\phi(x) = (d - Ax)^T C_d^{-1} (d - Ax), \quad (6.17)$$

which is equivalent to solving the system of normal equations:

$$\hat{x} = N^{-1}(A^T C_d^{-1} d), \quad (6.18)$$

where  $N$  is the normal matrix:

$$N = A^T C_d^{-1} A. \quad (6.19)$$

Eq. (6.18) provides the statistically optimum solution in the presence of noise in the data.

Multiple data sets,  $d_1, d_2, d_3, \dots, d_n$  can be combined to form a single set of observation equations

$$A_i x = d_i, \quad i = 1, n \quad (6.20)$$

In the absence of correlation between noise in different data sets, its least-squares solution can be written as:

$$\hat{x} = \tilde{N}^{-1} y, \quad (6.21)$$

where

$$\tilde{N} = \sum_{i=1}^n A_i^T C_{d_i}^{-1} A_i$$

and

$$\mathbf{y} = \sum_{i=1}^n \mathbf{A}_i^T \mathbf{C}_{d_i}^{-1} \mathbf{d}_i$$

where  $\mathbf{C}_{d_1}, \mathbf{C}_{d_2}, \mathbf{C}_{d_3}, \dots, \mathbf{C}_{d_n}$  are the covariance matrices of noise in the data sets  $\mathbf{d}_1, \mathbf{d}_2, \mathbf{d}_3, \dots, \mathbf{d}_n$ , respectively.

## 6.5 Regularization

Available data frequently do not allow model parameters to be determined accurately. In this case, an additional a priori information has to be used. A way to formulate and exploit the existing knowledge about the a priori information and the model is offered by statistical regularization, assuming that according to a priori information, the most probable model is equal to  $\mathbf{x}_0$ . Let the model satisfy the Gaussian distribution and is characterized by the most probable model  $\mathbf{x}_0$ , and the covariance matrix  $\mathbf{C}_x$ :

$$E\{\mathbf{x}\} = \mathbf{x}_0, \quad D\{\mathbf{x}\} = \mathbf{C}_x,$$

Then the a priori probability density function (pdf) of the model is :

$$P(\mathbf{x}) \propto e^{-\frac{1}{2}(\mathbf{x}-\mathbf{x}_0)^T \mathbf{C}_x^{-1}(\mathbf{x}-\mathbf{x}_0)}.$$

Furthermore, assuming that the noise is Gaussian and has zero mean i.e.,

$$E\{\mathbf{n}\} = 0, \quad D\{\mathbf{n}\} = \mathbf{C}_d,$$

where  $\mathbf{C}_d$  is the covariance matrix of data noise. Similarly, the data vector  $\mathbf{d}$  can be treated as random with stochastic properties

$$E\{\mathbf{d}\} = \mathbf{A}\mathbf{x}, \quad D\{\mathbf{d}\} = \mathbf{C}_d.$$

Then, the a-posteriori pdf of the model can be determined as:

$$P(\mathbf{x}|\mathbf{d}) \propto e^{-\frac{1}{2}(\mathbf{d}-\mathbf{A}\mathbf{x})^T \mathbf{C}_d^{-1}(\mathbf{d}-\mathbf{A}\mathbf{x}) - \frac{1}{2}(\mathbf{x}-\mathbf{x}_0)^T \mathbf{C}_x^{-1}(\mathbf{x}-\mathbf{x}_0)}. \quad (6.22)$$

Let us denote the optimal model estimation  $\hat{x}$  as the most probable model for which the a posteriori pdf (Eq. 6.22) is maximum. Then, such a model can be found as the minimum of a quadratic objective function (Ditmar, 2010):

$$\hat{x} = \operatorname{argmin}_x \left[ (Ax - d)^T C_d^{-1} (Ax - d) + (x - x_0)^T C_x^{-1} (x - x_0) \right]. \quad (6.23)$$

Differentiating Eq. (6.23) with respect to elements of the vector  $x$  and assigning the result to zero yields:

$$\hat{x} = \left( A^T C_d^{-1} A + C_x^{-1} \right)^{-1} \left( A^T C_d^{-1} d + C_x^{-1} x_0 \right) \quad (6.24)$$

Let

$$C_d^{-1} = \frac{1}{\sigma_d^2} P_d, \quad (6.25)$$

where  $P_d$  is the data weight matrix, whereas,  $\sigma_d^2$  is data noise variance. A similar representation of the model covariance matrix can be introduced:

$$C_x^{-1} = \frac{1}{\sigma_x^2} P_x. \quad (6.26)$$

By inserting the expression for  $C_d^{-1}$  and  $C_x^{-1}$  given by Eqs. (6.25) and (6.26) into Eq. (6.24), we obtain:

$$\hat{x} = \left( A^T P_d A + \alpha P_x \right)^{-1} \left( A^T P_d d + \alpha P_x x_0 \right),$$

where  $\alpha = \frac{\sigma_d^2}{\sigma_x^2}$  is the regularization parameter. For initial model correction  $x_0 = 0$ , the above Eq. becomes

$$\hat{x} = \left( A^T P_d A + \alpha P_x \right)^{-1} A^T P_d d. \quad (6.27)$$

Eq. (6.27) is an alternative form of the regularized least-squares adjustment formula, which yields the minimum of the corresponding objective function:

$$\hat{x} = \operatorname{argmin}_x (Ax - d)^T P_d (Ax - d) + \alpha x^T P_x x. \quad (6.28)$$

Knowledge of covariance matrices of the data noise and a priori model uncer-

tainties is mandatory when statistical regularization is used. In the most cases, the former is not a problem, while the latter is less obvious because we need to define some properties of a phenomenon that might be totally unknown before the measurements are made. For this reason, the statistical regularization is frequently replaced in practice with the Tikhonov regularization (Tikhonov, 1963a,b).

Originally, the Tikhonov regularization concept was developed for continuous inverse problems, however it can also be applied to discrete problems. According to Tikhonov, the objective function (6.28) is replaced with the following one:

$$\hat{x} = \underset{x}{\operatorname{argmin}} (Ax - d)^T P_d (Ax - d) + \alpha \phi(x), \quad (6.29)$$

where  $\phi(x)$  is a regularization functional. If the vector  $x$  is represented by a one-dimensional function  $f(t)$ , then the Tikhonov regularization functional can be written as:

$$\phi(x) = \int_a^b \left[ \zeta_0(t) f^2(t) + \zeta_1(t) \left( \frac{df(t)}{dt} \right)^2 + \dots + \zeta_n(t) \left( \frac{d^{(n)}f(t)}{dt^{(n)}} \right)^2 \right] dt, \quad (6.30)$$

where  $\zeta_0(t), \zeta_1(t) \dots \zeta_n(t)$  are a priori non-negative functions. The maximum order  $n$  of derivative of function  $f(t)$  is called the order of regularization.

Now, the regularized least-squares solution of the inverse problem, for which the objective function of Eq. (6.29) is minimized is given as:

$$\hat{x} = \left( A^T P_d A + \alpha R \right)^{-1} A^T P_d d, \quad (6.31)$$

where  $R$  is the regularization matrix,  $N = (A^T P_d A + \alpha R)$  is the normal matrix and  $y = A^T P_d d$  is the right hand side vector.

By comparing Eqs. (6.27) with (6.31), and using Eq. (6.26), we get

$$C_x = \sigma_x^2 R^{-1}.$$

For more than one data set, Eq. (6.31) can be rewritten as:

$$\hat{x} = N^{-1} y, \quad (6.32)$$



where

$$\mathbf{N} = \sum_{i=1}^n \left( \frac{\mathbf{A}_i^T \mathbf{P}_{d_i} \mathbf{A}_i}{\sigma_{d_i}^2} + \frac{1}{\sigma_x^2} \mathbf{R} \right), \quad (6.33)$$

and

$$\mathbf{y} = \sum_{i=1}^n \frac{\mathbf{A}_i^T \mathbf{P}_{d_i} \mathbf{d}_i}{\sigma_{d_i}^2}, \quad (6.34)$$

where  $n$  is total number of data sets.

## 6.6 Discrete zero-order and first-order Tikhonov regularization

From Eq. (6.30), the zero- and first-order Tikhonov regularization function  $\phi(x)$  can be written for an unknown function on the surface ( $\Omega_{\tilde{R}}$ ) of a sphere as follows:

$$\phi_0(x) = \int \int_{\Omega_{\tilde{R}}} x^2(\theta, \lambda) d\Omega_{\tilde{R}}, \quad (6.35)$$

and

$$\phi_1(x) = \int \int_{\Omega_{\tilde{R}}} (\nabla x(\theta, \lambda))^2 d\Omega_{\tilde{R}}, \quad (6.36)$$

where  $x(\theta, \lambda)$  is the unknown function, i.e., Moho model correction,  $\Omega_{\tilde{R}}$  is the surface of a sphere of radius  $\tilde{R}$ ,  $\theta$  is co-latitude and  $\lambda$  is longitude.

A discrete analogue of Tikhonov zero-order regularization given by Eq. (6.35) is:

$$\phi(x) = \sum_{i,k} x^2(\theta_i, \lambda_k) \tilde{R}^2 \sin \theta_i \Delta \theta \Delta \lambda, \quad (6.37)$$

where  $\Delta \theta$  and  $\Delta \lambda$  are the cell sizes. After denoting  $x_{i,k} = x(\theta_i, \lambda_k)$ , the above equation can be rewritten as

$$\phi(x) = \sum_{i,k} \sum_{i',k'} \mathbf{R}_{iki'k'} x_{i,k} x_{i',k'} = \mathbf{x}^T \mathbf{R} \mathbf{x},$$

where  $\mathbf{R}$  is the regularization matrix whose elements are given by

$$\mathbf{R}_{iki'k'} = \begin{cases} \tilde{R}^2 \sin \theta_i \Delta \theta \Delta \lambda & \text{if } i' = i, k' = k \\ 0 & \text{otherwise} \end{cases}. \quad (6.38)$$

In case of the first-order regularization, discretization of Eq. (6.36) yields:

$$\phi(x) = \sum_{i,k} \left[ \left( \frac{x(\theta_{i+1}, \lambda_k) - x(\theta_i, \lambda_k)}{R \Delta \theta} \right)^2 R^2 \sin \theta_{i+\frac{1}{2}} \Delta \theta \Delta \lambda + \left( \frac{x(\theta_i, \lambda_{k+1}) - x(\theta_i, \lambda_k)}{R \sin \theta_i \Delta \lambda} \right)^2 R^2 \sin \theta_i \Delta \theta \Delta \lambda \right],$$

where the term  $\theta_{i+\frac{1}{2}}$  is the value of co-latitude at the mid-point between the nodes with indices  $i$  and  $i+1$ . By simplifying the above equation, we get

$$\begin{aligned} \phi(x) &= \sum_{i,k} \left[ (x(\theta_{i+1}, \lambda_k) - x(\theta_i, \lambda_k))^2 \sin \theta_{i+\frac{1}{2}} \frac{\Delta \lambda}{\Delta \theta} + (x(\theta_i, \lambda_{k+1}) - x(\theta_i, \lambda_k))^2 \frac{\Delta \theta}{\sin \theta_i \Delta \lambda} \right] \\ &= \sum_{i,k} \left[ (x_{i+1,k} - x_{i,k})^2 \chi_{i+\frac{1}{2}} + (x_{i,k+1} - x_{i,k})^2 \frac{1}{\chi_i} \right], \end{aligned} \quad (6.39)$$

where

$$\begin{aligned} x_{i,k} &= x(\theta_i, \lambda_k) \\ \chi_i &= \frac{\sin \theta_i \Delta \lambda}{\Delta \theta} \end{aligned}$$

Eq. (6.39) further transforms into:

$$\begin{aligned} \phi(x) &= \sum_{i,k} \left[ \left( x_{i+1,k}^2 - 2x_{i+1,k} \cdot x_{i,k} + x_{i,k}^2 \right) \chi_{i+\frac{1}{2}} + \left( x_{i,k+1}^2 - 2x_{i,k+1} \cdot x_{i,k} + x_{i,k}^2 \right) \frac{1}{\chi_i} \right] \\ &= \sum_{i,k} x_{i+1,k}^2 \chi_{i+\frac{1}{2}} + \sum_{i,k} x_{i,k}^2 \chi_{i+\frac{1}{2}} + \sum_{i,k} x_{i,k+1}^2 \frac{1}{\chi_i} + \sum_{i,k} x_{i,k}^2 \frac{1}{\chi_i} - \\ &\quad 2 \sum_{i,k} x_{i+1,k} \cdot x_{i,k} \chi_{i+\frac{1}{2}} - 2 \sum_{i,k} x_{i,k+1} \cdot x_{i,k} \frac{1}{\chi_i} \\ &= \sum_{i,k} x_{i,k}^2 \chi_{i-\frac{1}{2}} + \sum_{i,k} x_{i,k}^2 \chi_{i+\frac{1}{2}} + \sum_{i,k} x_{i,k}^2 \frac{1}{\chi_i} + \sum_{i,k} x_{i,k}^2 \frac{1}{\chi_i} - \\ &\quad 2 \sum_{i,k} x_{i+1,k} \cdot x_{i,k} \chi_{i+\frac{1}{2}} - 2 \sum_{i,k} x_{i,k+1} \cdot x_{i,k} \frac{1}{\chi_i} \end{aligned} \quad (6.40)$$

$$= \sum_{i,k} x_{i,k}^2 \cdot \nu_i - 2 \sum_{i,k} x_{i+1,k} \cdot x_{i,k} \chi_{i+\frac{1}{2}} - 2 \sum_{i,k} x_{i,k+1} \cdot x_{i,k} \frac{1}{\chi_i}, \quad (6.41)$$

where

$$v_i = \chi_{i-\frac{1}{2}} + \chi_{i+\frac{1}{2}} + \frac{2}{\chi_i}.$$

After rearranging the indices  $i$  and  $k$ , Eq. (6.41) further reduces to:

$$\begin{aligned} \phi(x) &= \sum_{i,k} x_{i,k}^2 \cdot v_i - \sum_{i,k} x_{i+1,k} \cdot x_{i,k} \chi_{i+\frac{1}{2}} - \sum_{i,k} x_{i,k} \cdot x_{i-1,k} \chi_{i-\frac{1}{2}} - \\ &\quad \sum_{i,k} x_{i,k+1} \cdot x_{i,k} \frac{1}{\chi_i} - \sum_{i,k} x_{i,k} \cdot x_{i,k-1} \frac{1}{\chi_i} \end{aligned} \quad (6.42)$$

$$= \sum_{i,k} \sum_{i',k'} R_{iki'k'} x_{ik} \cdot x_{i'k'} = \mathbf{x}^T \mathbf{R} \mathbf{x}, \quad (6.43)$$

where

$$R_{iki'k'} = \begin{cases} v_i & \text{if } i' = i, k' = k \\ -\chi_{i+\frac{1}{2}} & \text{if } i' = i+1, k' = k \\ -\chi_{i-\frac{1}{2}} & \text{if } i' = i-1, k' = k \\ -\frac{1}{\chi_i} & \text{if } i' = i, k' = k-1 \text{ or } i' = i, k' = k+1 \\ 0 & \text{otherwise} \end{cases} \quad (6.44)$$

is the regularization matrix. In this study, Eq. (6.38) and (6.44) are used for the computation of the regularization matrix when the zero-order and first-order regularization is applied.

## 6.7 Solution strategy

To estimate the Moho depths, we discretize the whole globe into a  $2 \times 2$  arc-degree cells. It results in 16200 unknown parameters, called Moho corrections. The input data are defined as a set of spherical harmonic coefficients up to maximum degree and order  $L$ . Three cases for the maximum degree and order of input data have been considered:  $L = 90$ ,  $L = 150$ , and  $L = 180$ . The total number of coefficients (observations) in these cases is equal to 8281, 22801 and 32761, respectively. The maximum degree does not exceed 180 in order to match the resolution of the CRUST 1.0 model, which has been used for the forward modelling of gravity data (stripping corrections). We have used the following procedure for solving the inverse problem.

- Compute the elements of the design matrix  $A$ , as described in Eq. (6.15), using numerical integration.
- Compute the elements of the regularization matrix  $R$ , using Eqs. (6.38) and (6.44) in case of the zero-order and first-order regularization, respectively.
- Compute the regularization parameter using the Variance Components Estimation (VCE) procedure.
- Compute the normal matrix  $N$  as described in Eq. (6.33) and the right-hand side vector  $y$  of Eq. (6.34), and then solve the system of linear equations described by Eq. (6.32).

The Variance Components Estimation (VCE) technique (described in Appendix C) is used to estimate the regularization parameter and data weights. The weights are estimated by using the iteration solution and minimising the root means square value of the difference of two consecutive solutions.

## 6.8 Summary

In this chapter, we have described the functional model for the Moho configuration recovery. The model is established by linking the spherical harmonic coefficients of residual gravity disturbances with the Moho undulations. We present a procedure for the preparation of input data to be used for the Moho recovery. Furthermore, the least-squares estimation procedure for finding the most probable model (unknown Moho corrections) is described. We present the zero and first-order Tikhonov regularisation schemes and derive the expressions for the computation of the elements of zero and first-order Tikhonov regularization matrix. Moreover, we present a combined approach for Moho recovery in which the Moho models from seismic data are used as an additional input. Subsequently, the estimation of proper weights for each individual data set is presented. To that end, we have used the Variance Components Estimation (VCE) procedure.

---

## The Moho model and its validation

In this chapter, we present Moho model which have been developed using advanced numerical schemes for forward and inverse modeling. It has been argued in Chapter 2, that the large scale features can not be recovered from gravity data due to signals related to mantle inhomogeneity and core-mantle boundary. The pure gravimetric inversion may leads to an ill-posed problem due to a lack of uniqueness. Therefore, we have used gravity disturbances data together with a priori models based on seismic data. For this purpose, the global models CRUST 1.0, and CRUST07 have been used as a priori models. Moreover, we have used zero-order and first-order regularization. We have estimated the weight for each individual data set, using the Variance Components Estimation (VCE) procedure. To damp the nuisance signal related to mantle and core-mantle boundary heterogeneities, we have eliminated the first few degree of input spherical harmonic coefficients. Additionally, we have apply degree-dependent weight to the input spherical harmonic coefficients. In Section 7.1, we discuss the procedure for selecting the optimal values of the parameters required for Moho inversion. These parameters include input data combination schemes, choice of regularisation, degree up to which the input spherical harmonic coefficients are eliminated, degree-dependent weights, and the maximum degree of the input spherical harmonic coefficients.

Furthermore, we have produced three variants of Moho model using the above optimal combination strategy, by truncating the maximum degree of spherical harmonic coefficients at: (1) degree 90, (2) degree 150, and (3) degree 180. Then, we compare these three variants of Moho models with the European Moho model EuM09. We named our optimal Moho model as “Delft Moho Model Release 1”

(DMM-1). In Section 7.2, we have re-estimated the Moho density contrast using the DMM-1 model and stripped gravity disturbances. In Section 7.3, we present the analysis of our final product DMM-1, by comparing it with the available global Moho models. In Section 7.4, we present the comparison of Moho model DMM-1 with two regional models. These regional models include (1) the Gravity Derive Moho for South America (GDMSA) (Van der Meijde et al., 2013), (2) and (2) Precambrian Crustal Structure in Africa and Arabia (PCSAA) (Tugume et al., 2013). Finally, the summary is presented in Section 7.5.

## 7.1 Optimal data processing strategy

During the course of this research, we have adopted the following data processing strategies, which can be classified on the basis of combining gravity disturbances data with a-priori models, and the choice of the regularization scheme:

1. Moho Model using gravity data with a priori model CRUST 1.0 and Zero-order regularization (MMC1Z)
2. Moho Model using gravity data with a priori model CRUST 1.0 and First-order regularization (MMC1F)
3. Moho Model using gravity data with a priori model CRUST07 and Zero-order regularization (MMC07Z)
4. Moho Model using gravity data with a priori model CRUST07 and First-order regularization (MMC07F)
5. Moho Model using gravity data with a priori models CRUST 1.0, CRUST07 and Zero-order regularization (MMJZ)
6. Moho Model using gravity data with a priori models CRUST 1.0, CRUST07 and First-order regularization (MMJF)

The gravity disturbances data used in the development of these models are based on EIGEN-6C2 model, with the CRUST 1.0 stripped corrections applied. We have taken the contribution of gravity data up to maximum degree  $L = 180$ , in order to match the  $1^0 \times 1^0$  resolution of CRUST 1.0 model. The other reason to limit the maximum degree  $L$  to 180, is to minimize the signal due to the uncertainties of crust model,

which may contribute at higher degrees. The long wavelength component of the gravity data contain nuisance signals due to the 3-D density distribution within the mantle and core-mantle boundary. For this reason we eliminate first few degrees of the spherical harmonic coefficients of the input gravity data; up to degree 5, second, up to degree 10, and third, up to degree 15. For the further suppression of deep inhomogeneities, we have applied low weights to low-degree coefficients and high weights to high-degree coefficients.

### 7.1.1 Optimal data combination and the choice of regularisation

For the selection of the best data combination strategy, the optimal set of eliminated low-degree spherical harmonic coefficients, and the optimal degree-dependent weights of spherical harmonic coefficients, we have compared our models with two regional models for the European Moho: EuM09 developed by [Grad et al. \(2009\)](#) and EuCrust07 developed by [Magdala et al. \(2008\)](#). The EuCrust07 model spans the latitudes range  $35^{\circ}\text{N} - 71^{\circ}\text{N}$ , and the longitudes range  $25^{\circ}\text{W} - 35^{\circ}\text{E}$ , whereas the EuM09 model covers the region between the latitudes  $28^{\circ}\text{N}$  and  $87^{\circ}\text{N}$ , and the longitudes between  $40^{\circ}\text{W}$  and  $70^{\circ}\text{E}$ . For analysis, we have split the European region into two parts: (1) the continental part (2) the oceanic part. We have chosen these models due to the fact the Moho for European crust is well known as compared to other parts of the globe, and due to their high resolutions and the compilation of currently available seismic and gravity maps.

In order to choose the best seismic model and gravity data combination, we have run the inversion of various data combinations along with the zero-order and first-order regularization. We have eliminated the contribution of low-degree spherical harmonic coefficients up to 5, 10, and 15 degree. In this experiment, we have taken the input gravity spherical harmonic coefficients up to maximum degree 180. As highlighted in the last column of Tables [7.1](#) and [7.2](#), the RMS differences for the MMJF strategy are minimum with both of European Moho models EuM09 and Eucrust07. From these results, we can conclude that the optimum strategy is to utilize the gravity data in combination with both global a priori models CRUST 1.0 and CRUST07 and with the first-order regularization. Tables [7.1](#) and [7.2](#), present the Root Mean Square (RMS) difference between our models as well as CRUST 1.0 and CRUST07 on the other hand and the EuM09 and EuCrust07 Moho models on

**Table 7.1** Comparison of our different strategy based Moho models with EuM09 model, RMS difference in [km].

**(a)** Elimination of low-degree  $l \leq 5$  contribution

$l \leq 5$	CRUST 1.0	CRUST07	MMC1Z	MMC1F	MMC07Z	MMC07F	MMJZ	MMJF
continental part	2.95	4.73	2.65	2.83	3.83	3.83	2.57	2.49
oceanic part	3.48	3.09	3.25	3.43	2.98	2.96	2.74	2.88
total	3.13	4.47	2.93	3.13	3.78	3.25	2.80	2.71

**(b)** Elimination of low-degree  $l \leq 10$  contribution

$l \leq 10$	CRUST 1.0	CRUST07	MMC1Z	MMC1F	MMC07Z	MMC07F	MMJZ	MMJF
continental part	2.95	4.73	2.62	2.74	3.61	3.19	2.54	2.29
oceanic part	3.48	3.09	2.96	3.29	2.23	2.10	2.61	2.55
total	3.13	4.47	2.88	3.01	3.44	2.93	2.57	2.48

**(c)** Elimination of low-degree  $l \leq 15$  contribution

$l \leq 15$	CRUST 1.0	CRUST07	MMC1Z	MMC1F	MMC07Z	MMC07F	MMJZ	MMJF
continental part	2.95	4.73	2.65	2.84	3.75	3.33	2.57	2.52
oceanic part	3.48	3.09	3.12	3.38	2.40	2.14	2.74	2.85
total	3.13	4.47	2.91	3.09	3.59	3.04	2.79	2.74



the other hand. Based on this comparison, we have found that the strategy MMJF which incorporates the combination of gravity data with CRUST 1.0 and CRUST07 models, using first-order regularization scheme, yields the best result.

### 7.1.2 Spherical harmonic coefficients low-degree contribution

The choice to eliminate low degrees is based on the RMS fit between the developed models and the existing regional models for the European Moho EuM09 and Eucrust07. We run the inversions for the Moho recovery, using the following spherical harmonics coefficients of the input gravity data:

- of degree  $l > 5$
- of degree  $l > 10$
- of degree  $l > 15$

We compare our models with EuM09 and Eucrust07 models, and the results are summarised in Tables 7.1 and 7.2, respectively. From Tables 7.2b and 7.1b, it can be noted that the minimum RMS difference is achieved when the contribution of those input spherical harmonic coefficients is eliminated which have degree  $\leq 10$ . As shown in the Tables 7.1 and 7.2, we have obtained the minimum RMS difference for all three regions in this way.

From the above results we conclude that the elimination of spherical harmonic coefficients up to degree 10 provide the best RMS fit of gravimetric solutions with high-resolution European Moho models. This is due to the fact that gravitational signals of mantle density heterogeneities are more or less contained within the long wavelength up to degree  $l \leq 10$ . For further analysis, we have used the strategy MMJF, and have taken contribution of input spherical harmonic coefficients degree  $l > 10$ .

### 7.1.3 Degree dependent weights of gravity data

To damp the signal from deep inhomogeneities we have adopted a strategy, in which lower degrees are given lesser weights, whereas the higher degrees are given higher weights. For this purpose, we have performed numerical experiments, in which we

**Table 7.2** Comparison of our different strategy based Moho models with Eucrust07 model, RMS differences in [km].

**(a)** Elimination of low-degree  $l \leq 5$  contribution

$l \leq 5$	CRUST 1.0	CRUST07	MMC1Z	MMC1F	MMC07Z	MMC07F	MMJZ	MMJF
continental part	4.12	6.36	3.88	3.91	5.89	5.15	4.03	3.88
oceanic part	4.42	3.40	3.94	4.13	4.34	3.89	3.38	3.63
total	4.165	5.84	3.90	3.92	5.01	4.74	3.91	3.72

**(b)** Elimination of low-degree  $l \leq 10$  contribution

$l \leq 10$	CRUST 1.0	CRUST07	MMC1Z	MMC1F	MMC07Z	MMC07F	MMJZ	MMJF
continental part	4.12	6.36	3.82	3.77	5.50	4.70	3.86	3.71
oceanic part	4.42	3.40	3.78	4.09	4.72	3.64	3.21	3.59
total	4.165	5.84	3.84	3.90	5.01	4.34	3.78	3.62

**(c)** Elimination of low-degree  $l \leq 15$  contribution

$l \leq 15$	CRUST 1.0	CRUST07	MMC1Z	MMC1F	MMC07Z	MMC07F	MMJZ	MMJF
continental part	4.12	6.36	3.87	3.78	5.67	4.96	3.99	3.84
oceanic part	4.42	3.40	3.95	4.09	4.13	4.04	3.86	3.75
total	4.165	5.84	3.84	3.90	5.01	4.34	3.91	3.81

**Table 7.3** RMS differences [in km] between EuM09 and MMJF based strategy Moho model for different weights to spherical harmonics coefficients.

RMS difference [km]	1	$l^2$	$l^4$	$l^6$
Continental region	3.17	2.84	2.29	2.62
Oceanic region	2.99	2.99	2.55	3.16
Combine region	3.10	2.96	2.48	2.90

have obtained the Moho models using different weights proportional to the spherical harmonic coefficients degree (degree-dependent weights). We apply the following weighting schemes:

- $\mathbf{P}_d \propto l^2$
- $\mathbf{P}_d \propto l^4$
- $\mathbf{P}_d \propto l^6$

where  $\mathbf{P}_d$  is the weights matrix of the input gravity data and  $l$  is the spherical harmonic degree. Using the above weighting scheme, we have produced the Moho model using the MMJF strategy and by using the spherical harmonic coefficients up to degree 180 of input gravity data. The quantitative values in table 7.3, represent the RMS difference between our proposed Moho model and the high-resolution EuM09 Moho model, with the above-mentioned weighting schemes. The results reveal that the best RMS fit (see Table 7.3) can be achieved by applying weights proportional to  $l^4$ . This implies that the application of weights proportional to  $l^4$  properly suppress the long wavelength part of gravity signals and amplify the signals from shallow structures.

#### 7.1.4 Maximum degree truncation

We further produce three variants of MMJF strategy by setting the maximum degree of input spherical harmonic expansion equal to (1) 90, (2) 150, and (3) 180. There is the following reasons for the elimination of coefficients above degree 180: (1) The

**Table 7.4** RMS difference [in km] between EuM09 and MMJF based strategy Moho model for different maximum-degree  $L$  truncations.

$L=90$	$L=150$	$L=180$
2.82	2.56	2.48

resolution of the CRUST 1.0 model, which is used for the stripping correction of gravity data is  $1^0 \times 1^0$ , which is equivalent to degree 180. (2) The coefficients above degree 180 are strongly contaminated by the signals of upper crust heterogeneities. (3) the computation of Moho for taking maximum degree  $L > 180$  would be time consuming and will required large computational time and machine memory. We have compared our results with the EuM09 Moho model for the European region. The RMS fit is provided in Table 7.4. The RMS fit between the EuM09 model and our Moho models improves by increasing the maximum degree  $L$ , yielding the minimum RMS difference for  $L = 180$ . The results indicate that the Moho signature is still present at high degrees up to 180, despite the contribution of the crust model uncertainties, which may be significant at high degrees (typically above degree 100). We named our optimal Moho model as “Delft Moho Model Release 1” (DMM-1). The conclusion is that, the DMM-1 is obtain by using the input gravity data with a priori models CRUST 1.0 and CRUST07, eliminating coefficients up to degree 10, applying degree-dependent weight to input coefficients, and taking maximum degree input coefficients up to  $L=180$ . For further analysis and comparison we have used this model.

## 7.2 Moho density contrast estimation from MMJF model

In Chapter 5, we have estimated crust-mantle density contrast using complete crust-stripped gravity disturbances and the Moho depth from the a priori CRUST 1.0 model. Now, we recompute the crust-mantle density contrast using the stripped gravity disturbances and the Moho depth from DMM-1 model. For the estimate, we followed the same procedure as in Chapter 5. From this study, we have estimated the value of  $454 \text{ kg/m}^3$  for crust-mantle density contrast. This value differs from our early estimate ( $445 \text{ kg/m}^3$ ) by only 2%.

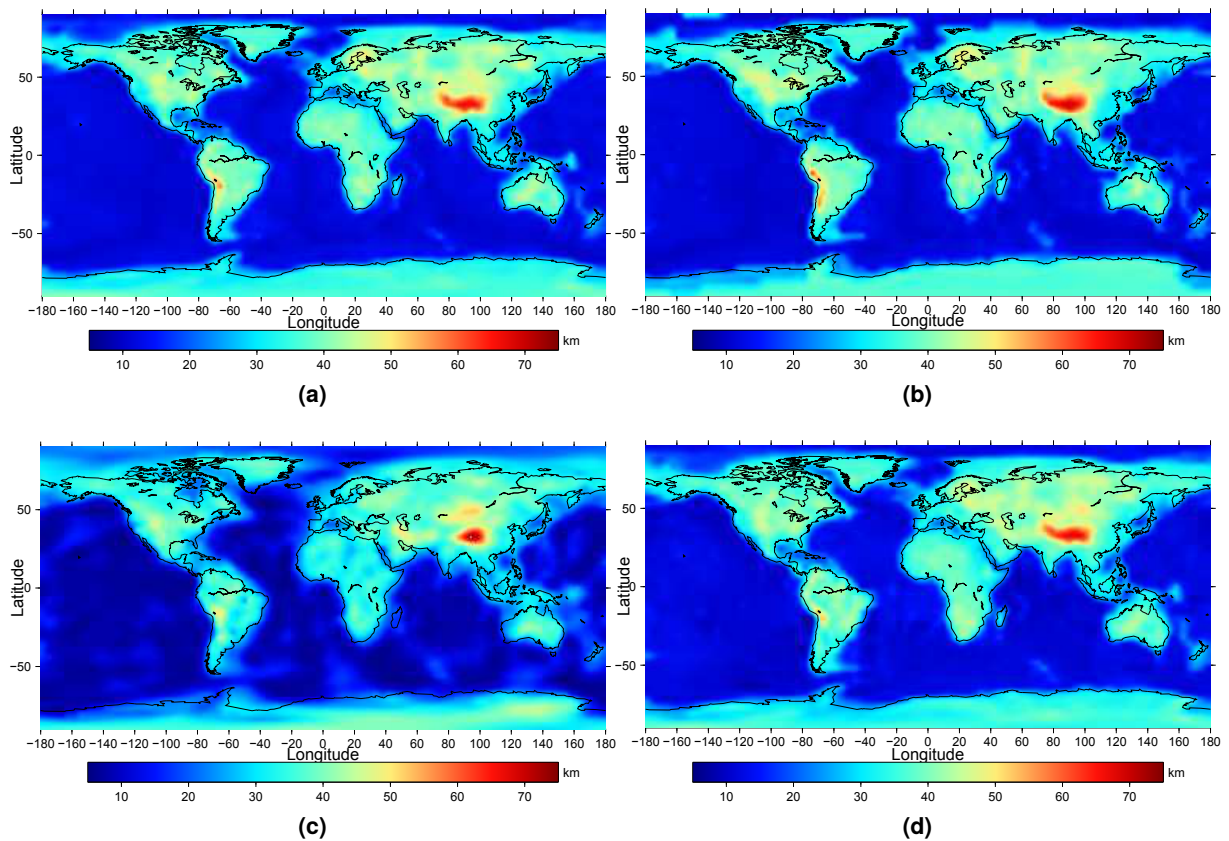


**Figure 7.1** Global Moho maps from (a) CRUST 1.0, (b) CRUST 2.0, (c) CRUST07, and (d) DMM-1 models

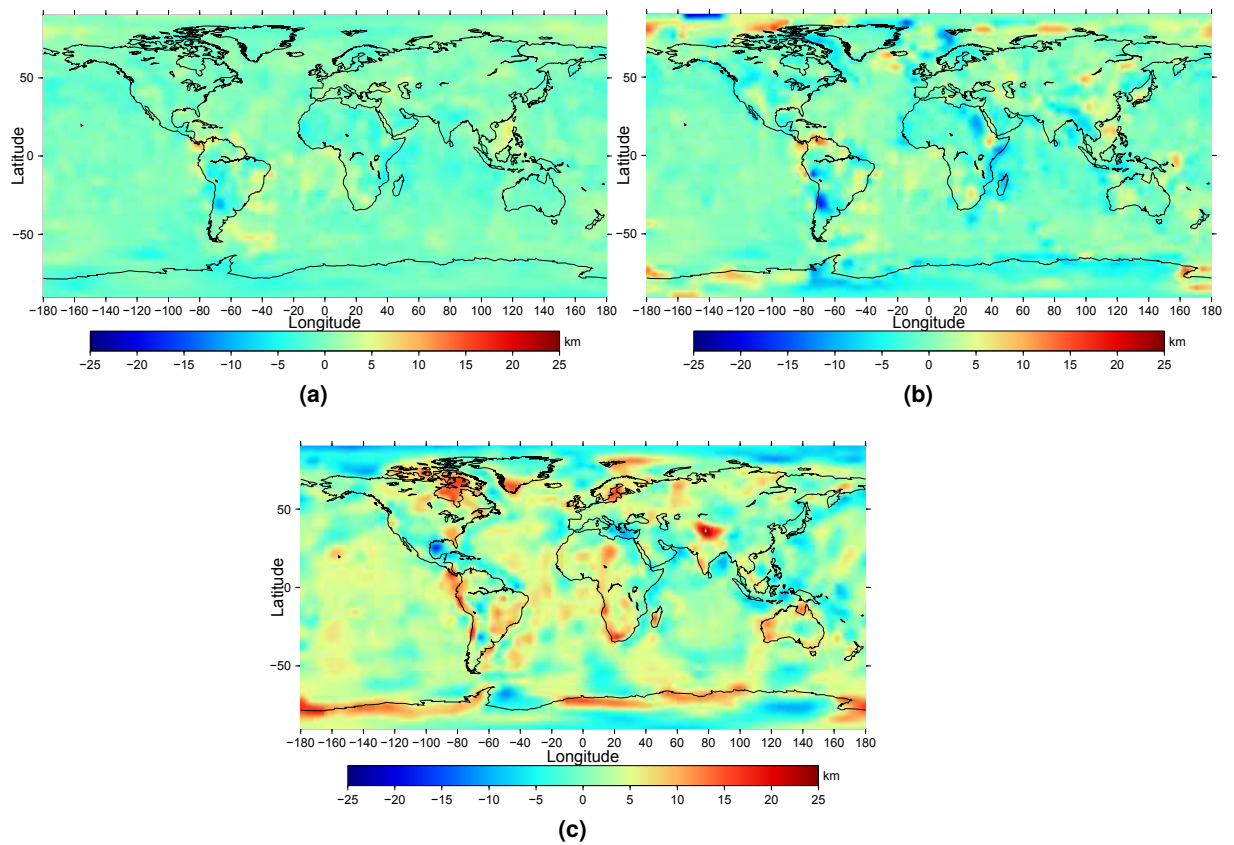


**Figure 7.2** Difference between DMM-1 and (a) CRUST 1.0, (b) CRUST 2.0, and (c) CRUST07

**Table 7.5** Statistics of different Moho models, unit [km].

Model	Min	Max	Mean	STD
MMJF	6.1	70.2	22.83	12.1
CRUST 2.0	8.6	69.9	22.96	12.3
CRUST 1.0	7.4	74.0	22.90	12.04
CRUST07	5.9	75.97	20.78	11.87

**Table 7.6** Statistics of the differences between a DMM-1 on the one hand and CRUST 2.0, CRUST 1.0 and CRUST07 models on the other hand, [km].

Model	RMS	Min	Max	STD
CRUST 2.0	3.25	-25.2	21.9	3.9
CRUST 1.0	1.66	-8.6	9.5	1.83
CRUST07	5.03	-20.3	33.5	5.14

### 7.3 Analysis of the obtain Moho model and comparison with alternative global models

The best data processing strategy comprises eliminating the spherical harmonic coefficients up to degree 10, applying degree-dependent weights proportional to  $l^4$ , and truncating degree 180 above spherical harmonic coefficients of the input gravity data. In our analysis we have considered three global Moho models: CRUST 2.0, CRUST 1.0 and CRUST07, shown in Figure 7.1. The statistics of these models are given in Table 7.5. We compare our Moho model DMM-1 with these global models. The RMS differences between the above-mentioned three global models, and our models are summarized in Table 7.6. The global maps of Moho models are depicted in Figure 7.1, while the differences are shown in Figure 7.2. The differences between DMM-1 model and the CRUST 1.0 is minimum. One possible explanation for it is that we have used the data from CRUST 1.0 in the forward-modeling of crust inhomogeneities, while the other explanation is that the CRUST 1.0 is used as

a-priori model and VCE assigns a higher weight to it as compared to the CRUST07 model (The VCE weights assigned to a priori models CRUST 1.0 are one order of magnitude greater than that assigned to CRUST07 model). On the other hand, in some parts of the globe we can observe a significant difference between our model and CRUST 1.0. These parts include the Himalaya region, Africa, South America, India, and Antarctica.

Figures 7.1a, 7.1b, and 7.1d show a typical pattern of the crustal structure. The most pronounced feature a steep transition from a thin oceanic crust to a thick continental crust along the marginal seas. The maximum crustal thickness is under the orogens of the Andes, Himalaya with an extension till the Tibetan Plateau. These structures correspond to the continent-to-continent and oceanic-to-continent collision. The contrast between the thin continental crust of the Tarim sedimentary basin relative to the surrounding orogens (Atlay, Hindu Kush, and Tibet) is well-pronounced to the north of Tibet. Towards the east of Tibet, the sedimentary basin of Sichuan is well-pronounced, similar to Indo-Gangetic basin to the south of Himalaya. Ural orogen is seen in Figures 7.1a, 7.1b, and 7.1d.

We observe also a thick continental crust in Fennoscandia, which is explained by glacial load and consequently crustal flexure, which is not rebalanced into original position (glacial rebound). This is not observed however in the Hudson Bay area. In North America, the crustal thickness is controlled mainly by the geological composition. For the oceanic crust, the largest crustal thickness is found under Island. It correspond to location of hotspot.

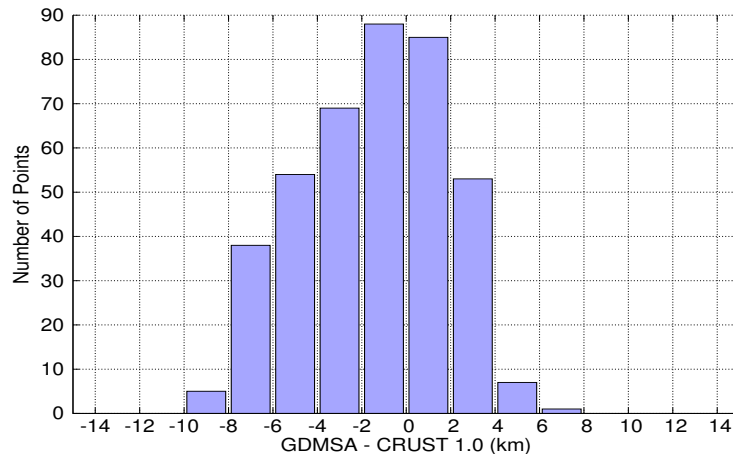
## 7.4 Regional comparison

As mentioned earlier, we compare our Moho model with two regional models, one for the South America (GDMSA) and the other for the Africa (PCSAA).

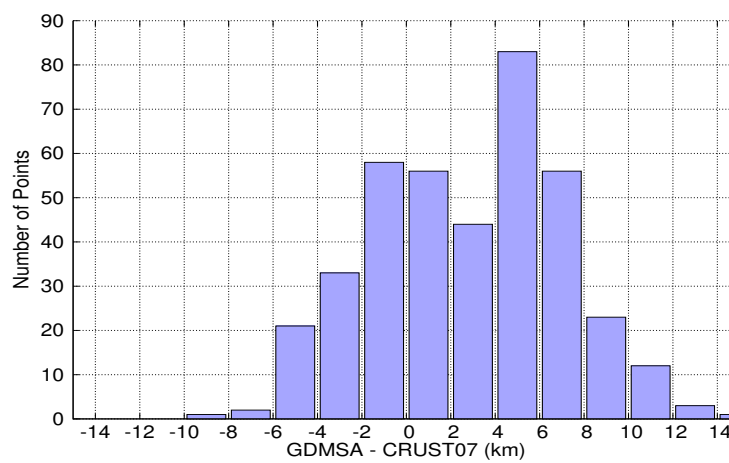
### 7.4.1 Moho model for South America (GDMSA)

The DMM-1 model fits the GDMSA as compared to the other models. Our model has predicted the small scale as well as the large scale features of the Moho, and are similar to those in the GDMSA model. All three models show the Orogenic

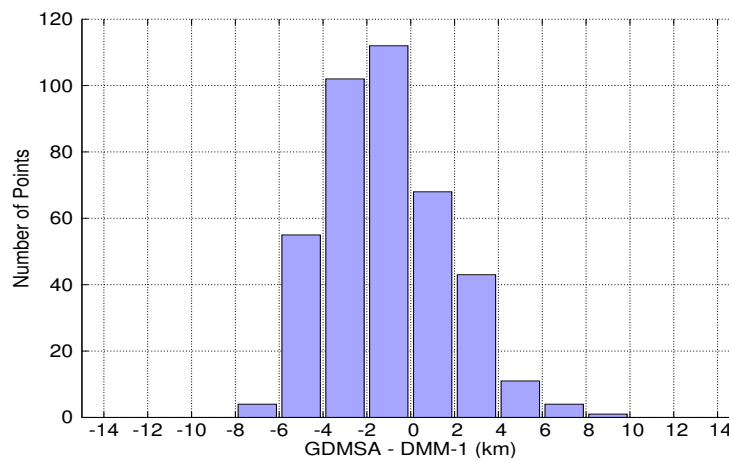




(a) a



(b) b



(c) c

**Figure 7.3** Histograms of differences between the GDMSA and (a) CRUST 1.0 (b) CRUST07 (c) DMM-1

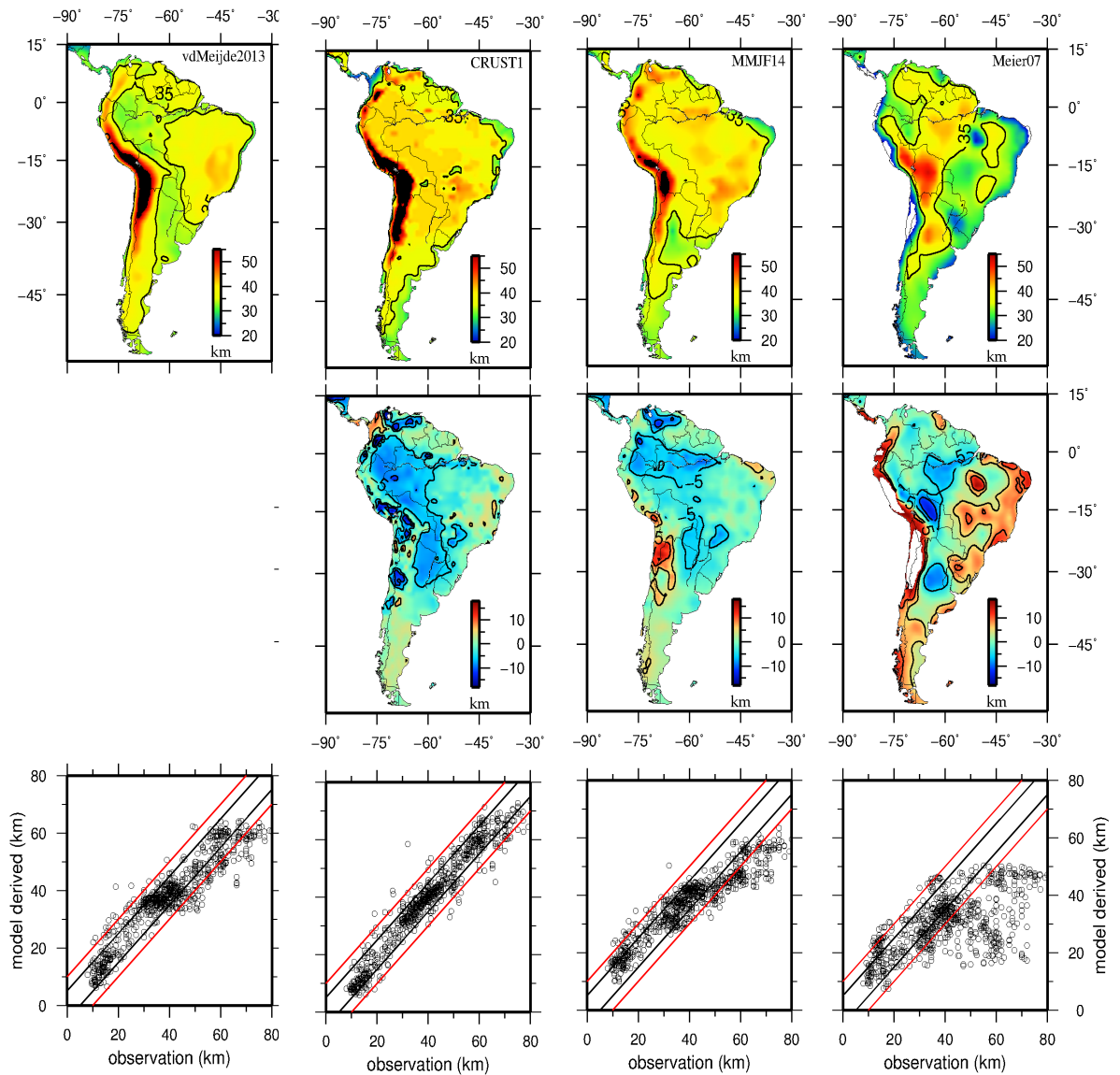


**Figure 7.4** Top: different Moho models, middle: difference with GDSMA, bottom: observation v.s. derive model. From left to right GDSMA, CRUST 1.0, DMM-1, and CRUST07

**Table 7.7** Statistics for the Moho models over the South America.

Model	Min	Max	Mean	STD
GDMSA	23.4	56.5	35.8	4.2
CRUST 1.0	23.3	55.7	37.3	4.8
CRUST07	18.4	48.6	32.8	5.11
DMM-1	24.1	52.5	37.1	4.0

**Table 7.8** RMS differences over the South America, between GDMSA Model on the one hand, and CRUST 2.0, CRUST 1.0 and DMM-1 models on the other hand

	CRUST 2.0	CRUST 1.0	CRUST07	DMM-1
RMS [km]	4.2	3.9	5.6	3.3

formation of Andes very well, as a result of the ocean-to-continent collision zone of Nazca and South American tectonic plates, characterized by largest crustal thickness especially in central Andes (see Figure 7.4). The DMM-1 model (Figure 7.4) shows clearly the continental sedimentary basin to the East of Andes. The contours of this sedimentary basin are well-recognized by low crustal thickness relative to large thickness under orogenic belt of Andes (to the west) and in the Amazon craton (to the east). This sedimentary basin can not be clearly seen in the other two models. All three models show clearly the extended crust structure (characterized by the thin crust) in the most part of Argentina. Moreover, cratonic formation with thicker crust can be witnessed in south Brazil, Uruguay and Paraguay (i.e., contrast between extended crust and craton).

The RMS differences over the South America region between Moho geometries based on various global models and GDMSA Moho model are described in Table 7.8. Different Moho maps for the region are presented in Figure 7.4 (top of the Figure). The difference between GDMSA Moho and other models is shown in Figure

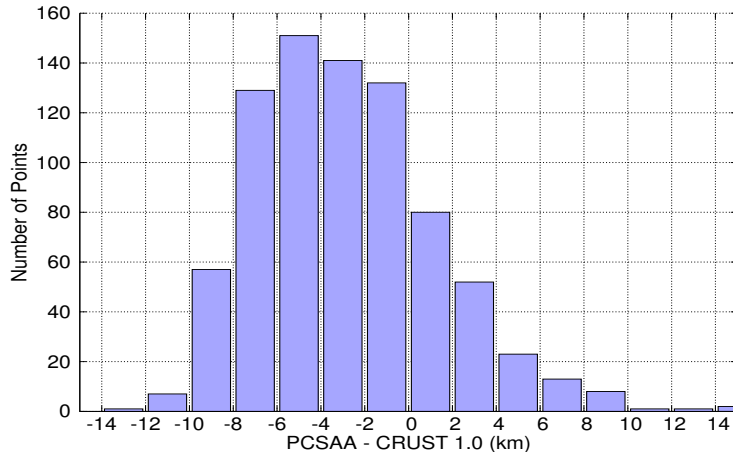
**Table 7.9** RMS[km] differences between CTMAF Moho model with others Moho models for Africa.

	CRUST 2.0	CRUST 1.0	CRUST07	DMM-1
RMS [km]	4.35	4.8	5.02	3.95

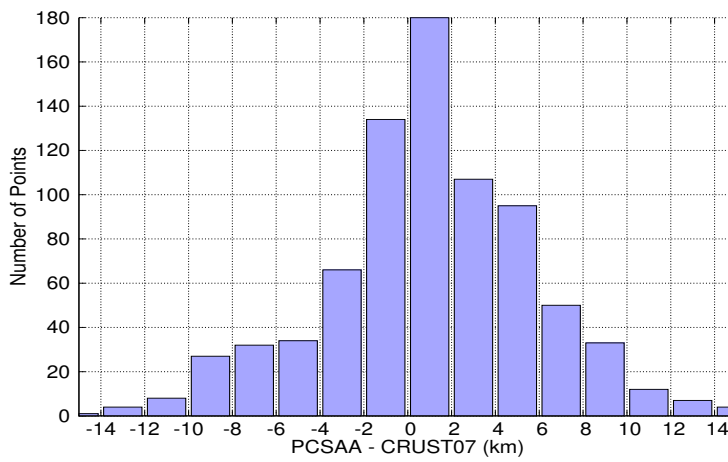
**Table 7.10** Statics for the Moho models of the Africa.

Model	Min	Max	Mean	STD
PCSAA	18.5	43.6	33.6	3.2
CRUST 1.0	18.7	44.8	36.4	4.5
CRUST07	16.1	50.5	32.5	5.2
DMM-1	18.9	46.2	35.8	4.5

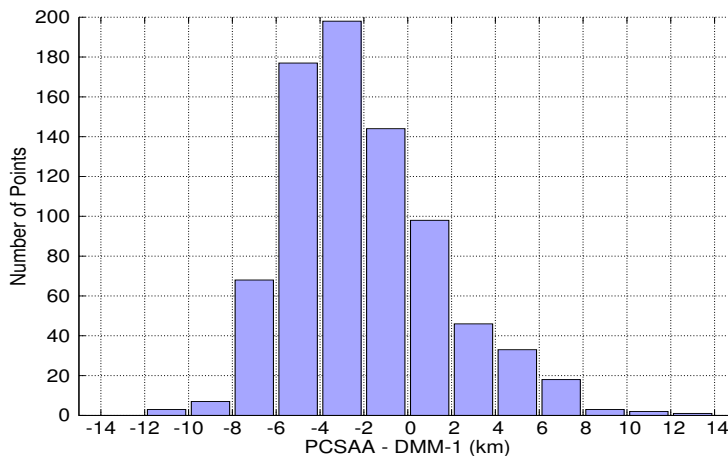
7.4 (middle of the Figure). The plot of the observed point values and the value for GDMSA, CRUST 1.0, DMM-1 and CRUST07 are shown in the Figure 7.4 (bottom of the Figure). The observed point values are provide by [Van der Meijde et al. \(2013\)](#). The histogram of the differences between the GDMSA and the others models is shown in Figure 7.3. The comparison from the histograms reveal that the DMM-1 has relatively good fit with GDMSA, as compare to CRUST 1.0 and CRUST07. In the histograms shown in Figure 7.3, 92% of the point values of GDMSA has less than 5 km difference with DMM-1 model, whereas these value are 80%, and 61% for the CRUST 1.0 and CRUST07, respectively. In other words only 8% of data point of DMM-1 have difference with GDMSA greater than 5 km and less than 15 km, whereas for CRUST 1.0 and CRUST07 it is 20%, and 39%, respectively. The statistics of different models for the South America are summarized in Table. 7.7.



(a) a



(b) b



(c) c

**Figure 7.5** Histograms of differences between the PCSAA and (a) CRUST 1.0 (b) CRUST07 (c) DMM-1

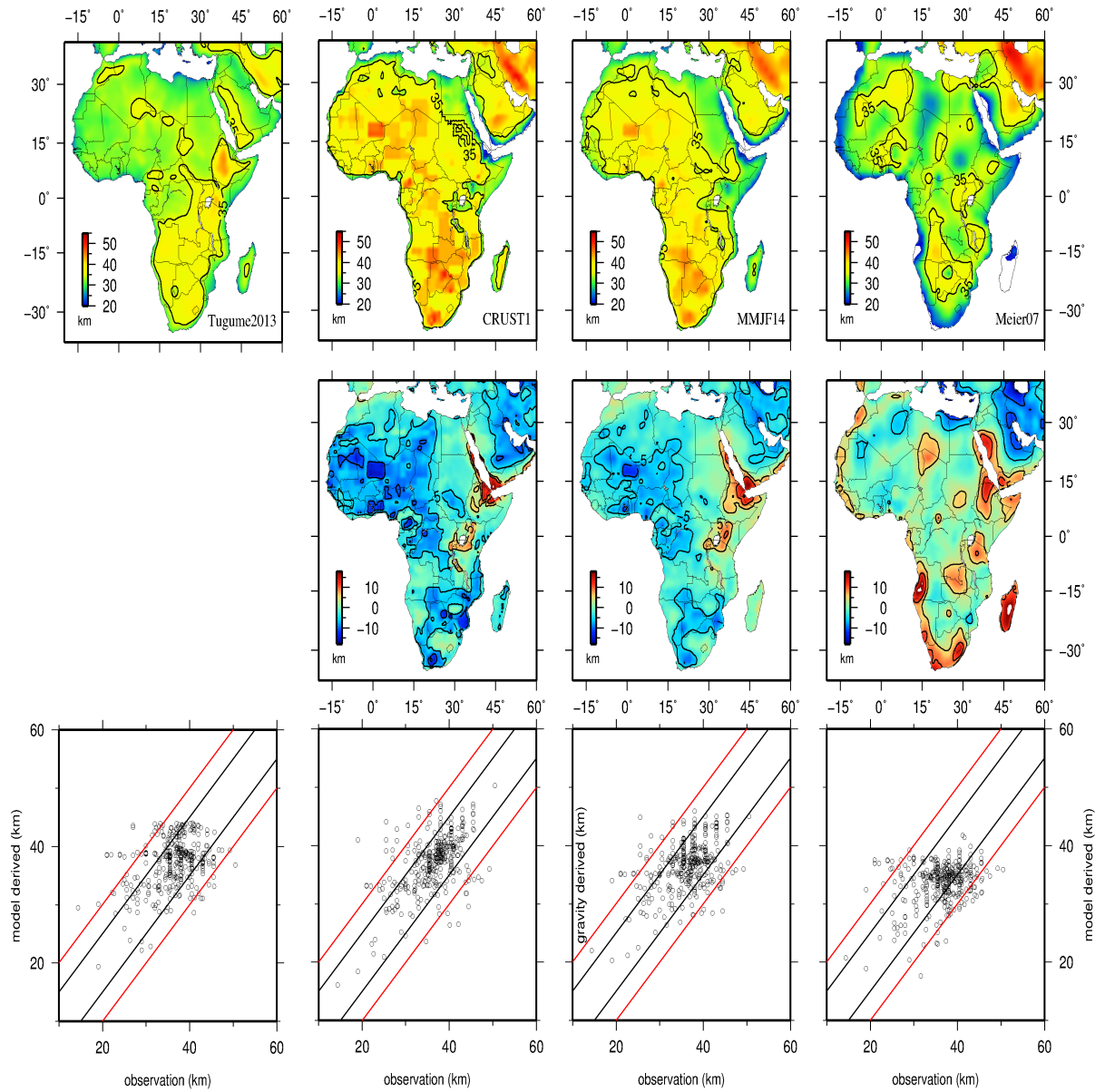


**Figure 7.6** Top: different Moho models, middle: difference with PCSAA, bottom: observation v.s. derive model. From Left to right, PCSAA, CRUST 1.0, DMM-1, and CRUST07.

### 7.4.2 Moho model beneath Africa (PCSAA)

In this section, we compare our Moho model DMM-1 with another regional model called, the Precambrian Crustal Structure in Africa and Arabia (PCSAA) (Tugume et al., 2013). All the three models, PCSAA, DMM-1 and CRUST 1.0 show distinctively thin crustal structure along the East-African rift zone as well as along the continent-to-continent collision zone between Africa and Eurasian tectonic plates (Figures 7.6), . At that place, the old oceanic crust has been captured between these two continental plates and as a result we observe a relatively thin crust. The models show thicker crust under cratonic shield and platform in sub-equatorial Africa and West Africa. The sedimentary basin in west Mali is marked by smaller crustal thickness. Furthermore, the orogenic formation of the Atlas in Morocco is not recognized by the thick continental crust.

The RMS differences between various Moho models over Africa and PCSAA Moho model are described in Table 7.9. The available and developed Moho maps for the region are shown in Figures 7.6 (top of the Figure). The differences between PCSAA Moho model and the other models are shown in Figures 7.6 (middle of the Figure). The plot of the observed point values and the value for GDMSA, CRUST 1.0, DMM-1 and CRUST07 are shown in the Figure 7.6 (bottom of the Figure). The observed point values are taken from the published paper by Tugume et al. (2013). As compared to the other models, our Moho model (DMM-1) is in a good agreement with the PCSAA as well as with the point observed values. The RMS difference for the DMM-1 Moho model is minimum. The histograms of differences between PCSAA model on one hand and CRUST 1.0, CRUST 07 and DMM-1 on the other hand are shown in Figure 7.5. The result reveals that the DMM-1 have the best fit with PCSAA as compared to the others two models. In the histograms shown in Figure 7.5, 77% of the point values of PCSAA has less than 5 km difference with DMM-1 model, whereas these value are 63%, and 70% for the CRUST 1.0 and CRUST07, respectively. In other words only 23% of data point of DMM-1 has difference with PCSAA greater than 5 km and less than 15 km, whereas for CRUST 1.0 and CRUST07 it is 37%, and 30%, respectively. Table. 7.10, summarized the statistics of different models for the Africa.

## 7.5 Summary

In this chapter, we identified the optimal data processing strategy. For this, two models for the European Moho, the EuM09 and Eucrust07 are used for the comparison of different data processing schemes, and selecting the optimal values of the parameters involved. These parameters include input data combination schemes, choice of regularisation, degree up to which the input spherical harmonic coefficients are eliminated, degree-dependent weights, and the maximum degree of the input spherical harmonic coefficients. Based on the RMS fit of the produced estimates to the two models mentioned before, it is found that the best data processing strategy consist of: using gravity data together with the others a priori models based on seismic studies CRUST 1.0 and CRUST 07, using the first-order Tikhonov regularisation, elimination of low-degree coefficients up to  $l = 10$ , using the  $l^4$  degree-dependent data weighting scheme, and exploiting input gravity spherical harmonic coefficients up to degree 180. The model produced with this scheme is called Delft Moho Model release 1 (DMM-1).

Furthermore, we have compared our final Moho model with the available global and regional Moho models. For a global comparison we use the global Moho models CRUST 2.0, CRUST 1.0 and CRUST07. We find that our Moho model is in a good agreement with CRUST 1.0. There are two reason for this agreement, the one is, we have used CRUST 1.0 for the computation of the stripping corrections and the other we have used CRUST 1.0 as a priori model in the solution of inverse problem. Furthermore, for the regional comparison of our final DMM-1 model, we use two independent models, one for the South America (GDMSA) and the other for the Africa (PCSAA). Our produced model DMM-1 has good RMS fit with the two regional models as compare to the other models for the region.

The elimination of spherical harmonic coefficients up to degree 10 give best results in terms of RMS fit of our gravimetric Moho with the regional Moho models. This mathematical procedure largely removes the unmodelled gravitational signal of the mantle heterogeneities. However, it also partially removes the gravitational signals of the Moho geometry. Therefore, our gravimetric model makes use of CRUST 1.0 and CRUST07, which are the only source of information at low degrees.

We have also re-estimated the crust-mantle density contrast using the stripped gravity disturbances and the Moho depth from DMM-1 model. The new value



are slightly differs from our early estimated value, which is based on CRUST 1.0 model.



---

## Summary, conclusions and recommendations

The research presented in this dissertation is aimed at developing advanced procedures for the recovery of global Moho geometry by using state-of-the-art models of Earth's gravity field and the additional geophysical information about various crust layers and the Earth's density structure. In Section 8.1, we summarize the work presented in this dissertation. In Section 8.2, we present the major results of the research. Finally, Section 8.3 provides recommendations for future researches and details remaining open questions.

### 8.1 Summary and conclusions

The main objective of this research is to use state-of-the-art information about the gravity field to improve the estimates of Moho depths globally. We have achieved this goal, using the basic principles of gravimetric Moho modeling; (1) the forward modeling (2) the inverse modeling. Furthermore, our focus was to develop and apply methods for forward modeling of gravity signal related to crust heterogeneities; and finding the global crust-mantle density contrast.

In Chapter 1, we briefly describe the background of research, research objectives, outline of the thesis and the adopted research methodology. The literature overview of activities, and a background study are presented in Chapter 2.

In Chapter 3, we derived an analytical expression for the computation of gravitational potential of a polyhedral body having a constant or a linearly-varying mass density. Furthermore, numerical experiments were performed to investigate the numerical accuracy and efficiency of different methods used for the forward modeling the gravitational potential and attraction due to residual densities of crust layers. Moreover, a particular methodology for the computation of the gravity attraction and the potential is proposed.

The observed gravity disturbances and gravity anomalies contains signals related to topography, bathymetry, ice, sediments and other density inhomogeneities in the crust. In Chapter 4, we have computed the global component-wise stripped gravity disturbances and gravity anomalies. To model the effects of topography, bathymetry, and ice, we have used the global elevation and bathymetry models GTOPO30C and ETOPO1, respectively. Furthermore, we have used the laterally-varying thickness and density estimates from the CRUST 1.0 model for the computation of the residual effects due to ice, sediments, upper, middle, and lower crust inhomogeneities. Furthermore, we have modeled the effect of the masses between the reference ellipsoid and the geoid, and corrected the corresponding gravity disturbances and anomalies. We have computed the Earth gravity disturbances and anomalies using the spherical harmonics coefficients of the recently-published EIGEN-6C2 model. Finally, after applying subsequent corrections, we have generated corrected gravity disturbances and anomalies. These gravity disturbances and anomalies are associated with Earth having a homogenous crust of a reference crust density between the ellipsoid and the Moho interface and the real mantle density below the Moho interface.

In Chapter 5, we have presented some analysis of the sequentially-corrected gravity disturbances and anomalies and estimated the crust-mantle density contrast. For this purpose, we computed the correlation coefficients between the depth of different interfaces and the sequentially corrected gravity disturbances and anomalies. We have demonstrated that the observed gravity is uncorrelated with the topography, bathymetry and Moho interface. It shows that the Earth's crust is isostatically compensated. When we apply the corrections, the correlation of gravity disturbances and anomalies with Moho depth increases. Hence, the corrected gravity data are the most suitable for the estimation of global mean value of crust-mantle density contrast. We have estimated the crust-mantle density contrast from gravity disturbances and anomalies by using an empirical method based on minimizing the correlation between the updated crust stripped gravity data and

the Moho depth. Our estimated values are in complete agreement with the those published in the literature. Moreover, based on the gravity data analysis, we have concluded that gravity disturbances are more suitable input data for the refinement of Moho as compared to gravity anomalies. Furthermore, we demonstrated that the application of stripping corrections to gravity data increase its correlation with Moho geometry.

In Chapter 6, we have presented the linear functional model for recovery of the Moho interface. The functional model links the residual spherical harmonic coefficients of the corrected gravity disturbances to variations in the Moho interface. To separate the signals due to Moho geometry from that of mantle heterogeneities and the deep Earth structure, we have proposed to eliminate low-degree spherical harmonic coefficients of the input data vector. Additionally, we have applied-degree dependent weights to the input spherical harmonic coefficients in such a way that low-degrees coefficients are weighted less than high-degrees coefficients. In this way the gravity signals from deep structures is further suppressed. To constrain the resulting model (particularly at large spatial scale), we have utilized the statistical regularisation and a priori Moho models CRUST 1.0 and CRUST 07. Simultaneously, we have used Variance Components Estimation (VCE) procedure for the estimation of weights to be applied to the data and to the a priori models.

In Chapter 7, we performed some analysis to select the best data processing strategy. For this analysis, we have utilized two European regional Moho models. Based on the RMS fit between these model and the obtained estimates of Moho geometry. We have found that the best strategy consist of using the gravity data together with a priori Moho models (CRUST 1.0 and CRUST 07). We named our optimal Moho model as “Delft Moho Model Release 1” (DMM-1). The conclusion is that, the DMM-1 is obtain by using the input gravity data with a priori models CRUST 1.0 and CRUST07, eliminating coefficients up to degree 10, applying degree-dependent weight to input coefficients, and taking maximum degree input coefficients up to  $L=180$ . We analysed and compare the DMM-1 model with alternative global and regional models. Based on the statistics (Histogram), we have concluded that the DMM-1 has good agreement with the other two independent high resolution regional models as compared to CRUST 1.0 and CRUST07.

## 8.2 Major results

The major results of the conducted research are listed below:

- Derived an analytical expression for the computation of the gravitational potential generated by a polyhedral body with a linearly-varying density.
- Computed sequentially-corrected gravity disturbances and anomalies on  $1^0 \times 1^0$  geographical grid. The corrections for the topography, due to residual density of bathymetry, ice, sediments, upper, middle, and lower crust are applied.
- Computed the global mean value of crust-mantle density contrast from the sequentially-corrected gravity disturbances and gravity anomalies. The estimated values of  $445 \text{ kg/m}^3$  and  $460 \text{ kg/m}^3$  for the gravity disturbances and gravity anomalies, respectively.
- Devised an algorithm for the computation of the Moho depth corrections, using the spherical harmonic coefficients of the corrected gravity disturbances.
- Developed and evaluated a new Moho model based on the optimal selection of the regularization scheme, a priori models, elimination of low-degree spherical harmonic coefficients, and degree-dependent weighting.

## 8.3 Future recommendations

Though we have shown a high quality of the designed model, there is still room for further improvements. A summary of open questions and recommendations for further researches is given below.

- The work presented in this dissertation can be further extended to make an inversion for the Moho configuration and the Moho density contrast simultaneously.
- We have replaced the actual density distribution in the crust with a reference density of  $2670 \text{ kg/m}^3$  and estimated the mean crust-mantle density contrast by minimizing the correlation between corrected gravity disturbances/anomalies and Moho depths. We have used the global mean value for crust-mantle density contrast in the solution of our inverse problem. It is recommended that the

Moho model should be recovered by assuming laterally-varying crust-mantle density contrast between the reference crust of density  $2670 \text{ kg/m}^3$  and the mantle density (from the seismic studies). In the first instance, it will be logical to estimate the mean value of crust-mantle density contrast for the oceans and continents separately.

- Our research can be extended for the modeling of other interfaces, for instance, the core mantle boundary zone. This can be achieved by a proper truncation of low-degree spherical harmonic coefficients and modeling of inhomogeneities in the mantle.
- New data of GOCE satellite mission is expected to be released during the summer of 2014, which will assist the release of new gravity field models of high resolution and accuracy. Although improved gravity models have only marginal impact on the Moho accuracy, once these models are available, the Moho model may be updated accordingly.
- Another possible extension of our work is to develop Moho models of a higher spatial resolution. This extension is definitely possible for a regional Moho modeling, however, it will be a challenging computational task to do a global Moho recovery. Because the global recovery of high-resolution Moho requires enormous computational power and machine memories.
- The gravimetric model in this study is heavily constrained by a priori seismic models. Such models have a good quality over most of the continental areas, but are poorer over the oceans. Hence, we recommend the use of spatially-varying weights assigned to the a priori models, which may take into account the variations in models accuracies.





# Algorithms for the computation of gravitational potential and attraction for polyhedral body

For an efficient calculation of the gravitational potential and attraction given in Eqs. (3.67) and (3.71) we adopted the same optimum algorithm as proposed by Pohánka (1998). The input parameters are: the value of density  $\rho_0$  at a suitably chosen origin of the local coordinate system used for a description of the density model within the volume of the polyhedral body (we note that this coordinate origin can be located either inside or outside of the polyhedral body), the gradient of a linear density distribution function  $\rho_1$ , the total number of polyhedral faces  $K$ , and the total number of polygon segments  $L(k)$  given for every polyhedral face  $S_k$ . For every vertex of the polyhedral face  $S_k$ , we compute the radius vector  $\mathbf{a}_{k,l}$ . As stated previously, the vertices of the polyhedral face  $S_k$  are numbered in the counter-clockwise sense as viewed from outside, and  $\mathbf{a}_{k,L(k)+1} = \mathbf{a}_{k,1}$ . The last input is the radius vector  $\mathbf{r}$  of the computation point. We note here that the expressions in (3.67) and (3.71) for the potential and attraction respectively holds for any computation point outside and on the surface of the polyhedral body.

The computation is then realized as follows: We compute the lengths  $\{d_{k,l} : l = 1, 2, \dots, L(k); k = 1, 2, \dots, K\}$  of the polygon segments  $L_{k,l}$ , and the corresponding unit vectors  $\{\mu_{k,l} : l = 1, 2, \dots, L(k); k = 1, 2, \dots, K\}$  according to the following equations,

$$d_{k,l} = |\mathbf{a}_{k,l+1} - \mathbf{a}_{k,l}|, \quad \mu_{k,l} = \frac{\mathbf{a}_{k,l+1} - \mathbf{a}_{k,l}}{d_{k,l}}$$

For every polyhedral face  $\{S_k : k = 1, 2, \dots, K\}$  we compute the unit normal vector  $\mathbf{n}_k$  oriented outwards from the polyhedral face  $S_k$  using the following expression,

$$\mathbf{n}_k = \frac{\mathbf{N}_k}{|\mathbf{N}_k|} \text{ where}$$

$$\mathbf{N}_k = \sum_{l=2}^{L(k)-1} (\mathbf{a}_{k,l} - \mathbf{a}_{k,1}) \times (\mathbf{a}_{k,l+1} - \mathbf{a}_{k,1})$$

For every polygon segments  $\{L_{k,l} : l = 1, 2, \dots, L(k)\}$  of the polyhedral face  $S_k$  we compute the normal unit vectors  $\{\nu_{k,l} : l = 1, 2, \dots, L(k)\}$  using Eq. (3.44); i.e.

$$\nu_{k,l} = \mu_{k,l} \times \mathbf{n}_k$$

We further compute the parameters  $\mu_{k,l}, \nu_{k,l}, w_{k,l}, Z_k$ , and  $z_k$  which depend on the position vector  $\mathbf{r}$  of the computation point. With reference to Eqs.(3.50) and (3.53), we have

$$\mu_{k,l}(\mathbf{r}) = \mu_{k,l} \cdot (\mathbf{a}_{k,l} - \mathbf{r})$$

$$\nu_{k,l} = \mu_{k,l} + d_{k,l}$$

$$w_{k,l}(\mathbf{r}) = \nu_{k,l} \cdot (\mathbf{a}_{k,l} - \mathbf{r})$$

$$Z_k(\mathbf{r}) = \mathbf{n}_k \cdot (\mathbf{a}_{k,l} - \mathbf{r}), \quad z_k = |Z_k|$$

For the given numbers  $\mu, \nu$  ( $\nu = \mu + d, d > 0$ ),  $w, z$  ( $z \geq 0$ ) and the parameter  $\epsilon$ , the computation of the functions  $\Phi(\mu, \nu, w, z, \epsilon)$  and  $\Phi_2(\mu, \nu, w, z, \epsilon)$  in Eqs. (3.68) and (3.69) is carried out in the following consecutive steps:

$$(a) \quad z_\epsilon = z + \epsilon,$$

$$(b) \quad W^2 = w^2 + z^2, \quad W_\epsilon^2 = w^2 + z_\epsilon^2,$$

$$(c) \quad U_\epsilon = \sqrt{\mu^2 + W_\epsilon^2}, \quad V_\epsilon = \sqrt{\nu^2 + W_\epsilon^2}, \quad (d) \quad T_\epsilon = U_\epsilon + V_\epsilon,$$

$$(e) \quad \text{sign}(\mu) = \text{sign}(\nu) : L_\epsilon = \text{sign}(\nu) \ln \frac{V_\epsilon + |\nu|}{U_\epsilon + |\mu|}$$

$$(f) \quad \text{sign}(\mu) \neq \text{sign}(\nu) : L_\epsilon = \ln \frac{(V_\epsilon + |\nu|)(U_\epsilon + |\mu|)}{W_\epsilon^2}$$

$$(g) \quad A_\epsilon = -\arctan \frac{2wd}{(T_\epsilon + d)|T_\epsilon - d| + 2T_\epsilon z_\epsilon}.$$

$$(h) \quad \Phi(\mu, \nu, w, z, \epsilon) = w L_\epsilon + 2z A_\epsilon$$

$$(i) \quad \Phi_2(\mu, \nu, w, z, \epsilon) = \frac{1}{4}d \left[ \frac{(\nu + \mu)^2}{T_\epsilon} + T_\epsilon \right] + \frac{1}{2}W^2 L_\epsilon$$

Finally, the gravitational potential and attractions is obtained from Eqs. (3.67) and (3.71) respectively.



## Link between the Stokes coefficients $C_{lm}$ and the mass distribution inside the Earth

The expression for the gravitational potential generated by the entire Earth of volume  $v$  is

$$V(r, \theta, \lambda) = G \iiint_{\text{Earth}} \frac{1}{d} \rho(r', \theta', \lambda') dv' \quad (\text{B.1})$$

where  $dv' = r'^2 \sin \theta' dr' d\theta' d\lambda'$  is the volume element,  $\rho(r', \theta', \lambda')$  is density at the given point, and  $d$  is the distance between the observation point  $(r, \theta, \lambda)$  and the integration point  $(r', \theta', \lambda')$ :

$$d = \sqrt{r^2 - 2rr' \cos \psi + r'^2} \quad (\text{B.2})$$

where  $\psi$  is the angular distance between these points. Hence,

$$\frac{1}{d} = \frac{1}{r \sqrt{1 - 2 \left(\frac{r'}{r}\right) \cos \psi + \left(\frac{r'}{r}\right)^2}},$$

the explicit expression for  $\frac{1}{d}$  can be written as (cf. [Moritz, 2006](#) Eq. (2-65)):

$$\frac{1}{d} = \sum_{l=0}^{\infty} \frac{r'^l}{r^{l+1}} P_l(\cos \psi), \quad (\text{B.3})$$

where  $P_l(\cos \psi)$  is Legendre polynomials. Eq. (B.3) converges for  $r > r'$ . Using the addition theorem, the expression for the Legendre function can be re-written as

$$P_l(\cos \psi) = \frac{1}{2l+1} \sum_{m=-l}^l \bar{Y}_{lm}(\theta', \lambda') \bar{Y}_{lm}(\theta, \lambda) \quad (\text{B.4})$$

after substituting Eqs. (B.3), and (B.4) into Eq. (B.1), the expression for the gravitational potential can be written as:

$$V(r, \theta, \lambda) = \frac{G}{r} \sum_{l=0}^{\infty} \sum_{m=-l}^l \frac{1}{2l+1} \bar{Y}_{lm}(\theta, \lambda) \iiint_{\text{Earth}} \rho(r', \theta', \lambda') \left(\frac{r'}{r}\right)^l \bar{Y}_{lm}(\theta', \lambda') dv'. \quad (\text{B.5})$$

On the other hand, the gravitational potential of the Earth can be represented as:

$$V(r, \theta, \lambda) = \frac{GM}{r} \sum_{l=0}^{\infty} \sum_{m=-l}^l \bar{C}_{lm} \left(\frac{R}{r}\right)^l \bar{Y}_{lm}(\theta, \lambda) \quad (\text{B.6})$$

where  $R = 6378136.3$  m is major semi-axis of the reference ellipsoid.

Comparing Eq. (B.5) and Eq. (B.6), we get the link between the Stokes coefficients and the density distribution inside the Earth

$$\bar{C}_{lm} = \frac{1}{M(2l+1)} \iiint_{\text{Earth}} \rho(r', \theta', \lambda') \left(\frac{r'}{R}\right)^l \bar{Y}_{lm}(\theta', \lambda') dv'. \quad (\text{B.7})$$

Now the variation in Moho depth  $b$  produces a variation in the Stokes coefficients  $\delta C_{l,m}$  of gravity field. This variation is produced due to surface mass changes. At the spherical surface of radius  $\tilde{R}$ : these mass changes can be represented as a variation of surface density  $\delta s(\theta', \lambda')$  in a thin layer between radii  $r_1$  and  $r_2$

$$\delta s(\theta, \lambda) = \int_{r_1}^{r_2} \delta \rho(r', \theta', \lambda') dr', \quad (\text{B.8})$$

After integration in the radial direction, the 3-D integral in Eq. (B.7) turns into 2-D integral:

$$\delta\bar{C}_{lm} = \frac{1}{M(2l+1)} \left(\frac{\tilde{R}}{R}\right)^l \iint_{\Omega_{\tilde{R}}} \delta s(\theta', \lambda') \bar{Y}_{lm}(\theta', \lambda') d\Omega'_{\tilde{R}},$$

where  $\Omega'_{\tilde{R}}$  is the sphere of radius  $\tilde{R} = R - z_0$ ,  $z_0$  is the reference Moho depth, and  $d\Omega'_{\tilde{R}}$  is an element of this sphere. Moreover,  $d\Omega'_{\tilde{R}} = \tilde{R}^2 d\Omega'$ , where  $d\Omega'$  is an element of the unit sphere  $\Omega'$ . Hence,

$$\delta\bar{C}_{lm} = \frac{\tilde{R}^2}{M(2l+1)} \left(\frac{\tilde{R}}{R}\right)^l \iint_{\Omega} \delta s(\theta', \lambda') \bar{Y}_{lm}(\theta', \lambda') d\Omega'. \quad (\text{B.9})$$





---

## Optimum regularization parameter estimation using Variance Component Estimation (VCE)

The Variance Components Estimation (VCE) technique is one of the methods suggested in literature to estimate the regularization parameter and data weights. The variance factor of a given data set is given by (Kusche, 2003)

$$\sigma_d^2 = \frac{1}{n - \tau_d} (d - A\hat{x})^T P_d (d - A\hat{x}),$$

where  $n$  is the total number of observations in the data set and

$$\tau_d = \text{trace}[N_d N^{-1}],$$

where  $N$  is the normal matrix defined by the least squares adjustment formula (6.33). It can be written as the sum of two matrices

$$N = N_d + N_x, \tag{C.1}$$

The part of the normal matrix related to the data vector  $d$  is

$$N_d = \frac{1}{\sigma_d^2} A^T P_d A,$$

and the part of the normal matrix related to the model  $x$

$$N_x = \frac{1}{\sigma_x^2} \mathbf{R}.$$

Similarly, the variance of the model parameter  $x$  can be estimated by

$$\sigma_x^2 = \frac{1}{u - \tau_x} \hat{x}^T \mathbf{R} \hat{x},$$

where  $u$  is the total number of unknown parameters and  $\tau_x = \text{trace} [N_x N^{-1}]$ .

# Bibliography

- Airy, G. (1855). On the computations of the effect of the attraction of the mountain masses as disturbing the apparent astronomical latitude of stations in geodetic surveys. *Trans. Roy. Soc. (London), ser. B,*, 145. [1](#)
- Aitken, A., Salmon, M., and Kennett, B. (2013). Australia's moho: A test of the usefulness of gravity modelling for the determination of moho depth. *Tectonophysics*, 609:468–479. [2.2](#)
- Alvey, A., C, G., Kuszniir, N., and Torsvik, T. (2008). Integrated crustal thickness mapping and plate reconstructions for the high Arctic. *Earth Planet Sci Lett*, 274:310–321. [4](#)
- Amante, C. and Eakins, B., W. (2009). ETOPO1 1arc-minute global relief model. *Procedures data source and analysis NOAA technical memorandum NESDIS NGDC-24*, page 19pp. [2.4](#), [4.1.1](#)
- Anderson, O, B. (2010). The dtu10 gravity field and mean sea surface. *Second international symposium of the gravity field of the Earth*, (IGFS2):Fairbanks, Alaska. [2.9](#)
- Anderson, O, B., Knudsen, P., and Berry, P. (2009). DNSC08 mean sea surface and mean dynamic topography models. *Journal of geophysical research*, 114:c11001 12 Pp. [2.9](#)
- Arabelos, D., Mantzios, G., and Tsoulis, D. (2007). Moho Depths in the Indian Ocean Based on the Inversion of Satellite Gravity Data. *Advances in Geosciences, Volume 9: Solid Earth, Ocean Science and Atmospheric Science*, 9:41–52. [2.11](#)
- Artemjev, M. and Kaban, M. (1994). Density inhomogeneities, isostasy and flexural rigidity of the lithosphere in the Transcaspian region. *Tectonophysics*, 240:281–297. [4](#)
- Artemjev, M., Kaban, M., Kucherinenko, V., Demjanov, G., and Taranov, V. (1994). Subcrustal density inhomogeneities of the Northern Euroasia as derived from the gravity data and isostatic models of the lithosphere. *Tectonophysics*, 240:248–280. [4.4](#)

- Bagherbandi, M. (2012). A comparison of three gravity inversion methods for crustal thickness modelling in tibet plateau. *Journal of Asian Earth Sciences*, 43(1):89 – 97. [2.11](#)
- Bagherbandi, M. and Eshagh, M. (2012). Crustal thickness recovery using an isostatic model and GOCE data. *Earth, Planets, and Space*, 64:1053–1057. [2.11](#)
- Bagherbandi, M., Tenzer, R., Sjöberg, L. E., and Novák, P. (2013). Improved global crustal thickness modeling based on the VMM isostatic model and non-isostatic gravity correction. *Journal of Geodynamics*, 66:25–37. [2.11](#), [2.11](#), [4.4](#)
- Banjeree, P. and Satyaprakash, W. (2003). Crustal configuration across the north-western himalaya as inferred from gravity and gps aided geoid undulation studies. *Journal of the Virtual Explorer*, 12:93–106. [2.2](#)
- Barnett, C. T. (1976). Theoretical modeling of the magnetic and gravitational fields of an arbitrary shaped three-dimensional body. *Geophysics*, 41(6):1353–1364. [3](#)
- Bassin, C., Laske, G., and Masters, G. (2000). The current limits of resolution for surface wave tomography in North America. *EOS Trans AGU*, 81:F897. [2.4](#), [4](#)
- Bessel, F. (1813). Auszug aus einem schreiben des herrn prof. bessel. zach's monatliche correspondenz zur beförderung der erd- und himmelskunde. XXVII:80–85. [3](#)
- Bielik, M. (1988). A preliminary stripped gravity map of the Pannonian Basin. *Phys Earth Planet Inter*, 51:185–189. [4](#)
- Braitenberg, C., Mariani, P., Reguzzoni, M., and Ussami, N. (2010). Goce observations for detecting unknown tectonic features. In *Proc. of the ESA Living Planet Symposium*, volume 28. [2.11](#)
- Braitenberg, C., Zadra, M., and Fang, J. (2000). The gravity and isostatic moho undulations in qinghai-tibet plateau . *Journal of Geodynamics*, 30(5):489–505. [2.2](#)
- Braitenberg, C., Z. M. (1999). Iterative 3d gravity inversion with integration of seismologic data. . *Boll. Geof Teor. App*, 40:469–476. [2.11](#)
- Braun, A., HR, K., B, C., and von Frese RRB (2007). Gravity-inferred crustal thickness of Greenland. *Earth Planet Sci Lett*, pages 138–158. [4](#)
- Bullen, K. (1975). *The Earth's density*. Chapman and Hall. [2.1](#)
- Cadek, O. and Martinec, Z. (1991). Spherical harmonic expansion of the earth's crustal thickness up to degree and order 30. *Studia Geophysica et Geodaetica*, 35(3):151–165. [2.11](#)

- Carlson, R. and Raskin, G. (1984). Density of the ocean crust. *Nature* 311, 311:555–558. [2.3](#)
- Chai, Y, H. W. (1988). Gravity inversion of an interface above which the density contrast varies exponentially with depth. *Geophysics*, 53:837–845. [3](#)
- Chen and Tenzer (2014). Harmonic coefficients of the earth's spectral crustal model 180-escm180. *Earth Scie Inf*, sum. [2.4](#)
- Collette, B. (1965). Charts for determining the gravity effect of two and three-dimensional bodies bounded by arbitrary polygons. *Geophysical Prospecting*, 13(1):12–21. [3](#)
- Dérerová, J., Zeyen, H., Bielik, M., and Salman, K. (2006). Application of integrated geophysical modeling for determination of the continental lithospheric thermal structure in the eastern Carpathians. *Tectonics*, 25(3):doi: TC3009 10.1029/2005TC001883. [4](#)
- Ditmar, P. (2010). Lecture notes: AE4-E10: Inverse problems. [6.5](#)
- Drinkwater, M., Floberghagen, R., Haagmass, R., Muzi, D., and Papescu, A. (2003). GOCE: ESA's first Earth explorer core mission. *Space Sci Rev.*, 00:1–14. [1.1](#)
- Dziewonski, A. and Anderson, D. (1981). Preliminary reference Earth model. *Phys. Earth Planet. Inter.*, 25:297–356. [2.1](#), [2.3](#), [2.4](#), [5](#)
- Dziewonski, A., Hales, A., and Lapwood, E. (1975). Parametrically simple earth models consistent with geophysical data. *Phys Earth Planet Inter*, page 10:12. [2.4](#)
- Everest, G. (1830). An account of the measurement of the arc of the meridian between the parallels of 18 3 and 24 7. *The Royal Society, Printed by JL Cox, London.* [3](#)
- Floberghagen, R., Fehringer, M., Lamarre, D., Muzi, D., Frommknecht, B., Steiger, C., Piñeiro, J., and Costa, A. (2011). Mission design, operation and exploitation of the Gravity field and steady-state Ocean Circulation Explorer mission. *Journal of Geodesy*, 85(11):749–758. [1.1](#)
- Foerste, C., Schmidt, R., Stubenvoll, R., Flechtner, F., Meyer, U., KÄnig, R., Neumayer, H., Biancale, R., Lemoine, J.-M., Bruinsma, S., Loyer, S., Barthelmes, F., and Esselborn, S. (2008). The geoforschungszentrum potsdam/groupe de recherche de geodesie spatiale satellite-only and combined gravity field models: Eigen-gl04s1 and eigen-gl04c. *Journal of Geodesy*, 82:331–346. [2.4](#)
- Förste, C., Bruinsma, S., shako, R., charles Marty, J., Flechtner, F., Abrikosov, O., Dahle, C., lemoine, J., Neumayer, H., Biancale, R., Barthelmes, F., König, R., and Balmino., G. (2011). EIGEN-6: A new combined global gravity field model including GOCE data from the collaboration of GFZ-Potsdam and GRGS-Toulouse. In *EGU general assembly*. [2.4](#), [2.9](#)

- Förste, C., Sean, B., Flechtner, F., Marty, J.-C., Dahle, C., Abrykosov, O., Lemoine, J.-M., Neumayer, H., Barthelmes, F., Biancale, R., and König, R. (2013). Eigen-6c2 - a new combined global gravity field model including goce data up to degree and order 1949 of gfg potsdam and grgs toulouse. *Geophysical Research Abstracts: EGU General Assembly*, 15:4077–1. [2.9](#), [4.1.3](#), [4.2](#)
- Gallardo-Delgado, L., Perez-Flores, M., and Gomez-Trevino, E. (2003). A versatile algorithm for joint inversion of gravity and magnetic data. *Geophysics*, 68:949–959. [3](#)
- García-Abdeslem (1992). Gravitational attraction of a rectangular prism with depth dependent density. *Geophysics*, 57:470–473. [3](#)
- García-Abdeslem (2005). Gravitational attraction of a rectangular prism with density varying with depth following a cubic polynomial. *Geophysics*, 70:J39–J42. [3](#)
- Gibb, R. (1968). The densities of precambrian rocks from northern manitoba,. *Canadian Journal of Earth Sciences*, 5:433 –438. [5](#)
- Goodacre, A. (1972). Generalized structure and composition of the deep crust and upper mantle in Canada. *J. Geophys. Res.*, 77:3146–3160. [5](#)
- Götze, H. J. and Lahmeyer, B. (1988). Application of three-dimensional interactive modeling in gravity and magnetics. *Geophysics*, 53(8):1096–1108. [3](#)
- Grad, M., Timo, T., and Group, E. W. (2009). The moho depth map of the european plate. *Geophys. J. Int.*, 176:279–292. [2.2](#), [2.4](#), [7.1.1](#)
- Gruninger, W. (1991). Zur topographisch-isostatischen reduktion der schwere. PhD thesis, Universität Karlsruhe. pages –. [3.4](#), [3.4](#)
- Hansen, R. O. (1999). An analytical expression for the gravity field of a polyhedral body with linearly varying density. *Geophysics*, 64:75–77. [3](#)
- Harkness, W. (1891). Solar parallax and its related constants, including the figure and density of the earth,. *Government Printing Office*. [5](#)
- Hayford, J.F., a. B. W. (1912). The effect of topography and isostatic compensation upon the intensity of gravity,. *U.S. Coast and Geodetic Survey*,, 10:Special Publication. [5](#)
- Hayford, J. (1909a). The figure of the earth and isostasy from measurements in the united states. *USCGS*. [2](#)
- Hayford, J. (1909b). The figure of the earth and isostasy from measurements in the united states:. *U.S. Coast and Geodetic Survey*. [5](#)

- Hayford, J. and Bowie, W. (1912). The effect of topography and isostatic compensation upon the intensity of gravity. *USCGS, Spec. Publ.*, 10. [2](#)
- Heck, B. and Seitz, K. (2007). A comparison of the tesseroid, prism and point-mass approaches for mass reductions in gravity field modelling. *Journal of Geodesy*, 81(2):121–136–136. [3.4](#), [3.4](#)
- Heiskanen, W.A., a. V. M. F. (1958). *The Earth and its Gravity Field*. McGraw-Hill Book Company, Inc. [1](#)
- Heiskanen, W.H., M. H. (1967). *Physical geodesy*. San Francisco, W.H., Freeman and Co. [2.2](#), [2.7](#), [5](#)
- Hinze, W. (2003). Bouguer reduction density, why 2.67? *Geophysics*, 68(5):1559–1560. [2.3](#), [5](#)
- Holstein, H. (2002a). Gravimagnetic similarity in anomaly formulas for uniform polyhedra. *Geophysics*, 67(4):1126–1133. [3](#)
- Holstein, H. (2002b). Invariance in gravimagnetic anomaly formulas for uniform polyhedra. *Geophysics*, 67(4):1134–1137. [3](#)
- Holstein, H. (2003). Gravimagnetic anomaly formulas for polyhedra of spatially linear media. *Geophysics*, 68(1):157–167. [3](#), [3.5](#)
- Holstein, H. and Ketteridge, B. (1996). Gravimetric analysis of uniform polyhedra. *J. Geophysics*, 61(2):49–59. [3](#)
- Holstein, H., Schürholz, P., Starr, A., and Chakraborty, M. (1999). Comparison of gravimetric formulas for uniform polyhedra. *Geophysics*, 64(5):1438–1446. [3](#)
- Hubbert and King, M. (1948). A line integral method of computing the gravimetric effects of two-dimensional masses. *Geophysics*, 13(2):215–225. [3](#)
- Ivan, M. (1990). COMMENT ON "OPTIMUM EXPRESSION FOR COMPUTATION OF THE GRAVITY FIELD OF A HOMOGENEOUS POLYHEDRAL BODY" BY V. POHÁ1 coments on "Optimum expression for computation of the gravity field of a homogeneous polyhedral body" by V. POHÁ. *Geophysical Prospecting*, 38(3):331–332. [3](#)
- Jiménez-Munt, I., M, F., Vergés, J., and Platt, J. (2008). Lithosphere structure underneath the Tibetan Plateau inferred from elevation, gravity and geoid anomalies. *Earth Planet Sci Lett*, 267:276–289. [4](#)
- Julia, J. (2007). Constraining velocity and density contrasts across the crust-mantle boundary with receiver function amplitudes. *Geophys. J. Int.*, 171:286–301. [5](#)

- Kaban, M. and Schwintzer, P. (2001). Oceanic upper mantle structure from experimental scaling of Vs and density at different depths. *Geophys J Int*, 147:199–214. [4](#)
- Kaban, M., Schwintzer, P., Artemieva, I., and Mooney, W. (2003). Density of the continental roots compositional and thermal contributions. *Earth Planet Sci, Lett* 209:53–69. [2.11](#), [4](#), [4.3](#)
- Kaban, M., Schwintzer, P., and Reigber, C. (2004). A new isostatic model of the lithosphere and gravity field. *Journal of Geodesy*, 78:368–385. [2.11](#), [2.11](#), [4](#)
- Kaban, M., Schwintzer, P., and Tikhotsky, S. (1999). Global isostatic gravity model of the Earth. *Geophys J Int*, 136:519–536. [2.2](#), [2.11](#), [2.11](#), [4](#)
- Kellogg, O. D. (1929). *Foundations of Potential Theory*. Berlin Verlag Von Julius Springer. [2.5](#)
- King, R., Yuan, X., and Saul, J. (2002). Seismic images of the crust and upper mantle beneath tibet: Evidence for eurasian plate subduction. *Science*, 298(5596):1 219–1221. [2.2](#)
- Kusche, J. (2003). A Monte-Carlo technique for weight estimation in satellite geodesy. *Journal of Geodesy*, 76:641–652. 10.1007/s00190-002-0302-5. [C](#)
- Kustowski, B., Ekstrom, G., and Dziewonski, A. (2008). Anisotropic shear-wave velocity structure of the earth's mantle: A global model. *J Geophys Res*, 113. [2.4](#)
- Kwok, Y.-K. (1991). Gravity gradient tensors due to a polyhedron with polygonal facests. *Geophysical Prospecting*, 39(3):435–443. [3](#)
- Laske, G., Masters, G., Zhitu, M., and Pasyanos, M. (2013). Update on crust1.0– a 1-degree global model of earth's crust. *Geophysical Research Abstracts*, 15. [2.4](#), [4](#), [5.1](#)
- Laske, G. Masters, G. (1997). A global digital map of sediment thickness. *EOS Trans. AGU*, 78:F483. [2.4](#), [4.1.5](#)
- Mader, K. (1951). Das Newtonsche raumpotential prismatischer Körper und seine ableitungen bis zur dritten Ordnung. Sonderheft 11 der Österreichischen Zeitschrift für Vermessungswesen. Österreichischer Verein für vermessungswesen, wien. pages –. [2.5](#), [3](#), [3.4](#), [3.4](#)
- Magdala, T., Kaban, M., Sierd, and A., P., L. . C. (2008). Eucrust-07: A new reference model for the european crust. *Geophysical research letters*, 35, L05313:doi:10.1029/2007GL032244, 2008. [2.2](#), [2.4](#), [7.1.1](#)
- Mariani, Patrizia, Braitenberg, C., and Ussami, N. (2013). Explaining the thick crust in paraná basin, brazil, with satellite goce gravity observations. *Journal of South American Earth Sciences*, 45:209–223. [2.2](#), [2.4](#)



- Martinec, Z. (1994). The density contrast at the Mohorovičić discontinuity. *Geophys. J. Int.*, 117:539–544. [5](#)
- Martinec, Z. (1998). *Boundary value problems for gravimetric determination of a precise geoid.. Lecture Notes in Earth Sciences, Vol 73*. Springer Verlag, Berlin, Heidelberg,, New York. [3.3](#)
- Meier, U., Curtis, A., and Trampert, J. (2007). Fully nonlinear inversion of fundamental mode surface waves for a global crustal model. *GEOPHYSICAL RESEARCH LETTERS*, 34:L16304, doi:10.1029/2007GL030989,. [2.2](#), [2.4](#)
- Mohorovičić, A. (1910). Earthquake of 8 October 1909 (English translation of "Potres of 8.X.1909", Godišnje izvješće zagrebačkog meteorološkog opservatorija, 9(4/1), 1-56). *Geofizika*, pages 1–56. [2.2](#)
- Mohorovičić, A. (1992). Earthquake of 8 October 1909 (English translation of "Potres of 8.X.1909", Godišnje izvješće zagrebačkog meteorološkog opservatorija, 9(4/1), 1-56). *Geofizika*, 9:3–56. [2.2](#)
- Mollweide, K. (1813). Auflösung einiger die anziehung von linien flächen und köpern betreffenden aufgaben unter denen auch die in der monatl corresp . vorgelegte sich findet. zach's monatliche correspondenz zur beförderung der erd- und himmelskunde,. *Bd XXIV. S*, 522:26–38. [3](#)
- Mooney, W., Laske, G., and Masters, T. (1998). CRUST 5.1: A global crustal model at 5 x 5 degree. *J Geophys Res*, 103B:727–747. [2.2](#), [2.4](#)
- Moritz, H. (1990). *The Figure of the Earth*,. Wichmann H., Karlsruhe,. [2.11](#), [2.12](#)
- Moritz, H. (2006). *Physical geodesy*. Springer-Verlag Wien Austria. [2.6](#), [2.7](#), [2.8](#), [2.8](#), [2.10](#), [B](#)
- Nagy, D. (1966). The gravitational attraction of a right rectangular prism. *Geophysics*, 31(2):362–371. [3.4](#), [3.4](#)
- Nagy, D., Papp, G., and Benedek, J. (2000). The gravitational potential and its derivatives for the prism. *Journal of Geodesy*, 74(7):552–560. [3](#), [3.4](#), [3.4](#)
- Nagy, D., Papp, G., and Benedek, J. (2002). Corrections to "The gravitational potential and its derivatives for the prism". [3.4](#), [3.4](#)
- Nataf, H.C., a. R. Y. (1996). 3smac: An a priori tomographic model of the upper mantle based on geophysical modeling. *Phys. Earth Planet. Int.* 95, 95:101–122. [2.4](#)
- Niu, F. and James, D. (2002). Fine structure of the lowermost crust beneath the Kaapvaal craton and its implications for crustal formation and evolution. *Earth Planet. Sci. Lett.*, 200:121–130. [5](#)

- Okabe, M. (1979). Analytical expressions for gravity anomalies due to homogeneous polyhedral bodies and translations into magnetic anomalies. *Geophysics*, 44(4):730–741. [3](#)
- Oldenburg, D. (1974). The inversion and interpretation of gravity anomalies. *Geophysics*, 39:525–536. [2.11](#), [2.11](#), [2.11](#)
- Parker, R. L. (1973). The rapid calculation of potential anomalies. *Geophysical Journal of the Royal Astronomical Society*, 31(4):447–455. [2.11](#)
- Pasyanos, M., Masters, G., Laske, G., and Ma, Z. (2012). Litho1.0 -an updated crust and lithospheric model of the earth developed using multiple data constraints. *Fall Meeting, AGU, San Francisco, Calif.*, Abstract:3–7 Dec, 2012. [2.4](#)
- Paul, M. K. (1974). The gravity effect of a homogeneous polyhedron for three-dimensional interpretation. [3](#)
- Pavlis, N., Holmes, S., Kenyon, S., and Factor, J. (2008). An Earth gravitational model to degree 2160: EGM 2008a. In *presented at Session G3: "GRACE Science Applications", EGU Vienna*, Vienna, Austria. Presented at the 2008 General assembly of the European Geosciences Union. [2.9](#)
- Pearson, K. (1896). *Mathematical contributions to the theory of evolution. III - Regression, heredity and panmixia*. Phil. Trans. Royal Soc. London Ser. A, 187, pp. 253-318. [5.1](#)
- Petrović, S. (1996). Determination of the potential of homogeneous polyhedral bodies using line integrals. [3](#)
- Pohánka, V. (1988). Optimum expression for computation of the gravity field of a homogeneous polyhedral body. *Geophysical Prospecting*, 36(7):733–751. [3](#), [3.5](#), [3.5](#), [3.5](#), [3.5](#)
- Pohánka, V. (1990). Reply to coment by M. Ivan. *Geophysical Prospecting*, 38(3):333–335. [3](#), [3.5](#), [3.5](#)
- Pohánka, V. (1998). Optimum expression for computation of the gravity field of a polyhedral body with linearly increasing density. *Geophysical Prospecting*, 46(4):391–404. [3](#), [3.5](#), [3.5](#), [3.5](#), [3.5](#), [3.5](#), [3.5](#), [3.5](#), [3.5](#), [3.5](#), [3.5](#), [3.5](#), [A](#)
- Pratt, J. (1855). On the attraction of the himalaya mountains and of the elevated regions beyond upon the plumb-line in india. *Trans. Roy. Soc. (London)*, 145:ser B. [2](#)
- Reigber, C., Bock, R., Forste, C., Grunwaldt, L., Jakowski, N., Lühr, H., Schwintzer, P., and Tilgner, C. (1996). CHAMP phase B executive summary, GFZ. *Potsdam, Germany*, STR96/13. [1.1](#)

- Reigber, C., Lühr, H., and Schwintzer, P. (2002). CHAMP mission status. *Adv. Space Res.*, 30:129–134. [1.1](#)
- Reigber, C., Schwintzer, P., and Lühr, H. (1999). The CHAMP geopotential mission. *Boll Geof Teor Appl*, 40:285–289. [1.1](#)
- Rogers N., Blake S., B. K. (2008). *An introduction to our dynamic planet*. Cambridge University Press. [2.3](#)
- Sampietro, D. (2011). Goce exploitation for moho modeling and applications. In *In: Proc. of the 4th International GOCE User Workshop, 31 March - 1 April, Munich, Germany*. [2.11](#)
- Simmons, N., Forte, A., Boschi, L., and Grand, S. (2010). Gypsum: A joint tomographic model of mantle density and seismic wave speeds. *J Geophys Res*, 115:B12310. [2.4](#)
- Sjöberg, L.E., B. M. (2011a). A method of estimating the Moho density contrast with a tentative application by EGM08 and CRUST2.0. *Acta Geophys.*, 59:502–525. [5](#), [5.5](#)
- Sjöberg, L.E., B. M. (2011b). A method of estimating the moho density contrast with a tentative application by egm08 and crust2.0. *Acta Geophys.*, 58:1–24. [2.3](#)
- Sjöberg, L. (2009). Solving vening meinesz-moritz inverse problem in isostasy. *Geophysical Journal International*,, 179:1527–1536. [2.11](#), [2.11](#), [2.12](#), [2.12](#), [2.12](#), [2.12](#)
- Subrahmanyam, C., V. R. (1981). Densities and magnetic susceptibilities of precambrian rocks of different metamorphic grade (southern indian shield),. *J. Geophys.*, 49:101 – 107. [5](#)
- Takin, M. and Talwani, M. (1966). Rapid computation of the gravitation attraction of topography on a spherical Earth. *Geophysical Prospecting*, 14(2):119–142. [3](#)
- Talwani, M. and Ewing, M. (1960). Rapid computation of gravitational attraction of three-dimensional bodies of arbitrary shape. *Geophysics*, 25(1):203–225. [3](#)
- Talwani, M., Worzel, J. L., and Landisman, M. (1959). Rapid gravity computations for two-dimensional bodies with application to the mendocino submarine fracture zone. *J. Geophys. Res.*, 64(1):357–364. [3](#)
- Tapley, B. D., Bettadpur, S., Watkins, M., and Reigber, C. (2004). The gravity recovery and climate experiment: Mission overview and early results. *Geophysical Research Letters*, 31(9):L09607. [1.1](#)
- Tassara, A., Swain, C., Hackney, R., and Kirby, J. (2007). Elastic thickness structure of South America estimated using wavelets and satellite-derived gravity data. *Earth Planet Sci Lett*, 253:17–36. [4](#)

- Tedla, G. E., Meijde, M. v. d., Nyblade, A. A., and Meer, F. D. v. d. (2011). A crustal thickness map of africa derived from a global gravity field model using euler deconvolution. *Geophysical Journal International*, 187(1):1–9. [2.4](#)
- Tenzer, R. and Bagherbandi, M. (2012). Reformulation of the vening-meinesz moritz inverse problem of isostasy for isostatic gravity disturbances. *International Journal of Geosciences*, 3:918–929. [2.11](#), [2.12](#)
- Tenzer, R., Bagherbandi, M., and Hwang Ch., and Chang, E. (2013). Moho interface modeling beneath himalayayas, tibet and central siberia using goco02s and dtm2006.0. *Special issue on geophysical and climate change studies in Tibet, Xinjiang, and Siberia from satellite geodesy. Terrestrial, Atmospheric and Oceanic Sciences (2013)*, doi: 10.3319/TAO.2012.11.01.02(TibXS). [2.11](#)
- Tenzer, R., Hamayun, Novák, P., Gladkikh, V., and P., V. (2012a). Global crust-mantle density contrast estimated from egm2008, dtm2008, crust2.0, and ice-5g. *Pure Appl. Geophys.*, 169,9:1663–1678. [2.2](#), [2.3](#), [4.3](#)
- Tenzer, R., Hamayun, and Vajda, P. (2009a). Global maps of the CRUST 2.0 crustal components stripped gravity disturbances. *J. Geoph. Res*, 114:B, 05408. [2.11](#), [4.4](#)
- Tenzer, R., Hamayun, and Vajda, P. (2009b). Global maps of the crust 2.0 crustal components stripped gravity disturbances. *J. Geophys. Res.* 114,, page B05408. [5](#)
- Tenzer, R., Novák, P., Vajda, P., Gladkikh, V., and Hamayun (2012b). Spectral harmonic analysis and synthesis of earth's crust gravity field. *Computational Geosciences*, 16(1):193–207. [2.11](#)
- Tikhonov, A. N. (1963a). Regularization of incorrectly posed problems. *Soviet Mathematics*, 4(6):1524–1627. [6.5](#)
- Tikhonov, A. N. (1963b). Solution of incorrectly formulated problems and the regularization method. *Soviet Mathematics*, 4(4)(2):1035–1038. [6.5](#)
- Torge, W. (1991). *Geodesy*. De Gruyter. [2.1](#), [2.10](#), [2.10](#), [2.10](#)
- Trabant, C., Hutko, A., Bahavar, M., Karstens, R., Ahern, T., and Aster, R. (2012). Data products at the iris dmc: stepping-stones for research and other application,. *Seism Res Lett*, 83(6):846–854. [2.4](#)
- Tsoulis, D. and Petrović, S. (2001). On the singularities of the gravity field of a homogeneous polyhedral body. *Geophysics*, 66(2):535–539. [3](#)
- Tugume, F., Nyblade, A., Juliá, J., and van der Meijde, M. (2013). Precambrian crustal structure in africa and arabia: Evidence lacking for secular variation. *Tectonophysics*, 609(0):250 – 266. Moho: 100 years after Andrija Mohorovicic. [2.4](#), [5](#), [7](#), [7.4.2](#)

- Vajda, P., Ellmann, A., Meurers, B., Vaníček, P., Novák, P., and Tenzer, R. (2008). Global ellipsoid-referenced topographic, bathymetric and stripping corrections to gravity disturbance. *Studia Geophysica et Geodaetica*, 52(1):19–34. [4](#)
- Vajda, P. and Vaníček, P. and, M. B. (2006). A new physical foundation for anomalous gravity. *Studia Geophysica et Geodaetica*, 50(2):189–216. [4](#)
- Vajda, P., Vaníček, P., Novák, P., Tenzer, R., and Ellmann, A. (2007). Secondary indirect effects in gravity anomaly data inversion or interpretation. *J. Geophys. Res., Solid Earth*, 112:B06411. [2.11](#), [4](#)
- Van der Lee, S. and Nolet, G. (1997). Upper mantle s-velocity structure of north america. *J Geophys Res*, 102:22815–22838. [2.4](#)
- Van der Meijde, M., Juliá, J., and Assumpção, M. (2013). Gravity derived moho for south america. *Tectonophysics*, 609:456–467. [2.2](#), [2.4](#), [7](#), [7.4.1](#)
- Vening Meinesz, F, A. (1931). Unenouvelle méthode pour la réduction isostatique régionale de l'intensité de la pesanteur. *Bulletin Geodesique*, 29:33–51. [2.12](#)
- Watts, A. (2001). *Isostasy and flexure of the lithosphere*,. Cambridge University Press, Cambridge. [2.11](#)
- Werner, R. and Scheeres, D. (1996). Exterior gravitation of a polyhedron derived and compared with harmonic and mascon gravitation representations of asteroid 4769 Castalia. [3](#)
- West, B., Fujimoto, H., Honsho, C., Tamaki, K., and Sempéré, J. (1995). A three-dimensional gravity study of the Rodrigues Triple Junction and Southeast Indian Ridge. *Earth Planet Sci Lett*, 133:175–184. [4](#)
- Woollard, G. (1962). The relation of gravity anomalies to surface elevation, crustal structure, and geology,. *University of Wisconsin Geophysics and Polar Research Center Research Report*, 62:9 pp. [5](#)
- Woollard, G. (1966). Regional isostatic relations in the united states, in: S teinhart , j.s., s mith , t.j. (eds.), the earth beneath the continents,. *American Geophysical Union Geophysical*, 10:557 – 594. [5](#)
- Woollard, G. P. (1971). *The Earth crust and upper Mantle*. National academy of sciences- national research council publication. [2.3](#)
- Zach (1811). Correspondenz zur beförderung der erd- und himmelskunde. *Bd XXVII*., page 522. [3](#)
- Zeyen, H., Dererova, J., and Bielik, M. (2002). Determination of the continental lithosphere thermal structure in the Western Carpathians: integrated modelling of surface heat flow, gravity anomalies and topography. *Phys Earth Planet Inter*, 134:89–104. [4](#)



# List of publication

## Peer Reviewed Journal Articles

1. Tenzer R, Hamayun, Vajda P (2008) Global secondary indirect effects of topography, bathymetry, ice and sediments. *Contributions to Geophysics and Geodesy* 38(2): 209-216
2. Tenzer R, Hamayun, Vajda P (2008) Global map of the gravity anomaly corrected for complete effects of the topography, and of density contrasts of global ocean, ice, and sediments. *Contributions to Geophysics and Geodesy* 38(4): 357-370
3. Hamayun, Prutkin I, Tenzer R (2009) The optimum expression for the gravitational potential of polyhedral bodies having a linearly varying density distribution. *Journal of Geodesy* 83: 1163-1170
4. Tenzer R, Hamayun, Vajda P (2009) Global maps of the step-wise topography corrected and crustal components stripped geoids using the CRUST 2.0 model. *Contributions to Geophysics and Geodesy* 39(1): 1-18
5. Tenzer R, Hamayun, Vajda P (2009) A global correlation of the step-wise consolidated crust-stripped gravity field quantities with the topography, bathymetry, and the CRUST 2.0 Moho boundary. *Contributions to Geophysics and Geodesy* 39(2): 133-147
6. Tenzer R, Vajda P, Hamayun (2009) Global atmospheric corrections to the gravity field quantities. *Contributions to Geophysics and Geodesy* 39(3): 221-236
7. Tenzer R, Hamayun, Vajda P (2009) Roughness of three types of gravity disturbances and their correlation with topography in rugged mountains and flat regions. *Acta Geophysica* 57(3): 657-679
8. Tenzer R, Hamayun, Vajda P (2009) Global maps of the CRUST 2.0 crustal components stripped gravity disturbances. *Journal Geophysical Research (Solid Earth)*, 114; B05408
9. Tenzer R, Vajda P, Hamayun (2010) A mathematical model of the bathymetry-generated external gravitational field. *Contributions to Geophysics and Geodesy* 40(1): 31-44

10. Tenzer R, Abdalla A, Vajda P, Hamayun (2010) The spherical harmonic representation of the gravitational field quantities generated by the ice density contrast. *Contributions to Geophysics and Geodesy*, 40(3): 207-223
11. Tenzer R, Hamayun, Novák P, Gladkikh V, Vajda P (2012) Global crust-mantle density contrast estimated from EGM2008, DTM2008, CRUST2.0, and ICE-5G. *Pure and Applied Geophysics* 169(9): 1663-1678
12. Tenzer R, Novák P, Hamayun, Vajda P (2012) Spectral expressions for modelling the gravitational field of the Earth's crust density structure. *Studia Geophysica et Geodaetica* 56(1): 141-152; doi: 10.1007/s11200-011-0023-7
13. Tenzer R, Novák P, Vajda P, Gladkikh V, Hamayun (2012) Spectral harmonic analysis and synthesis of Earth's crust gravity field. *Computational Geosciences* 16(1): 193-207

### **Conference Contributions**

1. Hamayun, Tenzer R, Prutkin I (2008) The comparison of various integration methods of solving Newton's integral at the vicinity of the computation point. *International Symposium on Gravity, Geoid and Earth Observation GGEO 2008, Session 5: Regional gravity field modeling. 23-27 June, 2008, Chania, Crete, Greece*
2. Hamayun, Tenzer R, Prutkin I (2008) Smoothing effect of the topographical corrections applied to various types of the gravity anomalies. *International Symposium on Gravity, Geoid and Earth Observation GGEO 2008, Session 5: Regional gravity field modeling. 23-27 June, 2008, Chania, Crete, Greece*
3. Hamayun, Prutkin I, Tenzer R (2008) Analytical expression in terms of line integrals for a potential of the polyhedral bodies with the linearly varying density. *General Assembly of the European Geosciences Union, Vienna, Austria, 13-18 April, 2008; Session G2 : "Recent Development in Geodetic Theory" (poster presentation); published in G2 proceedings (oral papers and posters). Vol. 54, Publication No. 45 in the series of publications of the Research Institute of Geodesy, Topography and Cartography, Zdiby, Prague-East*
4. Hamayun, Tenzer R, Prutkin I (2008) Global map of the no-topography gravity anomalies. *General Assembly of the European Geosciences Union, Vienna, Austria, 13-18 April, 2008; Session G2 : "Recent Development in Geodetic Theory" (poster presentation); published in G2 proceedings (oral papers and posters). Vol. 54, Publication No. 45 in the series of publications of the Research Institute of Geodesy, Topography and Cartography, Zdiby, Prague-East*



5. Hamayun, Tenzer R, Prutkin I (2008) Gravitational field generated by the total ocean mass. IAG International Symposium on Gravity, Geoid and Earth Observation GGEO 2008, Session 5: Regional gravity field modeling. 23-27 June, 2008, Chania, Crete, Greece
6. Tenzer R, Hamayun, Vajda P, Novák P (2009) A smoothing effect of the topographical correction on gravity disturbances in rugged mountains and flat regions – Case study for the Canadian Rocky Mountains. Session G11: High resolution geoid modelling with satellite, marine, terrestrial, and airborne gravity data, The General Assembly 2009 of the European Geosciences Union (EGU), Vienna, Austria, 19 – 24 April 2009 (poster presentation); Abstract published in: Geophysical Research Abstracts, 11, 6615.
7. Tenzer R, Hamayun, Vajda P, Novák P (2009) Global modeling of the ice stripping correction in terms of the ice thickness spherical functions. Session G17: Recent Developments in Geodetic Theory, The General Assembly 2009 of the European Geosciences Union (EGU), Vienna, Austria, 19 – 24 April 2009 (poster presentation); Abstract published in: Geophysical Research Abstracts, 11, 6610.



# Samenvatting

Momenteel wordt een enorme verbetering waargenomen in de nauwkeurigheid en ruimtelijke resolutie van globale zwaartekrachtmodellen van de aarde. Deze verbetering wordt bereikt door het gebruiken van verschillende nieuwe gegevens, waaronder die van gravimetriesatellietmissies (CHAMP, GRACE en GOCE); terrestrische en vliegtuiggravimetriegegevens, evenals altimetriegegevens. De nieuwe modellen van het zwaartekrachtveld kunnen in het bijzonder worden toegepast om onze kennis van de interne structuur van de aarde te verbeteren. Het doel van deze studie is om een globale kaart van de Moho-interface samen te stellen door gebruik te maken van een globaal zwaartekracht model en extra beschikbare informatie over de korstdichtheidsstructuur. In ons onderzoek gebruiken we het zwaartekrachtveldmodel EIGEN-6C2 en het wereldwijde aardkorstmodel CRUST 1.0, afgeleid uit seismische gegevens. Daarnaast gebruiken we op seismische data gebaseerde modellen van de Moho als a-priori-informatie: het CRUST 1.0-model en het Crust07-model, dat werd afgeleid van een volledige niet-lineaire inversie van fundamentele oppervlaktegolven.

Het waargenomen zwaartekrachtveld bevat hindersignalen van de topografie en de dichtheidheterogeniteit met betrekking tot bathymetrie, ijs, sedimenten en andere aardkorstcomponenten. Daarom modelleren en verminderen we opeenvolgend deze signalen door het toepassen van zogenaamde strippingcorrecties. Dit resulteert in een korst ontdane zwaartekrachtgrootheden (zwaartekrachtanomalieën en zwaartekrachtverstoringen). In de loop van het onderzoek bespreken we verschillende analytische, semi-analytische en numerieke voorwaartse modelleringstechnieken om de zwaartekracht van een lichaam te berekenen. We leiden ook een analytische formule af voor de berekening van de zwaartekracht potentiaal gegenereerd door een polyhedraal lichaam met lineair variërende dichtheid. Wij berekenen de correcties van het waargenomen zwaartekrachtveld met analytische methoden in nabijheid van het lichaam en met semi-analytische methoden voor het verre veld. We laten zien dat de opeenvolgende correctie voor de ongewenste signalen de correlatie van de zwaartekrachtverstoringen en zwaartekrachtanomalieën met de Moho-diepte verhoogt. We maken gebruik van het gecorrigeerde zwaartekrachtveld om de globale (gemiddelde) waarde voor korst-mantelcontrastdichtheid te vinden met behulp van de Pearson's correlatiemethode. We gebruiken een empirische techniek waarbij de absolute correlatie tussen de Moho-diepte uit het CRUST 1.0-model en de van korst ontdane zwaartekrachtverstoringen/anomalieën zijn geminimaliseerd. Deze gecorrigeerde zwaartekrachtverstoringen/anomalieën worden verkregen door toevoeging

van een bijdrage (aantrekking) gerelateerd aan het dichtheidscontrast tussen de referentiekorst en de bovenste mantel.

Het bepalen van de Moho-geometrie is gebaseerd op het oplossen van een lineair stelsel vergelijkingen dat het van korst ontdane zwaartekrachtsveld (weergegeven in termen van sferische harmonische coëfficiënten) verbindt aan de Moho-geometrie (weergegeven in termen van Moho-diepte op de knooppunten van een gelijkhoekig geografisch rooster). Zo worden correcties op de voorafgaande Moho-configuratie geschat. Het is bekend dat een opzichzelfstaande inversie van gravimetrische gegevens kan leiden tot onjuiste resultaten, omdat het onmogelijk is om het signaal van de discontinuïteit in kwestie te scheiden van gravimetrische signalen van andere bronnen (in het bijzonder van bronnen die zich dieper in de aarde bevinden). Om de laatstgenoemde signalen te onderdrukken (bijvoorbeeld die betrekking hebben tot inhomogeniteiten van de manteldichtheid en diepe structuur van de aarde) stellen we voor om de bijdrage van lage sferisch harmonische graden van de inputzwaartekrachtgegevens te elimineren. Verder passen we maatafhankelijke gewichten toe aan de resterende sferisch harmonische coëfficiënten. De gewichtsmatrix is zodanig ontworpen dat een lage graad minder weegt en een hoge meer.

We hebben een geavanceerde inversieprocedure ontwikkeld waarbij zwaartekrachtgegevens en informatie van andere (seismische) bronnen tegelijk worden uitgebuit, gebruikmakend van de nulde orde en eerste orde Tikhonov-regularisatieconcepten. De variance components estimation (VCE) procedure is gebruikt voor het schatten van de relatieve gewichten van de verschillende datasets.

We beschouwen een aantal inversie strategieën gebaseerd op verschillende combinaties van datasets, regularisatiesoorten, graadafhankelijke gewichten toegepast op inputzwaartekrachtgegevens, alsmede minimum- en maximumafbreekgraden van de input zwaartekrachtgegevens. Voor de selectie van optimale inversie parameters vergelijken we de ontwikkelde Moho-modellen met twee regionale Moho-modellen voor de Europese korst. De twee modellen omvatten EuCrust07 en EuM09, ontwikkeld door respectievelijk Magdala Tesauro et al. en Marek Grad et al. We ondervinden dat het beste model te verkrijgen is door het gebruiken van een gezamenlijke inversie (zwaartekracht gegevens plus CRUST1.0 en CRUST07 seismische modellen), eerste -orde Tikhonov-regularisatie, graadafhankelijk gewichten evenredig met de vierde macht van de graad en het gelijk stellen van de minimale en maximale afbreek graad aan respectievelijk 90 en 180). Het uiteindelijke Moho-model (DMM-1) is vergeleken met twee regionale modellen: (1) voor Zuid-Amerika en (2) voor Afrika. Uit de vergelijking en statistische analyse vonden we dat ons ontwikkeld model DMM-1 de geschiktste RMS-waarden heeft voor de twee regionale modellen, evenals met geobserveerde puntwaarden.

# Propositions

accompanying the PhD dissertation

Global Earth structure recovery from state-of-the-art models of the Earth's gravity field and additional geophysical information

by Hamayun

1. Gravity disturbances are more suitable for the recovery of the Moho than gravity anomalies.
2. Nuisance signals in gravity data can be effectively damped using degree-dependent data weights.
3. The combination of gravity data and seismic models of the Earth crust ameliorate the Moho recovery.
4. Gravity data complete to degree 180 contain substantial information about the Moho geometry.
5. Data of the GOCE satellite gravity mission facilitate the improvement of Moho models in remote areas.
6. Military operations cannot change the human mentality.
7. Instead of spending lavishly on higher education, Pakistan must focus on the primary education.
8. There is no such thing like the best model for a given phenomenon.
9. There is no space for research if there is an issue of survivability.
10. Access to the Internet must become a basic human right.
11. People demanding for a 'dislike' button on Facebook actually mean a 'hate' button.

*These propositions are regarded as opposable and defensible, and have been approved as such by the promotor, Prof. Dr.-Ing. Habil Roland Klees.*

## Stellingen

behorende bij het proefschrift

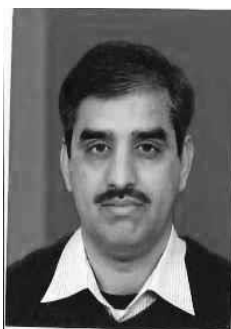
Global Earth structure recovery from state-of-the-art models of the Earth's gravity field and additional geophysical information

door Hamayun

1. Zwaartekrachtverstoringen zijn geschikter voor het bepalen van de Moho dan zwaartekrachtanomalieën.
2. Ongewenst signaal in zwaartekrachtgegevens kunnen effectief gedempt worden met behulp van graad-afhankelijke dataweging.
3. De combinatie van zwaartekrachtgegevens en seismische modellen van de aardkorst verbeteren het bepalen van de Moho.
4. Het zwaartekrachtsveld tot en met graad 180 bevat substantiële informatie over de geometrie van de Moho.
5. Meet gegevens van de GOCE zwaartekrachtsatellietmissie vergemakkelijken de verbetering van Moho modellen in afgelegen gebieden.
6. Militaire operaties kunnen de menselijk mentaliteit niet veranderen.
7. In plaats van royaal te besteden aan het hoger onderwijs moet Pakistan zich richten op het basisonderwijs.
8. Er bestaat geen beste model voor een bepaald fenomeen.
9. Er is geen ruimte voor onderzoek als er een overlevingskwestie is.
10. Toegang tot het internet moet een fundamenteel mensenrecht geworden.
11. Mensen die een vind-ik-niet-leuk-knop eisen op Facebook bedoelen eigenlijk een haat-ik-knop.

*Deze stellingen warden opponeerbaar en verdedigbaar geacht en zijn als zodanig goedgekeurd door de promotor Prof. Dr.-Ing. Habil Roland. Klees.*

## Curriculum Vitae



**Hamayun** was born on April 09, 1970 in Shewa, Swabi, Pakistan. He finished his secondary schooling from Swabi in 1989, and studied Physics in his bachelors degree till 1992. Subsequently, he graduated with MSc degree in Physics from Peshawar University, Pakistan in 1994. Later, he attained MPhil degree in Physics in the field of laser spectroscopy from Quaid-i-Azam University (QAU), Islamabad in 1997. Afterwards, he joined Center of Excellence in Science & Applied Technologies, Islamabad, Pakistan, as a scientific researcher.

In April 2007, he obtained a scholarship from Higher Education Commission (HEC) Pakistan for pursuing PhD studies, and joined Physical and Space Geodesy group in the faculty of Aerospace Engineering and later faculty of Civil Engineering and Geosciences at Delft University of Technology, the Netherlands. He worked on global Earth structure recovery from state-of-the-art models of the Earth's gravity field and additional geophysical information under the supervision of Dr. P. Ditmer, Prof. R. Klees and Prof. R. Tenzer. The research conducted by him is presented in this thesis.